UiT
THE ARCTIC
UNIVERSITY
OF NORWAY

Faculty of Science and Technology
Department of Physics and Technology

Survey and simulation of space debris using EISCAT UHF

—

Elisabeth Kristina Røynestad

FYS-3931 Master's thesis in Space Physics, 30 sp, June 2018

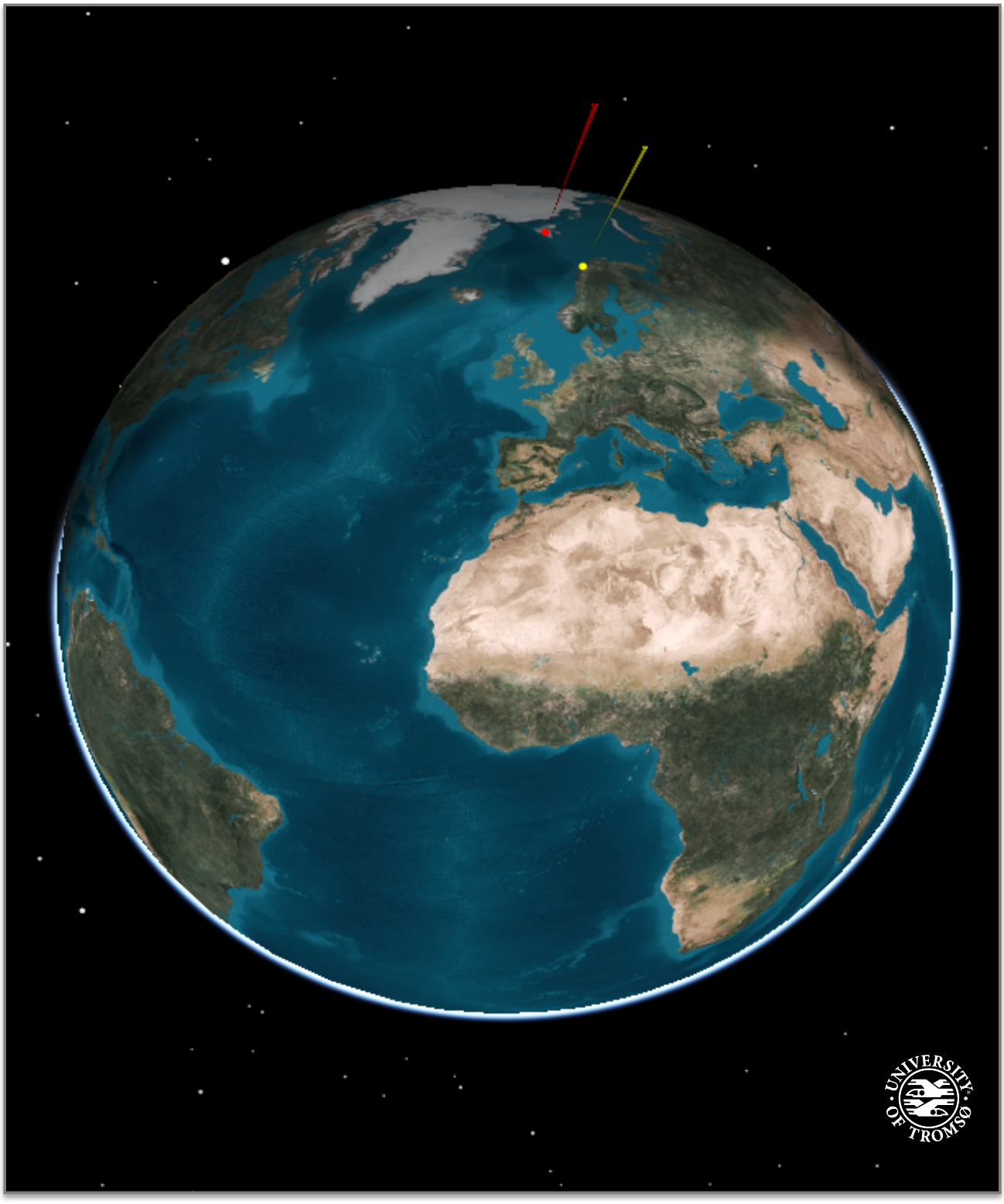

"That's here. That's home. That's us. On it, everyone you ever heard of, every human being who ever lived, lived out their lives. (...) To my mind, there is perhaps no better demonstration of the folly of human conceits than this distant image of our tiny world. To me, it underscores our responsibility to deal more kindly and compassionately with one another and to preserve and cherish that pale blue dot, the only home we've ever known."

— **Carl Sagan**, *speech at Cornell University, October 13, 1994*

Abstract

This thesis starts with a review of the evolution of space debris, what is consists of, how it is made, how it is detected and tracked, and why it is such an important topic. Some of the worst collisions have contributed to causing 49% of the total space debris. If the launch rate continues, the "Kessler Syndrome" might become a reality destroying our future outlook for space communication and exploration. Furthermore, a deeper look at the contents is done and what is the impact of these hypervelocity objects. Highly-advanced ground surveillance systems are used to track and catalog the space debris stationed around the globe, and highly sophisticated space debris models are used to estimate the density of the total space debris population in all sizes, shapes and compositions. After 60 years in space, a lot of space debris has accumulated, resulting in a large increase of density in the polar regions. However, objects below 10 cm are not easily detected, but EISCAT UHF is capable detecting the sizes below 10 cm and down to 1 cm by using beampark experiments, its location makes it suitable for detecting polar region debris. The data is then used to confirm the catalog and the models.

A 24-hour beampark experiment was done on 4th of January 2018 simultaneously at Tromsø and Svalbard, specifically for this thesis. It statistically measured the range, the Doppler velocity, and the echo strength of space debris. An inversion of apogee and inclination was then done by using these parameters.

A modelling of a beampark experiment was simulated, propagating objects through the EISCAT UHF beam. It extracted the data from the ESA MASTER model and the output was the number of detections per day. A comparison of the beampark experiment 2018 campaign with the simulation model indicated that the simplified model shows good correlation with the observations.

Aknowledgement

The one I would like to thank most of all is my supervisor, Professor Juha Vierinen. Thank you for putting me on this quest, and for giving me such an inspiring and interesting topic. Thank you for all the good support. Mostly, I will thank you for the incredible help with the code, you are truly a master in python.

I am forever grateful to Derek McKay for the help you gave me in these final hours before submitting the thesis, and the amount of work you did by proof-reading it.

Also, I would like to thanks Arja and Marcus for also proof-reading it.

I want to thank my office buddy Nozhan for all the discussions we had from physics to old classic movies, and for all the help with my thesis..

I am forever grateful to the CREATE foundation which provided me with space mission training. I would never have been this excited about satellites, radars, and space mission if it wasn't for that opportunity.

I would like to thank the people I have studied with who has always supported me and helped me through my studies, you know who you are. I would especially thank my brother from another mother, Magnar, who has always been there for me no matter what.

I want to thank my parents who has always supported me and believed in me, Egil and Keth, as well my siblings with their respective families who always surrounded me with love and support.

Last, but not least, I want to thank my amazing boyfriend, Christopher, for always making me laugh, and making me feel special, and for making me believe in myself again.

Sincerely,
Elisabeth Røynestad
elisabeth.roynestad@gmail.com
June 2018, Tromsø

Contents

List of Figures

List of Tables

Abbreviations

STK Satellite Tool Kit

AGI Artificial General Intelligence

SGP4 Simplified General Propogator

TLE Two-Line-Element

ECEF earth Center earth Fixed

COE Classical Orbital Elements

RAAN Right Ascension of the Ascending Node

LEO Low earth Orbit

HEO Highly Elliptical Orbit

GTO Geostationary Transfer Orbit

MEO Medium earth Orbit

GEO Geostationary earth Orbit

EOL End Of Life

IADC Inter-Agency Space Debris Coordination Committee

PMD Post Mission Disposal

ESA European Space Agency

NOAA National Oceanic and Atmospheric Administration

RADAR RAdio (Aim) Detection And Ranging

LIDAR LIght Detection And Ranging

HPLA High Power Large Aperture Radar

OGS Optical Ground Station

SLR Satellite Laser Ranging

MASTER Meteoroid and Space Debris Terrestrial Environment Reference

NASA National Aeronautics and Space Administration

ORDEM Orbital Debris Engineering Model

DELTA Debris Environment Long Term Analysis

POEM The Polar Orbiting earth Observation Mission

TIRA Tracking and Imaging Radar

PROOF Program for Radar and Optical Observation Forecasting

DISCOS Database and Information System Characterising Objects in Space

SSN Space Surveillance Network

ISS International Space Station

FFI Forsvarets Forsknings Institutt

UiT University in Tromsø

NTNU Norges Teknisk Naturvitenskapelige Universitet

UiO University in Oslo

EM Electromagnetic

VHF Very High Frequency

UHF Ultra High Frequency

EISCAT European Incoherent SCATter Scientific Association

IRI International Reference Ionosphere 2007 Model

BPE Beampark Experiment

dB Decibel

RCS Radar Cross-Section

FOV Field-Of-View

SNR Signal-to-Noise Ratio

GMF Generalized Matched Filter

LOS Line-of-Sight

FMF Fast Matched Filter

Chapter 1

Introduction

"Debris is all about the small stuff and their sources, and how we manage that."

— **Donald Kessler**[1]

Satellites have advanced significantly over the years compared to what their original idea. It was proposed by Arthur C. Clark that satellites was to just function as relé for communication. However, now they work more than just mirroring the signal. With advanced signal processing and with several mission objects applied on the satellites, the application has been expanded to more than communication. Satellites are currently used for many things such as weather monitoring, navigation, worldwide communication, and other research areas.

In recent years, space exploration has become more available for the public, making more countries, universities and companies involved in space missions, and launching out into space will only increase in the future. This will making it even more crowded up there than it already is. Some of the orbits are already overcrowded due to their popular altitude and inclination. Especially, the polar regions, which have increased in density and keeps on growing.

Space has been treated in the same way as the ocean. We think it is so big, that no harm will come to us by dumping things into it. Now, after 60 years in space without taking out the trash, it has started to get crowded up there. The atmosphere is the only known way that due this date at decaying space debris.

The space surveillance network (SSN) keeps track of all kinds of objects orbiting the earth. However, even with the most highly advanced radars and telescopes in the world, the smallest debris below 10 cm are not traceable.

By using the EISCAT radar facilities in the northern Scandinavia, space objects down to 1 cm in size are thus detectable, making EISCAT better than most of ground tracking apertures by the SSN. This is done by using beampark experiment, which steers the antenna beam into a fixed point. Then the antenna is parked for 24 hours, and tracks all space objects which flies trough the beam. By this, the radar retrieves parameters such as the range R, time t, signal power S, and the radial velocity v_d. With these parameters an inversion is done by using these parameters to find the space debris' orbital elements, and an attempt to find the size of the space debris.

The purpose of this thesis is to analyze two 24 hour observation of space debris obtained with the EISCAT incoherent scatter radars, one in Longyearbyen at Svalbard and the other at Ramfjordmoen at Tromsø.

The thesis consists of three parts

[1] Said during the 7th European Conference on Space Debris in Darmstadt, Germany, 21.April 2017

1. Introduction to space debris.
2. Introduction to radar measurements of space debris
3. Modelling EISCAT observation of space debris

The main contribution will be in the third part of the thesis. The aim will be to model the response of the EISCAT radars to space debris objects characterized by orbital elements and size (debris parameters). This will be done by numerically propagating objects with different debris parameters and obtaining a radar sensor response. Next, this sensor response can be used to determine the relationship between a beampark observation of the space debris and its population.

This thesis will start by introducing the laws of physics needed for objects to stay in certain orbits in chapter 2, and introduce what parameters are needed to keep track of all the objects.

Further in chapter 3, a brief history of space debris will be introduced, followed by what the consequences of space debris are, the density distribution in each altitude, what it consists of, how large they are, and what the risks and the impacts it has if one should be that unfortunate to be hit by one.

Next, it will be explained how space debris is being tracked by ground surveillance instruments, and end with how the space debris is being estimated by models.

In the last section of the space debris chapter it will be investigated some of the future entries of how to deal with the space debris, and what Norway has as its policies of space debris.

Chapter 5, will go through the specifications of radars and high power large aperture (HPLA) radars are used to measure space debris, the parameters and in order to perform radar measurements as well its measurements techniques used to detect the objects orbiting through the beam of EISCAT. These are as well used in the simulation to emulate a beampark measurement.

In chapter 6, the concept of how a beampark experiment (BPE) is performed followed up by the results from the actual BPE performed for 24 hours at the 4th of January 2018.

In chapter 7 and 8, the third concept of this thesis will be introduced and the statistical measurements will be discussed and the chapter will finish up by comparing the simulated versus the measured space debris with the EISCAT UHF Tromsø, and take a look at the signal to noise ratio of the detected objects to see if it feasible to get some information about its true size in diameter. However, due to time constrains and the objectives with the third contribution of this thesis, only the radar measurements done at Tromsø UHF of the beampark experiment and the simulation in part 3 is considered here in this thesis.

1.1 Software and Data

A brief overview of what software has been used in this thesis.

1.1.1 STK

Satellite Tool Kit (STK) is a space mission analysis software by Artificial general intelligence (AGI) which uses a simplified general propagator (SGP4) and uses the cataloged two-line-element (TLE) data of spacecrafts and space debris in orbit to propagate the trajectory for the desired spacecraft. Only its demo version was used in this thesis to visually understand the size of the beam and how spacecrafts moves through the beam. However, with the full version it will be possible to generate a video simulation of how satellite collision occur and how they crash and causing space debris and how it distributes itself after time. The front page illustrates the beams of EISCAT at Tromsø and Svalbard and was made in STK [4].

1.1.2 Stallo

The simulation of the BPE was done through the super computer, Stallo, at the University of Tromsø. The name comes from Samí folklore. It was installed in 2007, and has a mass of 16 000 kg, 704 servers whereas each of these has a 2.66 GHz four kernel processor, 16 GB RAM and 120 GB hard drive. Altogether the Stallo has 12 TB RAM and 128 TB with hard drive capacity.

1.1.3 Python 2.7

Python 2.7 is a free programming software that was used to perform all the necessary calculations of the simulation, extracting data from the BPE, and plotting all its corresponding figures, as well when run the simulation in Stallo.

1.1.4 ESA MASTER Model

The data file of ESA MASTER model with all estimated and cataloged space debris and spacecrafts in all the orbits with its corresponding Keplerian elements was given by ESA and implemented with the simulated data.

1.1.5 SpaceTrack

All the cataloged unclassified data of all objects in and decayed orbits with its corresponding two-line-element (TLE) data is found by using the data from space-track.org [5].

1.1.6 Beampark Experiment

Data collected with the EISCAT radars through the beampark experiment used to perform its statistical analysis.

Chapter 2

Satellite orbits

2.1 Keplerian Elements

In space applications different types of coordinate systems may be used for different purposes, such as spacecraft attitude control systems and space mission navigation. For observations from earth, a coordinate system called earth Centered earth Fixed (ECEF)[1] uses **X,Y,Z** positions at the center of the earth. The axes are fixed on the surface of the earth as a reference point, and thus follows the earth rotation as fixed points. The **Y**-axis is perpendicular to the **Z** and **X** axis. It is crucial to select the right coordinate systems in order to reduce errors and to gain insight into the problem when dealing with satellite orbits. The earth and satellite can together, to first order, be described as a two-body system, or equation of motion, by combining Newtons Second Law and Newtons law of Gravitation.

Johannes Kepler introduced three laws of planetary motions in 1609 and 1619 by finding data matched with a geometric solution of elliptical orbits. These three laws of planetary motion can also describe satellites orbiting the earth [6]. They are the following:

1. **Kepler's 1st law**
   The orbit of each planet is an ellipse, with the Sun at one focus.

2. **Kepler's 2nd law**
   The line joining the planet to the Sun sweeps out equal areas in equal times.

3. **Kepler's 3rd law**
   The square of the period of a planet is proportional to the cube of its mean distance from the Sun.

These orbits can be any of four conic sections: a circle, an ellipse, a parabola, or a hyperbola. However, since space debris mostly moves in an elliptic or circular orbit near low-earth orbit (LEO), we neglect the parabola and hyperbola orbits in this thesis. Furthermore, Keplerian elements can be used to characterize the orbital regimes of objects. The orbital inclinations used for satellites near earth are the following orbits with different inclinations shown in table (2.1).

When the inclination is $i = 180°$ the equatorial orbit is called retrograde equatorial orbit. The six classical orbit elements (COE) help describe and locate the objects position in orbit. Figure (2.1) and table (2.2) shows the six COE used to describe a satellite orbiting the earth. The inclination, i, and the Right Ascension of the Ascending Node (RAAN), Ω, shows the the angle between the

[1] Also called ECR (earth Centered Rotational)

Table 2.1: Orbital regimes of objects characterized by Keplerian orbits showing their respective inclinations

Orbit	Inclination, $i(^\circ)$
Equatorial	$i = 0^\circ$
Polar	$i = 90^\circ$
Sun-Synchronous	$i = 100^\circ \pm 5^\circ$
Navigation Satellite	$i = 55^\circ \& i = 65^\circ$
Critical Inclination	$i = 63.5^\circ$
Retrograde	$90^\circ < i < 180^\circ$
Prograde	$0^\circ < i < 90^\circ$

angular momentum vector, **h** and the unit **Z**-axis and the orientation of the orbiting object in space, respectively, whereas the size and the shape of the orbit plane is described by the semi major axis, a, and the eccentricity, e. The orientation of the ellipse in the plane is described by the length of the perigee, ω. The last one shows the position of the object in the orbit plane and this is described by the true anomaly, ν, and is a function of time which is the only variable of these six elements [6]. The radius of apogee and perigee is also in the table as often used to describe the specific orbital plane.

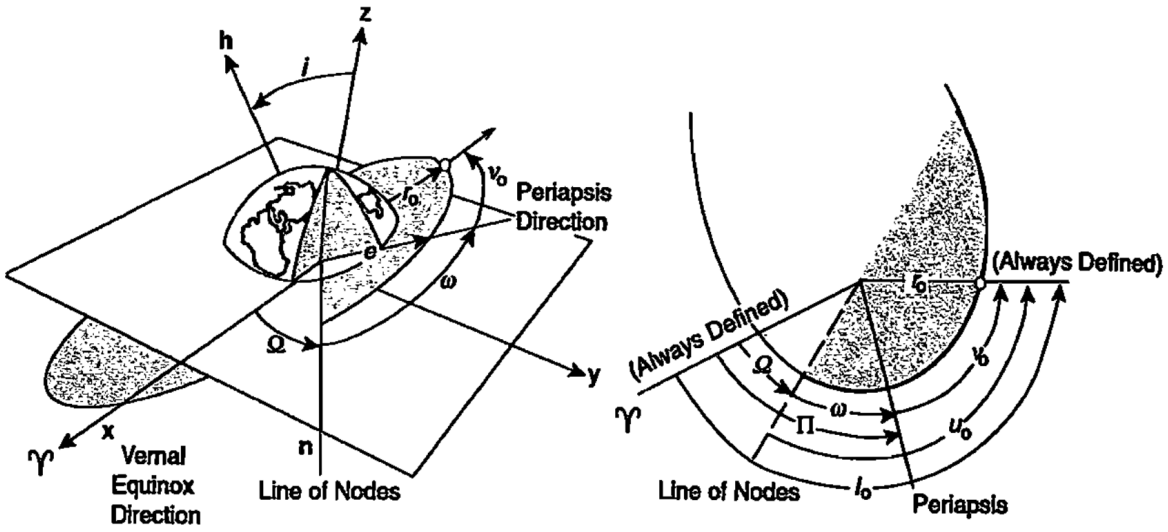

Figure 2.1: The Classical Keplerian Orbital Elements for a satellite orbiting the earth in an elliptic orbit [6]].

Keplerian elements are also used in the commonly used two line element (TLE) format for storing and distributing the orbital parameters of a satellite. Software using the TLE format can be used to keep track of a satellite's orbit. TLE data for tens of thousands of earth orbiting space objects is distributed by the US Space Surveillance Network and can be accessed through the Space Track service [5].

Table 2.2: The Six Classical Orbital Elements (COE) [6]

Parameter	Formula
Inclination, i	$i = \cos^{-1} \frac{h_z}{h}$
RAAN, Ω	$\Omega = \cos^{-1} \frac{n_x}{n}$
Semi major Axis, a	$a = -\frac{\upsilon}{2\epsilon} = \frac{r_A + r_P}{2}$
Eccentricity, e	$e = \lvert\mathbf{e}\rvert = 1 - \frac{r_p}{a} = \frac{r_A}{a} - 1$
Argument of Perigee, ω	$\omega = \cos^{-1}[\frac{\mathbf{n}\cdot\mathbf{e}}{n\cdot e}]$
True Anomaly, ν	$\nu = \cos^{-1}[\frac{\mathbf{e}\cdot\mathbf{r}}{e\cdot r}]$
Radius of Perigee, r_p	$r_P = a(1-e)$
Radius of Apogee, r_A	$r_A = a(1+e)$

2.2 Low earth Orbit (LEO)

The low earth orbit (LEO) is the orbit closest to earth, but it is also the orbit with the largest density of space debris. The satellites here are not as big as in the terms of mass and size. LEO ranges from 200 km to 2000 km, and the satellites here orbit at different inclinations varying from i = 0° to i = 180° and with eccentricity of $e \approx 0$. The satellites can move from south to north in polar orbits, around the equator in equatorial orbits, or in-between these two with so called inclined orbits in both retrograde and prograde directions.

One popular orbit with high inclination is the so called sun-synchronous orbit or the dawn-dusk orbit, here the satellite follows the earth's day and night terminator such that its solar panels are then always pointed towards the Sun. This is essential for satellites to exploit maximum solar energy, and minimum battery payload. Satellites here orbit the earth approximately 14 times a day, with a orbital period of approximately 100 minutes.

The advantages of having satellites in LEO is the large number of orbits per day, making them perfect for earth observations such as remote sensing and weather measurements. In addition, the satellites in low altitude orbits are protected by the earths magnetic field from cosmic radiation and grants a good coverage of the polar regions. However, they are more susceptible to atmospheric drag and they will also de-orbit faster[2] than the higher altitude satellites, which results in less coverage time.

[2] orbits at 200 to 400 km de-orbits after a couple of years [6].

2.3 Highly Elliptical Orbit and Geostationary transfer orbit

2.3.1 Highly Elliptical Orbit (HEO)

The highly elliptical orbit (HEO) was mainly used by the Soviet Union for their Molniya satellites, and are still being used now by the Russian Space Agency ROSCOSMOS. HEO has a high inclination which gives good coverage of the most northern areas, and it has high eccentricity with a large perigee and small apogee which ensures the satellite to spend a good amount of its time at these certain areas. It is geosynchronous which means that its period of time is 12 hours. To obtain a continuously coverage, a three-satellite constellation was the solution, where the satellites was separated by 120° in-between each others. Molniya, Tundra and the other satellites in HEO has all the same inclination of i=63.4°, this to ensure that the trajectory is fixed in the orbital plane.

2.3.2 Geostationary transfer Orbit (GTO)

The geostationary transfer orbit (GTO) is where the satellites goes into an elliptical orbit, which allows them to exploit the earths gravitation to increase their momentum. When sufficient momentum is gained, they will make the transfer from HEO to a MEO or LEO orbit. This maneuver is also known as Hohmann transfer, which is a normal way of changing orbit with minimal use of rocket fuel. These are often launched near the equator and has a low inclination in order to be transferred out to geostationary orbit (GEO).

2.4 Medium earth Orbit (MEO)

Between LEO and GEO is the medium earth orbit (MEO) were the satellites orbits in-between the two highly concentrated charged particles belts, the Van-Allen Belts. The satellites here orbits in the range of 10 000 km and ≈26 000 km, with a period of a sidereal time and is synchronized with the earth's rotation. Typically navigation satellites are stationed here such as the GPS satellites, which consists of satellite constellations such as Iridium, GLONASS and GlobStar. In this orbit, satellites are highly exposed to radiation due to the Van-Allen belts and other cosmic radiation. However, due to the high altitude, less spacecrafts are needed in a constellation to provide global coverage.

2.5 Geostationary earth Orbit (GEO)

The geostationary earth orbit (GEO) is the orbit furthest away from the earth. The satellites here are stationed side-by-side like a pearl necklace at an altitude of 42 164 km from the center of the earth (≈36 000 km away from the earth's surface). This orbit is a circular orbit with eccentricity of $\varepsilon = 0$ with inclination of i = 0°, which also makes it an equatorial orbit. The satellites follows the earth's rotation, and thus has the same period of time of 86,164 seconds per day. The satellites that are stationed here are much larger in both size and mass than in LEO, due to their heavy protected shielding, with fuel tanks and large solar arrays. The advantages of having satellites stationed in GEO is firstly that they follow the earth's rotation and is fixed relative to a point on the earth's surface. This makes it possible to get a system that can provide a continuous coverage at a certain area at earth, which is advantageous for satellites that provides communication and television. The disadvantages by using GEO is the great distance, the lack of coverage in the polar regions, the hazardous cosmic radiation, and in fact that it's getting cramped up there, especially in the most

popular longitudes. Also there is limited capacity on the most popular bandwidth frequencies, such as KU- and KA-bands.

2.6 End of Life

All spacecrafts has an end-of-life (EOL) after their mission is done. This normally happens after 10 - 15 years in space. According to IADC by the committee for Post Mission Disposal (PMD) all satellite distributors has to have a plan to get rid of their spacecraft in a almost risk-free way. For objects in LEO (below 1000 km) they have to re-enter after at least 25 years. At a satellite's EOL it has either degraded by cosmic radiation coming from either the solar wind or from deep space, or it runs out of fuel so it uses its last amount of fuel to either boost itself into the GEO Graveyard or de-orbit into the atmosphere and re-enters the earth. Nevertheless, this is usually closely tracked and calculated to land in the ocean far from land and harm to people. Or it can be destroyed either by intentional or unintentional collisions. It may take years for objects in orbit to re-enter the atmosphere. For orbits at around 400 km it may take only one year for the object to start to de-orbit, but if the altitude is increased to 600 km it may take 25 years for it to enter the atmosphere, and even longer as as the altitude increases. For objects orbiting in MEO and GEO it will take even longer to de-orbit. The GEO graveyard contains of old satellites and fuel tanks, and is placed at a perigee altitude of 300 km above the GEO ring [6].

Chapter 3

Space Debris

3.1 History

It all started with the idea by Arthur C. Clarke to put artificial satellites into space to use them for long distance communication around the earth. In 1945 he published the article "Extra-Terrestrial Relays" in the October edition of the magazine *Wireless World* [7]. 12 years later at October the 4th, 1957 the Soviet Union launched the first Satellite to orbit the earth, *Sputnik-1*, which de-orbited three months after its launch. This was the first man-made satellite in space [6]. Only four years later the first break-up event occurred, in June 1961 the transit 4-A was then the first to make space debris.

The Westford Needles Project was a needless project in the early 60's. Millions of needles were sent up to work as small dipole antennas used for communication, but failed since they clustered together due to inefficient coating. They were sent out a second time, but still it did not work even though they did not cluster as much as the first time due to more efficient coatings. These clusters of needles are still orbiting to this date and are trackable, even though most of them have de-orbited [8].

During the Cold War in the 70's and 80's the Soviet and the US. Debris were made over the years due to intentional collisions by testing out anti-missile weapon program, which was done to keep the design of a satellite a secret, or a surveillance reconnaissance satellite (also referred to as spy satellite).

Donald Kessler published at 1st of June 1978 an article *"Collision Frequency of Artificial Satellites: The Creation of a Debris Belt"* . Kessler predicted that there would occur a chain collision if there are too many satellites and space debris in orbit (See section 3.3). This has been later described as the Kessler Syndrome, Today, many models predict that space debris is in collisional cascade [9, 10]

By following *the Timeline of the History of Space Debris* (see figure 3.1) more unintentional collisions has occurred in the later years, not only by small chunks of parts, but also by dust particles from rocket engines. An example of this happened in 2013 with the CubeSat *NEE-01 Pegaso* where they eventually had to declare the satellite as lost due to lack of communication after it went into a debris cloud made by the upper stage of the orbital rocket, *Tsyklon-3*. Today most of the satellites change their orbit several times of year to avoid collisions.

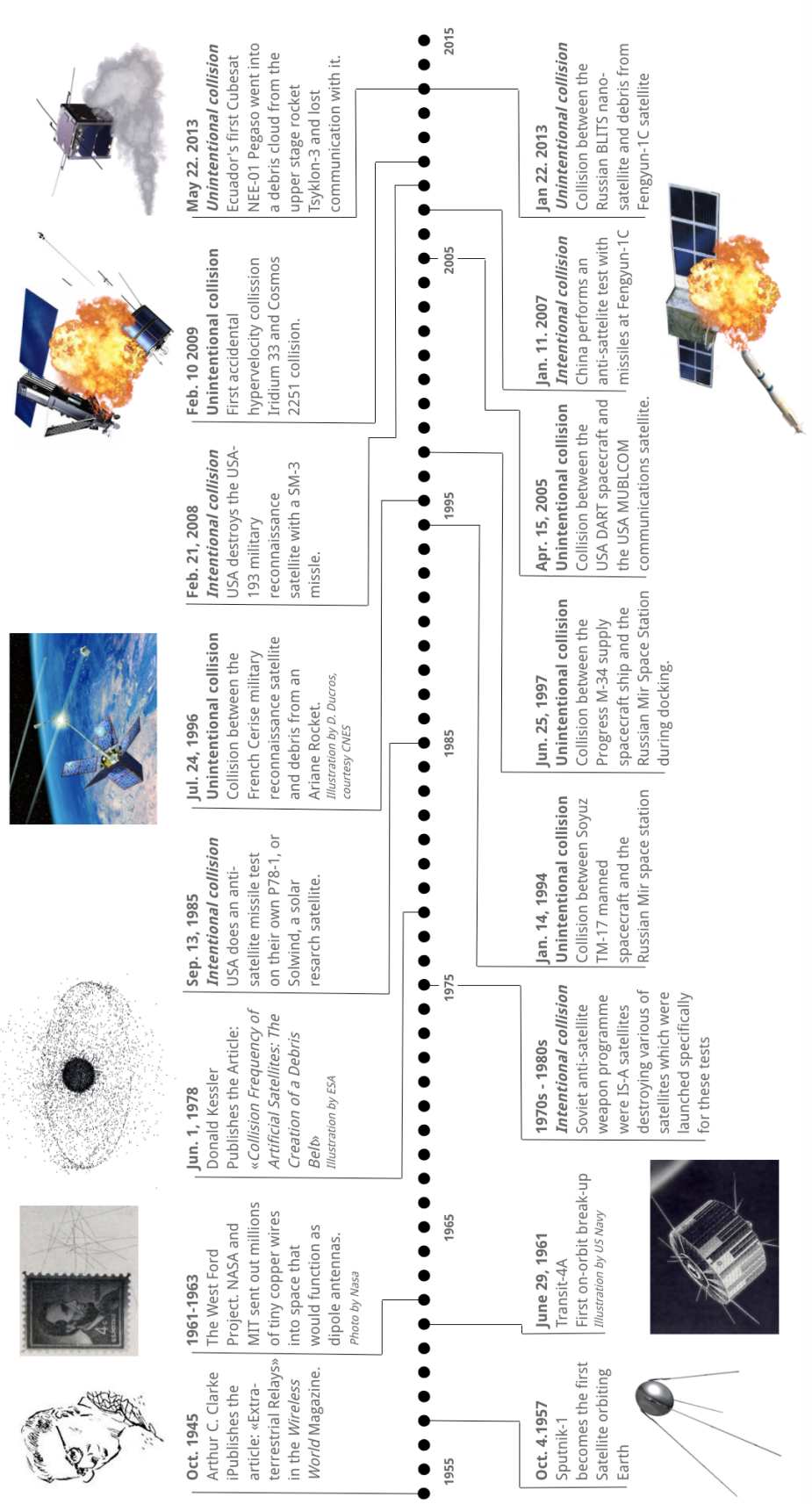

Figure 3.1: A timeline of the history of space debris from 1957 until 2013.

The figure (3.2) shows the evolution of space debris orbiting the earth and what it consist of and the amount of space debris there is. The number of space debris increased linearly the destruction of Fengyun-1C in 2007, leaving behind the worst amount of over 3000 space debris objects in history spreading out over a perigee and apogee of 200 km and out to 4000 km. Two years later the dead Cosmos 2251 satellite with a equatorial orbit hit the Iridium 33 satellite which orbited in a polar orbit, leaving behind over 2000 objects in an altitude of around 800 km. These two is considered as the worst collisions that caused all together 30 % of all the trackable space debris. They are now causing a big threat to all the spacecrafts in altitudes between 700-1000 km.

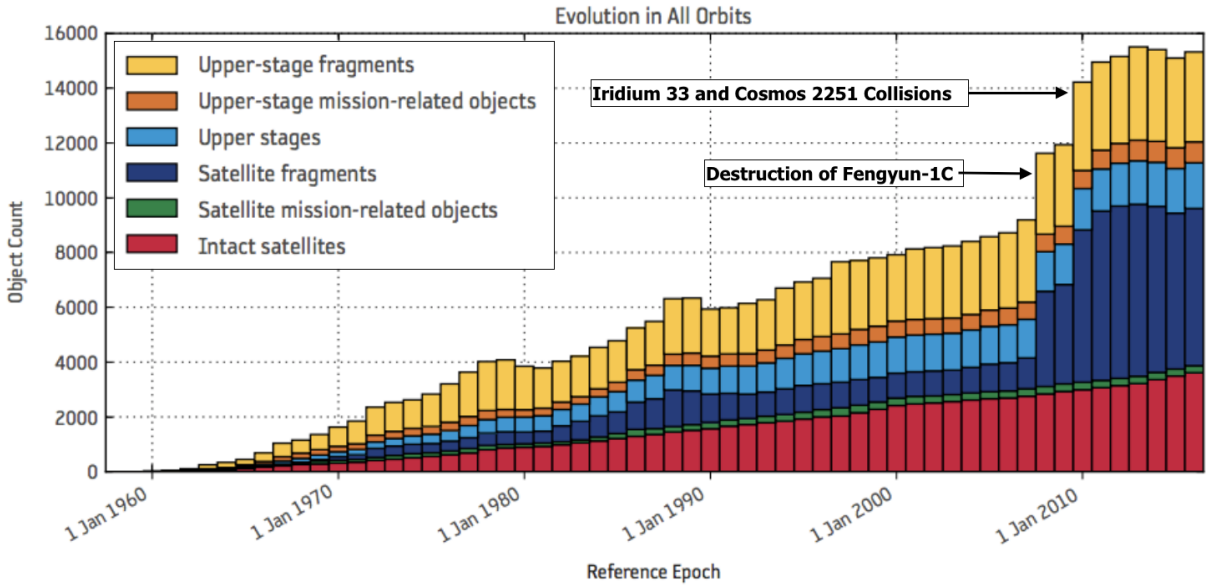

Figure 3.2: A histogram of the evolution of all objects from the first satellite in space in 1957 and until 2017. The event of the two worst collisions in history is marked here. [Figure credit ESA].

3.2 Break-Ups

Spacecraft break-ups is either intentional or unintentional. This can happen for many reasons such as the battery may explode, as the recent NOAA[1] satellite did [11, 12], or it gets shot down by a missile, or that it either get hit by a space debris object, or collide with another spacecraft, or the reason is unknown, such as anomalous event where the spacecrafts loses parts for unknown reasons.

There has been ten large break-ups each causing a large amount of debris. Two of the worst ones are already mentioned in previous section. The figure (3.3a) shows the 10 worst satellite break-ups leaving behind the highest number of space debris in 2017. It is compared in figure (3.3b) that these ten collisions caused 49% of all the total space debris in orbit, were Fengyun-1C alone caused 18% of all the space debris [5, 13].

[1]National Oceanic and Atmospheric Administration

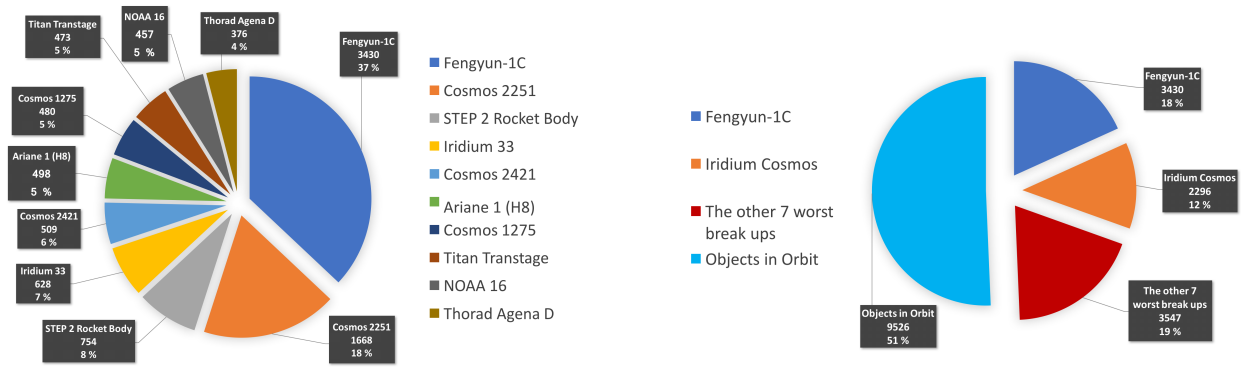

(a) 10 worst satellite break-ups **(b)** Total object of debris in orbit

Figure 3.3: Figure (a) shows comparison of the 10 worst satellite break-ups and the amount of space debris each of them caused. Figure (b) shows total of objects in orbit and how much the 10 worst satellite break-ups causing at December the 1st, 2017 [5, 12].

3.3 The Kessler Syndrome

Donald Kessler published an article together with Burton G. Cour-Palais already in 1978 predicting the increase of objects in LEO is making it crowded. The amount of debris from all the intentional collisions during the cold war, and a large amount of small slag particles from old rocket engines (approximately at centimeter-size) is getting more hazardous for satellites, even after all these years. Hypervelocity[2] collision with space debris would cause a domino effect of crashes, and those fragments would cause more crashes until it will be inevitable for the satellites to maneuver away. Eventually these will crash into each other creating even more space debris destroying other satellites. This will continue until there is no satellite left in orbit. Consequently, this would prevent us from sending things out in space and out to the most crowded orbital regions [10].

After what happened to Fengyun-1C laws have been put up to prevent the Kessler Syndrome to become a reality. A study from 2013 which compares all the space agencies' long-term analysis software concludes that in some orbits in LEO this has already reached that critical point, this due to these two worst collisions leading to an increase of space debris of more than 124% between 700-900 km, even if no new spacecraft are ever launched, the amount of debris will continue to increase far into the future [9].

In figure (3.3b) this is shown that these two collision caused almost 28% of all the space debris detected at 1.December 2017 [5]. How space debris distributes itself after a time is shown in figure (3.4) which shows how the trajectory is after (a) one orbit (b) after 20 orbits (c) after 3 months (d) after 4 years [2]. The SSN is tracking the largest pieces of collisions and can figure out when and how the fragments originates from. In figure (3.5) it is shown how all of the three satellites' debris was distributed 3 and 5 years after their collisions at July 2012 [1].

[2]Speed above 3 000 m/s

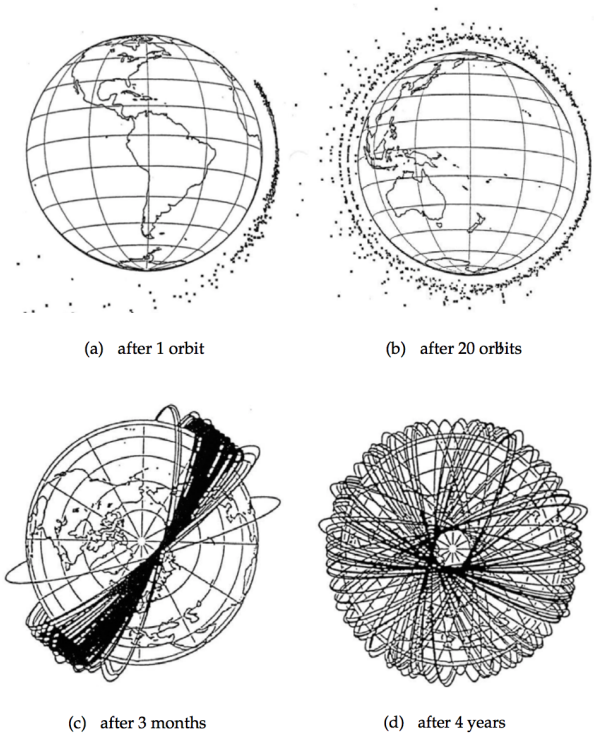

Figure 3.4: How space debris will distribute itself after 1 orbit, 20 orbits, 3 months, and after 4 years [2].

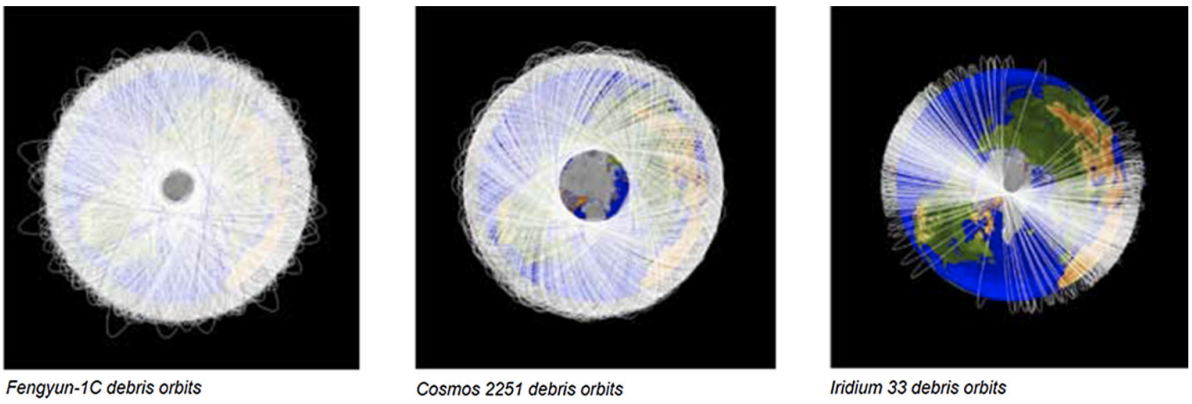

Figure 3.5: The distribution of the space debris of the two worst satellite collisions in history to this date [1].

3.4 Distribution

In GEO the mass is larger due to the fact that the satellites used here are larger. In LEO there are more spacecrafts but they are smaller than spacecraft in GEO. Due to testing, intentional and unintentional collisions and by being a popular orbit, there has been a increase in some of the orbits in LEO. It is assumed to be approximate 750 000 objects larger than 1 cm which is the size of a

Table 3.1: Number of different specification of space debris, January 2017.

Specification	Total
Rocket Launches (since 1957)	5250
Satellites Placed into Orbit	7500
Satellites still in Space	4300
Active Satellites	1200
Tracked and Cataloged Space debris by SSN	23 000
Number of break-ups	> 290
Total Mass of All Objects in Orbit (kg)	7 500 000
Estimated Space debris (> 10 cm)	29 000
Estimated Space Debris (1 cm to 10 cm)	750 000
Estimated Space Debris (1 mm to 1 cm)	166 000 000

marble, and approximate 20 000 objects larger than 10 cm which is the size of a tennis ball, but there is assumed to be over 166 000 000 objects larger than 1 mm in orbit which is the same size as a rough sand corn. More number of different specification of space debris is found in the table (3.1).

As seen in figure (3.6) the mass has increased with 2000 ton every ten year since 1980, and still increases. This is diveded into four categories, the blue line indicate spacecrafts, the green line is rocket bodies, the pink line is the fragmentation debris, and the orange one is the mission related debris. These are more described in the the section (3.5) which undergoes the contents of the debris and what each category consists of. The total mass of objects in orbit is about 7500 tons which is roughly the same as the population of Tromsø and Harstad[3] [1].

[3]Population in 2018.

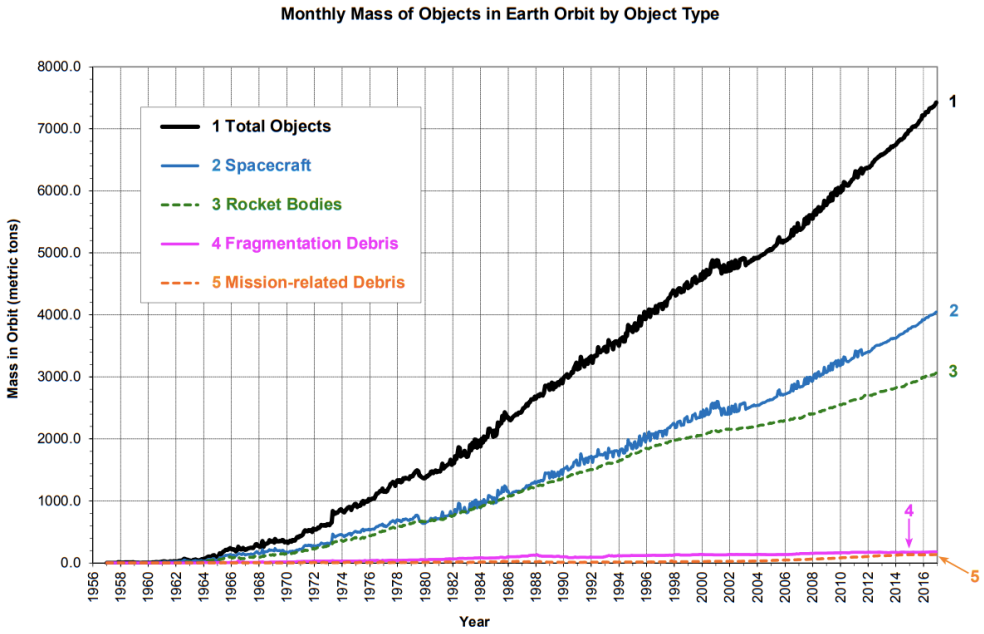

Figure 3.6: The graph shows the mass evolution of all objects from the first satellite in space in 1957 and until 2017 and what it consists of. The black line (1) shows the total of all the objects, the blue (2) shows number of spacecrafts, the green (3) is the number of rocket bodies, the pink (4) shows the fragmentations from break-up events due to collisions, the last orange one (5) shows all the mission related space debris. [1].

3.4.1 Altitude

In LEO, the largest spatial distribution of objects is at heights of 800 km at ($i = 98°$), 1000 km at ($i = 82°$) and at 1400 km since here it is the most convenient height for remote sensing satellites. This is shown in figure (3.7a) whereas figure (3.7b) shows the next highest spatial density of objects is in MEO at approximately 20,000 km altitude and in GEO at approximately 36,000 km.

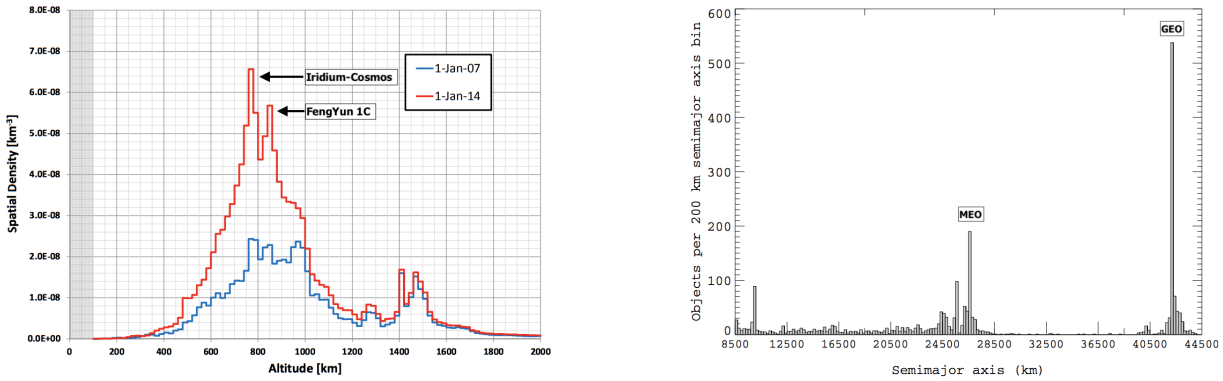

(a) LEO **(b)** MEO and GEO

Figure 3.7: Figure (a) shows the distribution of LEO cataloged objects before vs. after the two worst collisions occurred [1]. Figure (b) shows the distribution in MEO and GEO catalog objects with the semimajor axis of their orbit (class width: a = 200 km; status: June 2003) [2].

The spatial distribution is largest in the LEO, but as well it has grown larger at the polar regions over the years as shown in figures (3.2) and (3.8). Figure (3.8) shows the density of the polar regions at the beginning of the space age one year after launch of Sputnik-1, at the year 2017, and the predicted density in the year 2055 if the same amount of activity continues as it does this day almost 100 years after the launch of the first satellite in space.

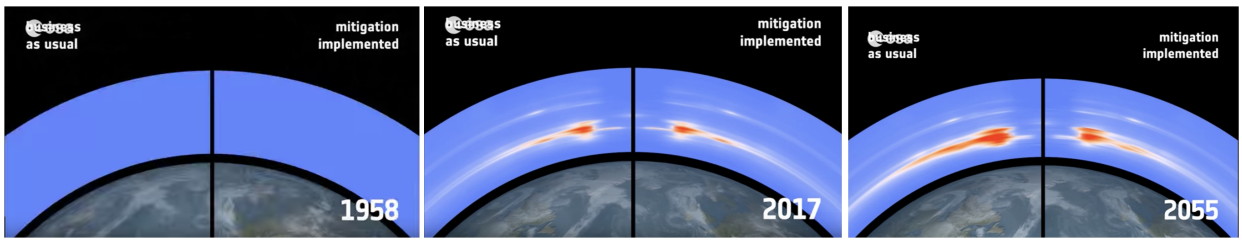

Figure 3.8: Density at the year 1958, 2017, and 2055 in the polar regions. [Photo credit ESA [14]].

3.5 Composition

Space debris consists of all man made objects sent out into space and orbiting the earth, which are now fragments, dead satellites and rockets. What space debris consists of are divided into various of types, these are explosion fragments which are energy sourced objects from the spacecraft; collision fragments which are unintentional or intentional collisions from spacecrafts or missiles; solid propellant objects such as leaked fuel that did not vaporize but instead formed into larger clusters or slag particles; deterioration fragments which are small flakes of either paint, erosion or damages of surfaces; launch hardware consist of objects that were released during detachment of the upper stage rockets; human space castaways are human waste from before they recycled it on the space station, and tools dropped during spacewalks mainly from the space stations, whereas a last thing to mention here under this last category is the human ashes of the creator of Star Trek series Gene Roddenberry that was spread into orbit in 1992 [13, 15]. Some other small objects of debris which despite their size can create damage on spacecrafts are introduced in the next following sections

3.5.1 Paint Flecks

Not all space debris contains fragments of explosions of satellites and rockets. Even though the majority of it comes from this, some contains paint flecks from upper launch vehicles, it doesn't sound like the biggest threat, but those paint flecks actually made a 3-4-millimeter deep crater in the window of the Challenger space shuttle. [2].

3.5.2 Solid Rocket Motor Firings

Solid rocket motors can make slag particles up to 30 millimeter in size when exhausted, this can cause more severe damage than the paint flecks with larger and deeper craters in spacecrafts. The exhaust from the rocket engine may as well cause a disconnection as it did when Ecuador's first CubeSat went into a debris cloud. [2]

3.5.3 Sodium Potassium

It was also found residue of liquid coolant from 16 Soviet RORSAT (Radar Ocean Reconnaissance Satellites) radar satellites' nuclear reactors. It has been recorded between 70 000 - 100 000 of droplets of Sodium Potassium of 5-7 centimeter (thus trackable with radars) between 900 and 950 km at a particular inclination, $i = 65°$. Making them the largest threat of all particle exhaust coming from rocket engines. The observed droplets is shown in figure (3.9) and is marked with red [13].

3.5.4 Anomalous

Another event of space debris coming from spacecrafts is more of a mysterious one called an anomalous event. Parts from spacecrafts is being released for unknown reasons, but may still function, or they are not possible to find their originate. An example of this is NASA's COBE satellite which released 76 fragments for unknown reasons, but is still fully functional. [13].

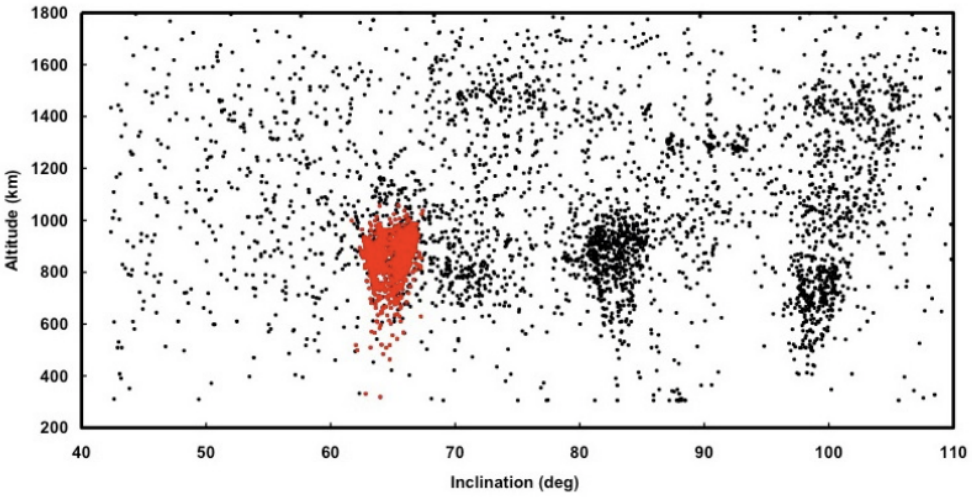

Figure 3.9: Droplets of Sodium Potassium from Soviet spacecraft nuclear reactors observed in $i = 65°$ at around 900 km altitude highlighted in red [13].

3.6 Risks and Impacts

Debris orbits around the earth at an enormous speed of 10 km/s obtaining a high amount of kinetic energy. For example, a coin that weighs 5-gram has a kinetic energy of 140,625 Joule with this speed. This is ten times faster than a fired bullet, but 100 times more energetic than a bullet fired from a gun. In table (3.2) and figure (3.10) a comparison of the various sizes in LEO, and their respective impact energy, is shown. It was assumed that each object has the mass and kinetic impact energy of an aluminum sphere ($m_{al} = 2.7g/cm^3$). The kinetic energy, E_k, is found by the mass divided by half the velocity of the object by the equation:

$$E_k = \frac{1}{2}mv^2 \tag{3.1}$$

Table 3.2: Comparison of everyday object if they where in LEO with typical LEO impact speed of 10 km/s.

Debris Size	Similar in size to ...	Mass (g)	Kinetic Energy (J)	Energy similar to...
1 mm	Sand Corn or Poppy Seed	0.001	70	Pitched Baseball
5 mm	Push Pin	0.04	2,000	A Bullet
1 cm	Marble or Blueberry	1.4	70, 000	Falling Anvil
5 cm	Golf Ball	180	9,000,000	Hit by a Bus
10 cm	Tennis Ball or Baseball	1,400	70,000,000	Large Bomb

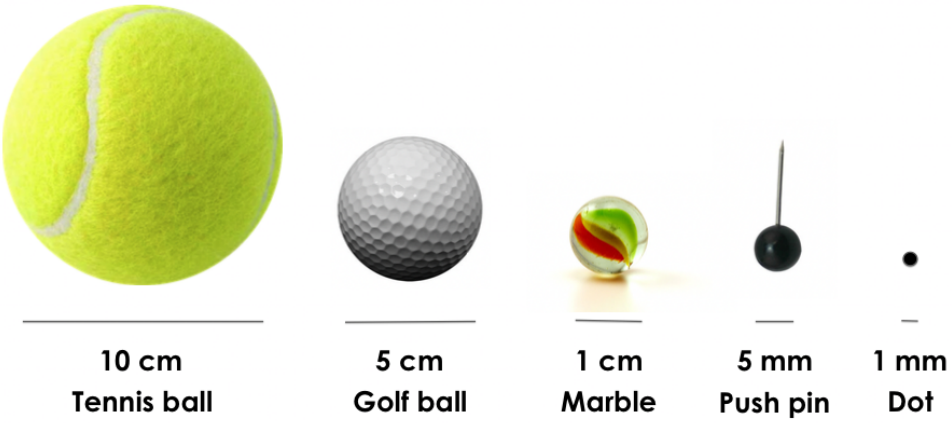

Figure 3.10: A visual comparison of the smallest sizes of space debris with everyday objects as in table (3.2)

A real world reminder of the threats imposed by space debris is the recent collision on Sentinel-1A. The Copernicus Sentinel-1A (alt = 693km, i = 98.18°) is a radar imaging satellite operated by ESA and two of its clients is located in Tromsø. KSAT receives the transmission data from Sentinel-1A [16], whilst NORUT is using their data to perform image processing [17]. It is worth mention that these companies uses several of ESA's satellites, which now with the increase of space debris imposes a greater threat of being hit by hypervelocity objects.

On August 23rd it was hit by what is believed to be a five-millimeter sized piece of space debris (which is the same size as a push pins shown in figure (3.10) creating a crater of 40 cm in diameter on the solar panel wing [18]. This is shown and marked with a red arrow in the figure (3.11). Fortunately, the event had no effect on the overall power system and the function of the satellite, so it still operates (almost) fully functionally [19].

Due to its small size, objects of this size are currently not trackable from earth, since only objects larger than about 5 cm to 10 cm are currently tracked with radars, so that collisions can be avoided by maneuvering the satellite. The risk still increases by the number of collisions, and the risk of Sentinel-1A to be hit by fragments of Fengyun-1C is at almost 20%, meanwhile for the Cosmos-2251 fragments (from the iridium-cosmos collision) the risk is at almost 30%. More collision of satellites will increase this risk, making it almost inevitable for the spacecraft to move away [12].

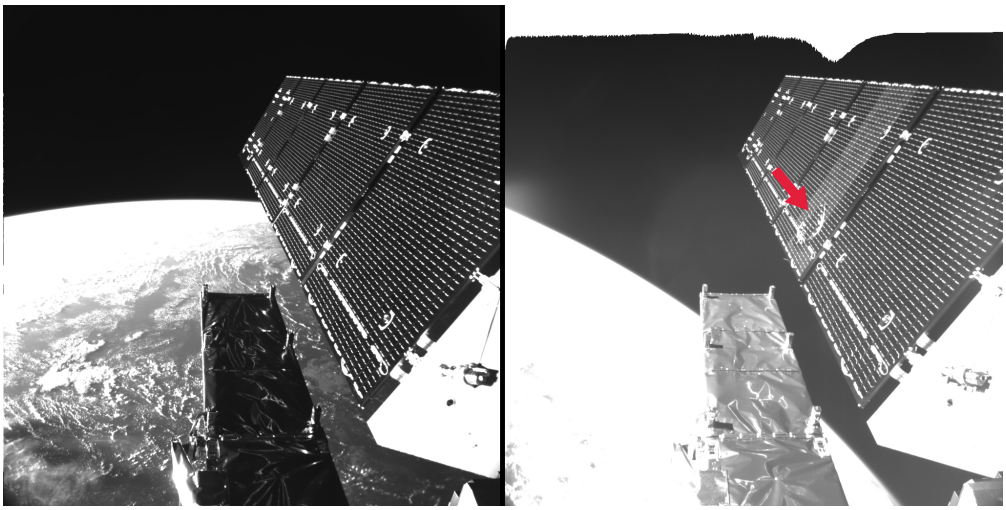

Figure 3.11: The Sentinel-1a impact before and after. The impact is marked with a red arrow in the left picture [19].

Even though the size and the impact of the space debris is known, the risks still has to be lowered in when designing the spacecraft. It is sufficient to make it space proven while considering all possible events that could happen to the spacecraft. This process on how to properly shield the spacecraft in the design process was done by Eric Christiansen [20] in 1992 and is still used today.

From the same article a mathematical description of the limit of different materials hit by objects in either 0 or 45 degree angles at various diameter in size and velocity. This is seen in figure (3.12) that the most critical point is the 0.32 cm object with a velocity of 6.50 km/s.

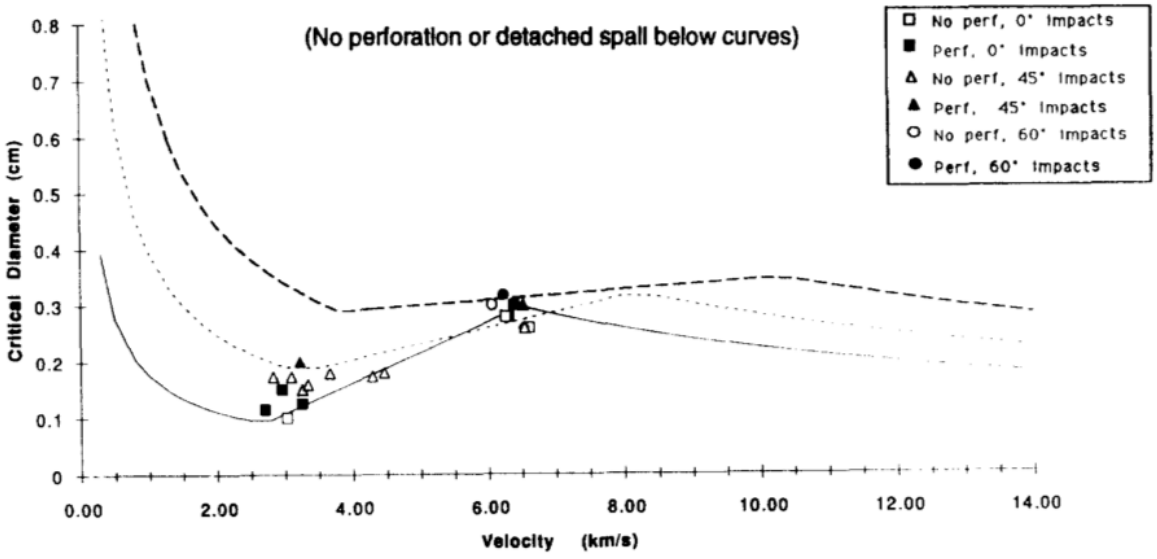

Figure 3.12: A diameter and velocity diagram of different material strengths and their redundancy against different sized objects and their corresponding velocity. [20]

The impact of destruction this critical point can do is shown in figure (3.13). Here an impact test of a glass projectile of diameter 0.32 mm with the velocity of 6km/s is done to several thick

aluminum plates varied in thickness from (left to right) 1.0 cm, 2.4 cm, 2.8 cm, 3.4 cm, 3.9 cm, and 10.0 cm. It is seen here that it the thickness is important in shielding the spacecraft, even though the space debris object is only 0.32 cm. The shape of the object creates different impacts craters. The picture below shows the impact crater of various shapes the space debris may have, and how a rectangular horizontal or vertical flat shape, or a spherical shape makes different craters in both size and depth.

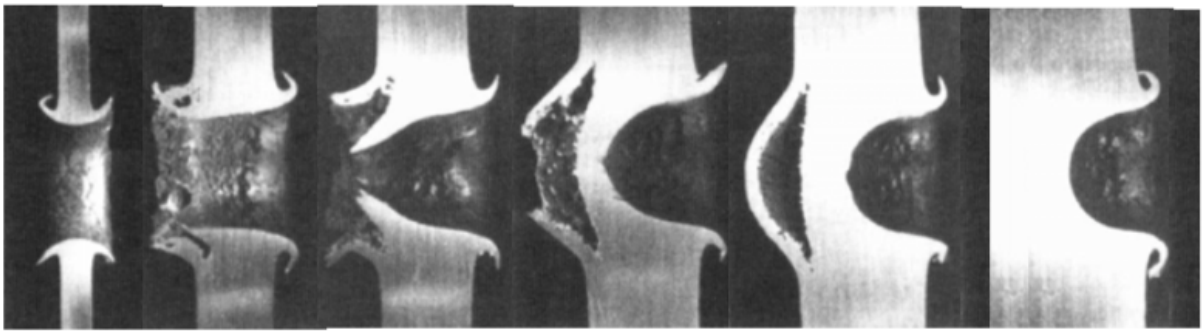

Figure 3.13: A test done to a single wall and how the impact damages on aluminum plate with different thickness. The glass projectile had a diameter of 3.2 mm with velocity of 6 km/s. The thickness of each wall from left to right: 1.0, 2.0, 2.8, 3.4, 3.9, 10.0 cm. [2]

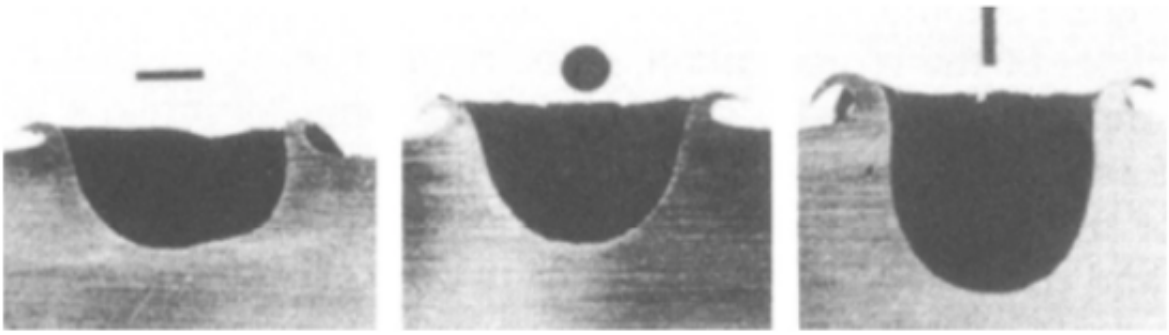

Figure 3.14: How a crater looks like after an impact done by different geometric objects. [2]

3.7 Reentry

Reentry into the atmosphere is the only effective method to remove space debris due this date. The atmosphere drags down objects in the lowest orbits of around 200 km, and will start to break-up at an altitude of 70 to 80 km [21]. As seen in the graph (3.15) the yearly amount of reentries is nothing compared to the amount of space debris orbiting the earth. On average it de-orbits only approximately 400 objects worldwide, which includes not only space debris but also rocket bodies, platforms and payloads [22]. This compared to the estimated 166 million objects still out there, which is basically nothing. The footprint of a large object re-entering the atmosphere requires a field of 2000 km long and 70 km wide. Even then it will not fully be dissolved in the atmosphere. Such as large fuel engine tanks and other large objects from spacecrafts will not fully burn up. After a

series of reentry events of nuclear materials on board spacecrafts ended up spreading nuclear waste on ground, so restrictions had to be made to forbid these from entering the atmosphere, resulting in no use of atomic fuel or material on-board any spacecrafts in LEO. Reentry is a dangerous risk for humans, animals, and buildings on earth. Luckily, no record of humans is killed by space debris, but buildings and houses has been struck. Large spacecraft ascending down to earth is pointed to sink into the ocean as far away from land and humans as possible while smaller once burns up in the atmosphere [2].

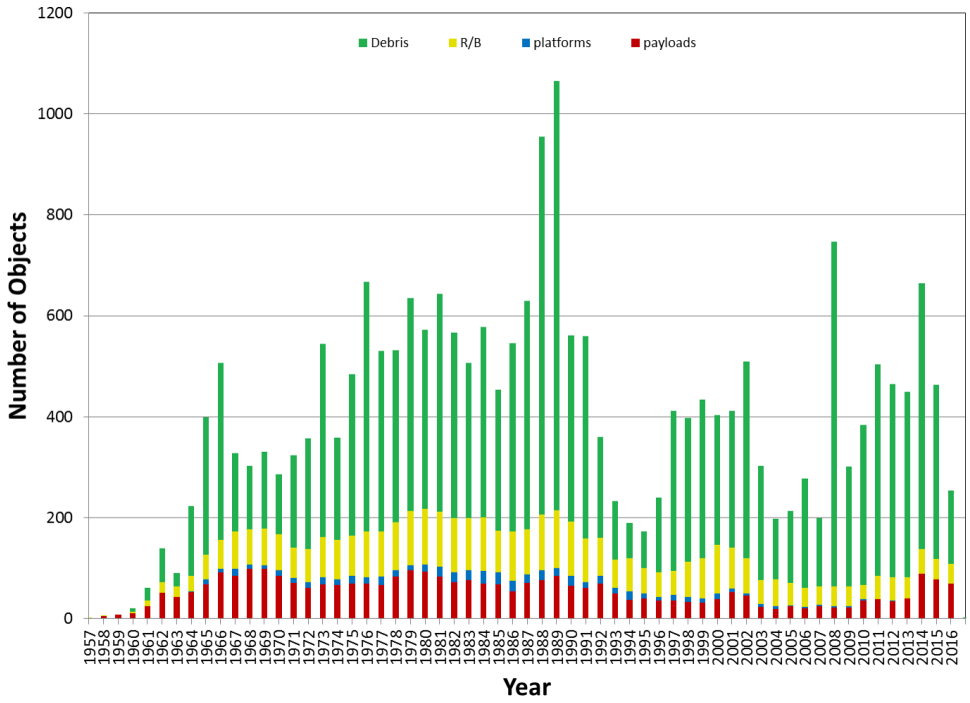

Figure 3.15: Histogram of all the number of objects reentries the atmosphere annually since 1957 and up to 2016. ©The Aerospace Corporation, 1995-2016.

3.8 Detection of Space Debris

The U.S. military Space Surveillance Network (SSN) is the world's most comprehensive space surveillance system and has over 25 sites on the Northern Hemisphere and uses ground based surveillance to track the space debris.

The space debris are being tracked and then stored in a satellite catalog to prevent collisions between spacecraft and the object. SSN can track objects at 10 cm in size in LEO and 25 cm - 1 m in GEO making over 750 000 observation per day over 10 cm. The catalog contains around 20 000 objects were 1,000 of them is operational satellites. Other information from other detection sites external from the SSN is used to confirm the catalog.

Both ESA and NASA have to maneuver their spacecrafts once or twice a year. The exact number of active satellites is not public available, but the non-classified onces may be found at space-track.org [5] with their corresponding TLE data [23].

There are three options that exists to detect space debris, this is either using Radar, Optical or Laser. These observes thousands of objects in the various orbits per passing. The radar uses

the signal transit time and Doppler shift to determine the position and the velocity of the object and uses reflected energy for observation. The radar uses the radio waves, the optical telescopes uses sunlight which is reflected from the spacecraft, and the LIDAR uses a narrow high power light beam that gets reflected [2].

3.8.1 Radar

Radar is used in many fields of measurement and detection, such as for remote sensing either from ground or space, as well to localize objects from a great distance by help from radio waves [2]. The radar can either do monostatic (Transmitting and receiving with same antenna) or multistatic measurements were several antennas where one of them is transmitting and receiving with same antenna, while the other one are receiving with the other external antennas. There are various types of radars each for different measurements and purposes. They all transmit micro- or radio frequencies making them sufficient for almost no atmospheric attenuation, independent of the time of day and weather. For the lowest frequencies the ionosphere may attenuate or reflect the signal [2, 24]. The main focus in this thesis will be the use of high power large aperture (HPLA) radars in measuring space debris, and will be explained in depth in chapter 5.

3.8.2 Optical

The optical ground stations (OGS) uses telescopes that are often located at high mountain tops and near the equator. This is to avoid as much light pollution as possible and to get as high as possible to get better measurements. The weather has to be clear, and the measurements has to be done at night. The telescopes uses sunlight that is being reflected from the spacecraft. It may detect objects as small as 10 - 15 cm in size in LEO, and 1 m in GEO. In the future it may also tell what the fragments consists of [2, 25].

3.8.3 LIDAR

Satellite Laser Ranging (SLR) is the use of LIDAR to detect objects in orbit, by firing laser-pulses through a telescope and measures the time taken for the pulses to return to earth which gives a centimeter accuracy. This is feasible if the object has a retro-reflector array which makes the light reflects back again, it is possible if the target don't have it by making other laser stations receive the reflected signal. SLR could also be used to shoot down space debris, the photons would impart a small thrust on the object enough to bring it down in altitude making it de-orbit [2].

3.9 Models of space debris

3.9.1 MASTER-2009

The ESA Meteoroid and Space Debris Terrestrial Environment Reference (MASTER) model statically models space debris and meteoroid sizes from 1 micrometer and 100 meter. Master-2009 is part of ESA's analyzing and prediction program. It is a risk assessment tool and estimates the material density of space debris and predicts its impact fluxes on spacecrafts. The model has been improved over the years since 1995, and the latest version is the MASTER-2009. Objects smaller than 5-10 cm are not easy to detect, so by comparing measurements with the model it makes the prediction more accurate. To study the evolution of space debris with a long-term forecast to determine future trends analysis may be preformed using ESA's DELTA tool (Debris Environment Long-Term Analysis). It uses the ESA MASTER model and the break-up model EVOLVE 4.0

developed by NASA to forecast the future trend since collision events are triggered statistically as well the Program for Orbital Debris Environment Modeling (POEM) to include all the historical events including the assumed events. [26]. The master model uses the period ranging from 1957 and to 2060 to simulate the present and the future. The result is compared with measurements from the TIRA radar and the EISCAT radar using the Program for Radar and Optical Observation Forecasting (PROOF) tool [2, 24]. Objects below 1 cm is not easily detected with radar and it is estimated to be around 166,000,000 of these objects. [1]. The MASTER model predicts the space debris that is not detected by the SSN, and statistically predicts its velocity, area-to-mass ratio, material density and impact flux. It is calculated as the mean number of collision, c, that is equal to the impact flux times the collision cross-section area, A_c, times the propagation time, Δt, gives the equation [2]:

$$c = vDA_c\Delta t, \tag{3.2}$$

where $F = vD$ is the impact flux. The probability of being hit is found by Poisson statistics where the probability of one or more impacts is hence the complement of no impact given by the equation [2]:

$$P_{i\geq 1} = 1 - \exp[-c] \approx c, \tag{3.3}$$

where $P_{i\geq 1}$ is the Possion statistic equal to one minus the exponential of the negative mean number of collision, gives the approximately mean number of collision which measures the impact flux and the corresponding fluency of the particles, where $P_{i=n}$ is the number of impact and $P_{i=0}$ is no impact. The MASTER-2009 defines a 3-dimensional time varying space debris environment. This ranges from LEO and all the way to the graveyard orbit outside GEO [2], [27].

3.9.2 ORDEM 3.0

NASA also has a similar model, which is called ORDEM (Orbital Debris Engineering Model). These two models work in similar manners were both of them uses top level functions in their software, and analysis, and pre-derived population files. The ORDEM 3.0 uses the LEO-to-GEO Environment Debris (LEGEND) model which includes the historical and projection models to support their predictions in the future evolution of space debris.

3.9.3 Comparison of the Models

All the biggest space agencies has their own prediction model. The two models that are discussed in section (3.9.1) (3.9.1). One of them, the MASTER-2009, are used in studies done at the university of Tromsø. A comparison of all the models is done in by Liou in [9]. A prediction of the spatial density in 200 years is shown in figure (3.16) with all the prediction models of the greatest space agencies compared to the environment in year 2009. ESA has an analysis and prediction program to model and catalog space debris. This is maintained and updated through DISCOS database (Database and Information System Characterizing Objects in Space), with collaboration with the US Space Surveillance Network (SSN) which tracks all objects in LEO and in GEO and catalogs them. DISCOS is characterizing all launch information, registration of the details of the object, launch vehicle descriptions and the spacecraft information for all trackable and unclassified objects. It takes part in preventing collision avoidance and re-entry analysis [27].

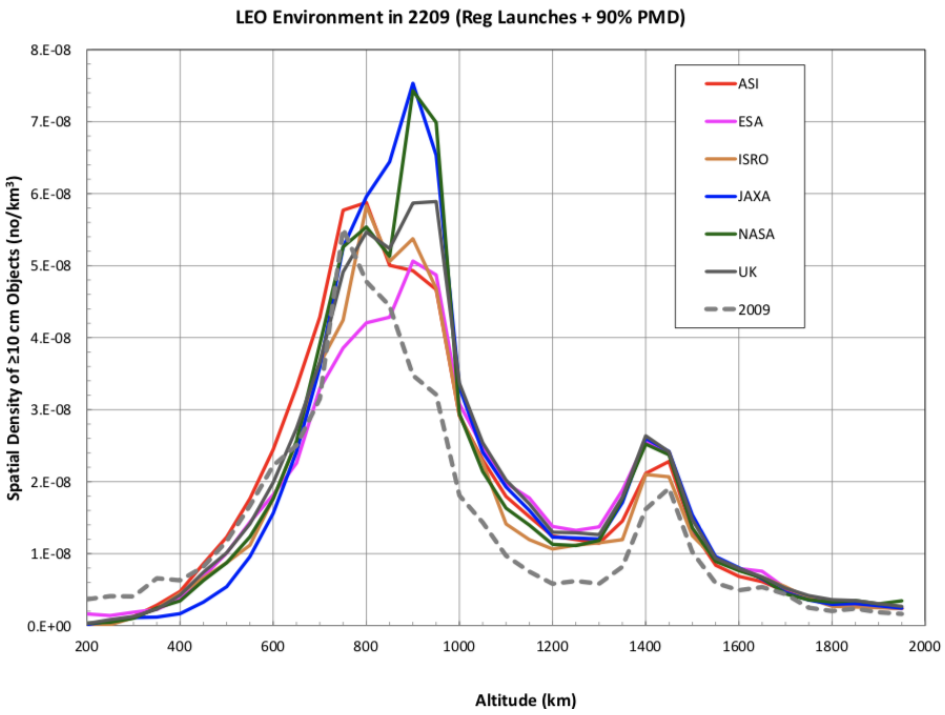

Figure 3.16: The initial and projected LEO environment in 200 years. The red line is the Italian Space Agency (ASI), The pink line is the European Space Agency (ESA), the brown line is the the Indian Space Research Organisation (ISRO), the blue line is the Japan Aerospace Exploration Agency (JAXA),National Aeronautics and Space Administration (NASA), The United Kingdom Space Agency (UK), and the last gray stippled line is the spatial density in the LEO environment in 2009 [9].

Both ORDEM and MASTER include intact objects, and various of types of debris (fragments, anomalous, and debris that has been degraded due to atomic oxygen and erosion), they both get their large input data from the SSN, and use in-situ detectors, radars, telescopes and LIDARs, to identify their model. However, for the smaller critical sizes the ORDEM 3.0 do not model in GEO, due to no confirmed tracked objects smaller than 1 m, and those smaller than 1 m is considered originating from the transfer orbit, GTO. ORDEM 3.0 uses the known density of different space debris material while MASTER-2009 includes all of types of space debris such as meteoroid and solid rocket dust and slag particles, fragments from collisions and explosions, launch, droplets, paint flacks, multi-layer isolation. In the comparison of the two models this is possibly the reason for mismatch between these two models in the 10 cm region. However for 1 m objects the two models match very well due objects being easily trackable rather than the smaller objects. For smaller objects in the critical size the two models deviate depending on the orbit, but match rather very well. [28].

3.10 EISCAT and Space Debris

The EISCAT UHF can measure objects at the size of a coin or a marble (1 cm) at a distance of 400 km to 1500 km. The polar orbits contains the most space debris of any orbits in this inclination and at in an altitude of around 800 km as shown in figure (3.8). The fact that it can measure this makes EISCAT UHF a remarkable instrument in detecting and tracking space debris. The next chapter

(5) will go through this more in depth. The figure (3.17) is made by Juha Vierinen illustrates the total field-of-view (FOV) when the beam is steered into various azimuth and elevation angles with the EISCAT 3D in Tromsø radar can measure marked in green, and all the modeled space debris marked in white. The yellow is the low earth orbits [3].

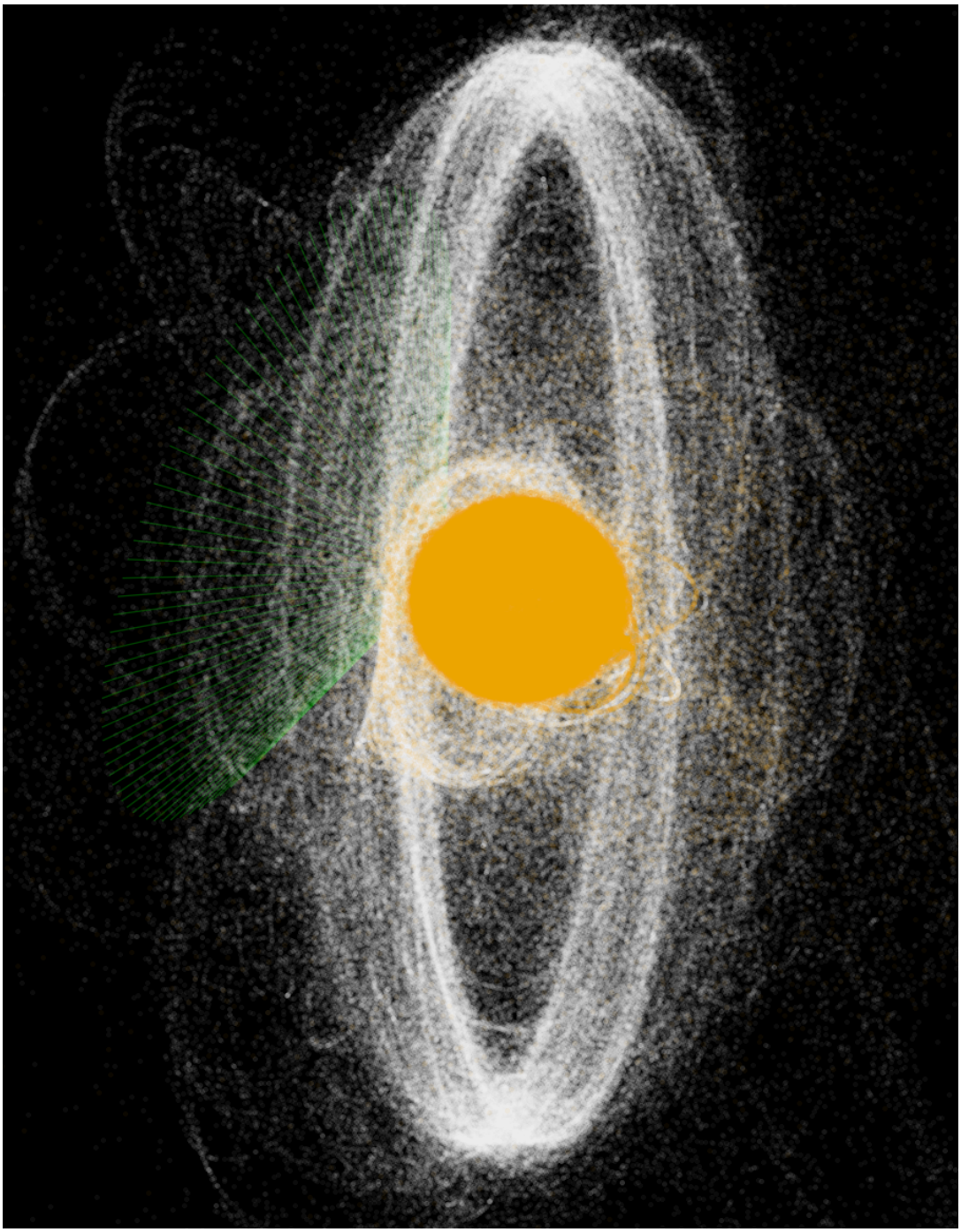

Figure 3.17: Total FOV of EISCAT 3D where the green lines indicates the various types of angle the beam can be steered in, with all the predicted space debris (white) where the low earth orbit is marked in yellow [3].

3.11 The future

After space has become available for public and commercial companies, space missions have had a major growth the later years. What the future outcome will be strongly depends on the policies made in the near future. The quantity of future launch activities is planned to almost explode compared to what is the normal annual launch rate. Space debris is not decaying fast enough, so major goal in the future is to remove dead satellites and to figure out what to do with the smaller parts. By doing so, the risk of cascading collisions decreases.

3.11.1 Policies

There has now been restriction after the intentional collision of the Chinese satellite Fengyun-1C. The international law of space also states that the owner of the satellite is responsible of getting rid of the satellite in the most safe and least risk way [29]. The law of Norway also states that it is a high priority in ensuring the space environment is safe from space debris and that Norway has to take part in helping out on this problem by going under the guidelines set by the international law of space to lower the risk of increasing unnecessary space debris [30,31]. Norway does not have a lot of satellites in orbit. The Norwegian Defence Research Establishment (Forsvarets forskningsinstitutt – FFI) have five CubeSat, the AISSat, but AISSat-3 got lost during a failure in the launch in Russia, but the other two still orbits, and they have two NorSat CubeSats. Telenor has 7 THOR satellites in GEO, where the first of them is now in the graveyard orbit. Last, there is built several student CubeSat satellites by UiT Narvik, NTNU Trondheim, and UiO Oslo, not all of them launched, however those who was did not work [5].

Some example of this is the upper stage rocket break-ups has been improved over the years to decrease the release of unnecessary parts, atomic fuel is no longer allowed in the LEO due to safety.

3.11.2 Launch activities

Over the next ten years SpaceX, Boeing, OneWeb and Samsung are planning to launch over 12 000 satellites almost a mass of 1 ton. All at altitudes between 1 100 km and 1 400 km. This will present an increasing challenge. Figure (3.7a) shows that these regions are some of the lowest regions of density. These region will increase after these 12 000 are inserted into these orbits. These are small satellites, but yet, they will then fill this region and increase the density here, but it is also worth mention that these companies also works on efficient solutions to get rid of these satellites after their EOL.

3.11.3 CubeSat

In the recent years, there has been a change in paradigm, with satellites becoming smaller and more plentiful. The more launches there are, the more debris will be produced. [32]. Since the launch of the first CubeSat in 2003, they have increased in popularity due to the low cost in building and launching them. CubeSats are small light-weighted satellites usually built for one or two mission purposes with the cube-size of 10x10 centimeters. They usually only last for one to five years. They have made it able for academics, universities, and countries to get involved and working with satellite missions and analysis. Some of them are launched by the International Space Station (ISS), or by stage rockets, by just inserting it in a cage containing a spring feather that will shoot the CubeSat out into orbit. Hundreds of CubeSats has been built and launched since 2013, and in February 2017 India set a record in launching 104 CubeSats [33]. The amount of space debris caused by CubeSats is heavily debated, so in order to decrease the risk of increasing the volume of

space debris even more the CubeSats are often installed with sails to help it de-orbit faster, and with blinking morse-coded LEDs to distinguish them from one another. Few of them are equipped with an attitude control system with thrusters. This helps the CubeSat to extend its lifetime, since most of the them de-orbits due to atmospheric drag. [34].

3.11.4 Active removal

Policies each satellite distributor has to follow states that is has do clean up after itself. Several proposals has been made on how to effectively remove space debris, starting with the largest pieces first. [13]. They are all inspired by the same method fishers catches fish, with harpoon or fishnet. Objects induces a small magnetic field when in orbit and tases the spacecraft with a small potential voltage the object loses momentum and decreases in altitude. There are several project proposals in making due this date, such as "CleanSpace One" which is a CubeSat project designed to clean out space debris (see figure 3.18) by ESA done by The Swiss Federal Institute of Technology in Lausanne. [35]. These catches the debris with a claw using a ion propulsion system as thrusters. Another examples of proposal is shown in figure (3.19) where it is used different methods such as fishnet, taser, or laser to either catch the object or to decrease its momentum to lower it to de-orbit into the atmosphere [13].

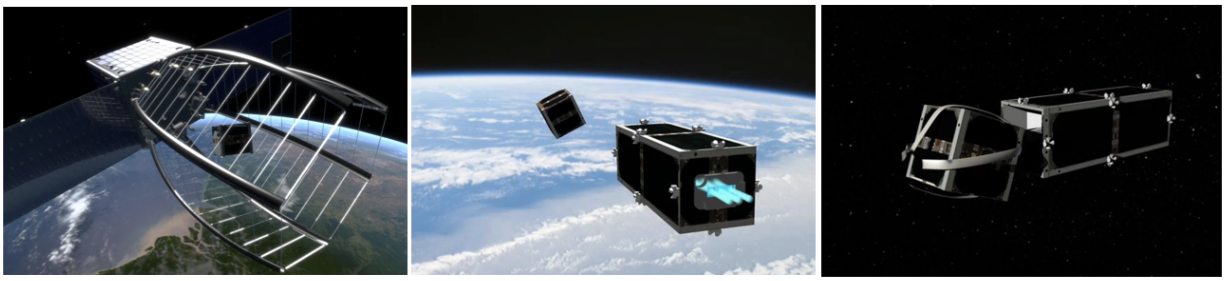

Figure 3.18: An artist illustration of removing space debris by CubeSats by the CleanSpace One Project. [35].

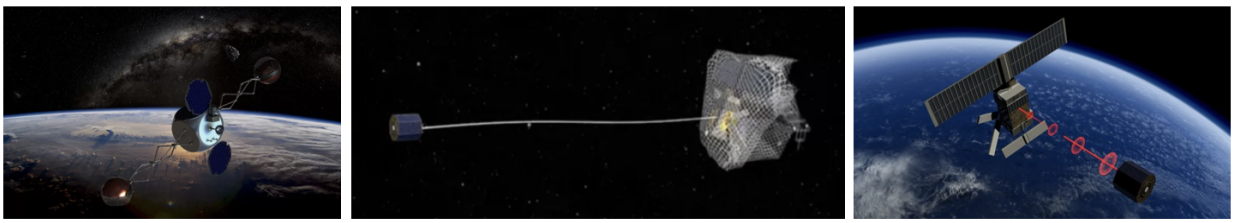

Figure 3.19: An artist illustration of removing space debris proposals by spacecrafts. **From right:** Sling-Sat Space Sweeper (4S). **Middle:** e.Deorbit by Esa. **Left:** Laser Satellite. [13].

Ground based LIDAR is used to track space debris from earth to decrease the targets momentum and making it de-orbit faster into the atmosphere. ALOMAR at Andøya, Nordland, Norway is planning to use their LIDAR in optical tracking of space debris [36]. Other ideas to decrease the velocity of the space debris is by firing ion thrusters at the space debris to slow it down so it will de-orbit and burn up in the atmosphere.

Chapter 4

The Atmosphere

This chapter will go through the benefits of using radar and what happens to the signal when it propagates through the atmosphere and what causes the attenuation.

Our eyes only see through the atmosphere at a wavelength where it is effectively transparent. What we do not see, however, are all the different gasses it is filled with, and that they are expanding and contracting as a result of different solar heating. This expansion is actually advantageous, as it stretches up into the lower orbits and drags space debris back down to earth. These orbits are repopulated with debris descending from higher altitudes in a continual cyclic process [2]. The solar heating itself is variable, following an 11-year period, known as the solar cycle.

The atmosphere behaves differently for the various wavelengths in the electromagnetic (EM) spectrum. In the visible part of the EM spectrum the wavelengths scatter differently, like the blue wavelength is shorter and scattered more strongly than the longer wavelength such as red, making the sky blue. For different radio-and microwave frequencies the rays do not necessarily penetrate the atmosphere and instead may be scattered in the form of either refracted, or reflected as shown in figure (4.2), [6].

4.1 Attenuation and Reflection

.

Figure (4.1) shows the attenuation of the different frequency and wavelengths used in optical and radar measurements. The amount of atmospheric absorption depends on the wavelength of the signal, this may vary as a function of humidity, temperature, and air pressure. The atmospheric attenuation reduces the signal strength or bends it, depending on the wavelength. The advantages of using radar is the low attenuation and interference with the gases in the atmosphere, making it mainly independent of the weather, the time of day, and location, which are what telescopes consider as disadvantages. Longer wavelengths will be attenuated or reflected by the ionosphere. Shorter wavelengths is limited by resonance with water [37]. However, satellites that uses higher frequencies ranging from S-band and up to Ka-band, have their main attenuation in water vapor (H_2O), which is greater when it rains or snows. When going to even higher frequencies than this both oxygen (O_2) and water vapor will play an important role in the interfering and attenuating the signal. For the lower frequencies such as VHF and UHF there is some small attenuation by the oxygen, but here the ionosphere reflections are strong for these radar bands. No such corrections are even needed for the EISCAT UHF, as we do not need ¡ 1 km range accuracy.

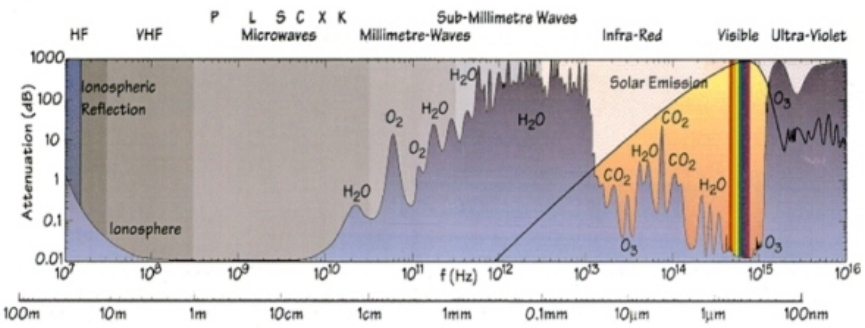

Figure 4.1: Different attenuation of the electromagnetic spectrum ©European Space Agency.

4.2 The Ionosphere

In 1901 was the first time it was achieved to send radio waves 4 500 km overseas by using the ionosphere. It was understood that the atmosphere could work as a mirror at certain frequencies, and radio signals could be transported over long distances by the ionosphere. This is called skywave (see figure (4.2)). The frequencies between 5-30 MHz will be bent by the ionosphere and sent back to earth.

The ionosphere is part of the upper atmosphere and it is ionized by solar radiation, producing free electrons. It ranges from around 100 km and extends up to 1 000 km. However, the ionosphere is part of the thermosphere which expands and decreases by the solar activity making it unstable to use for communication [6]. As seen in figure (4.2) certain frequencies will either be reflected or refracted back to earth or into space, called ray bending. For frequencies higher than 1 GHz, no perturbations will distort the signal. Frequencies above 30 MHz will be refracted and error corrections must be done. Frequencies below the peak plasma-frequency are reflected back, because the ionosphere behaves as a conducting surface for frequencies $f \leq f_p$ interfere with the plasma frequencies and are reflected back to earth. Assuming a neutral atmosphere with no collisions or magnetic field, the transmitted frequencies passing through the ionosphere have to be larger than the plasma frequency $f \gg f_p$, where f_p is the plasma frequency, which is normally around $f_p = 10\text{MHz}$. The plasma frequency is dependent on the electron density, N_e in the ionosphere [3].

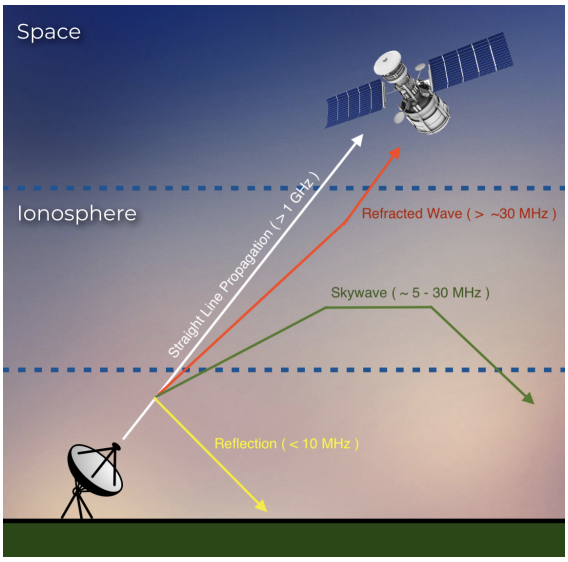

Figure 4.2: Radio signals pathway through the ionosphere. For higher frequencies, the less the ionospheric refraction becomes.

With high auroral activity caused by large solar activity, radio waves which passes through an ionized medium may be absorbed. This time assuming an atmosphere with collision and a magnetic field, the transmitted frequencies collide with heavy particles such that the energy is transferred into the medium and thus absorbed from the wave. The total absorption over a path $\int dl$ is [38]:

$$A = 4.6 \times 10^{-5} \int \frac{N_e \nu}{\nu^2 + (\omega \pm \omega_L)^2} dl \quad [\text{dB}] \tag{4.1}$$

where the $\omega_L = \omega_H cos\theta$ which is the gyro frequency, ω_H times the angle between the magnetic field and the direction of the propagation of wave, $cos\theta$, and ν is the collision frequency is shown in figure (4.3a). The rate of absorption depends on the number of electron collision frequency, ν, over the oscillations which is the angular wave frequency, ω. The absorption is most sensitive in heights when $\nu = (\omega \pm \omega_L)$ due to the change of electron density. This can vary during the time of the day (figure (4.3b)) and as well for different heights (figure (4.3a)), especially in the D-region at 60 to 90 km which is difficult to measure due to low electron density. Here the collision frequency is proportional to the electron energy and when $\nu \gg \omega$ the $\nu = \frac{3}{2} = \nu_m$ at low heights, and for great heights then $\nu \ll \omega$ and thus $\nu = \frac{5}{2} = \nu_m$, where ν_m is the collision frequency for mono-energetic particles. This is shown in figure (4.3a) which shows curves for specific absorptions at different heights. In figure (4.3b), the International Reference Ionosphere 2007 (IRI) model shows the variation of the electron density for altitudes from 0 km up to 2000 km. It is shown here that there is more electron density in the ionosphere during the day caused by daylight from the sun. This peaks at [3].

When transmitting, the angle which radio waves are transmitted has also an effect on how the waves propagates through the ionosphere. The propagation effect is largest at the lowest elevation angles because of the larger volume of the portion of the ionosphere it has to go through, making the waves bend and/or refract. At the zenith angle (the transmit waves go straight up) the propagation effect is smallest.

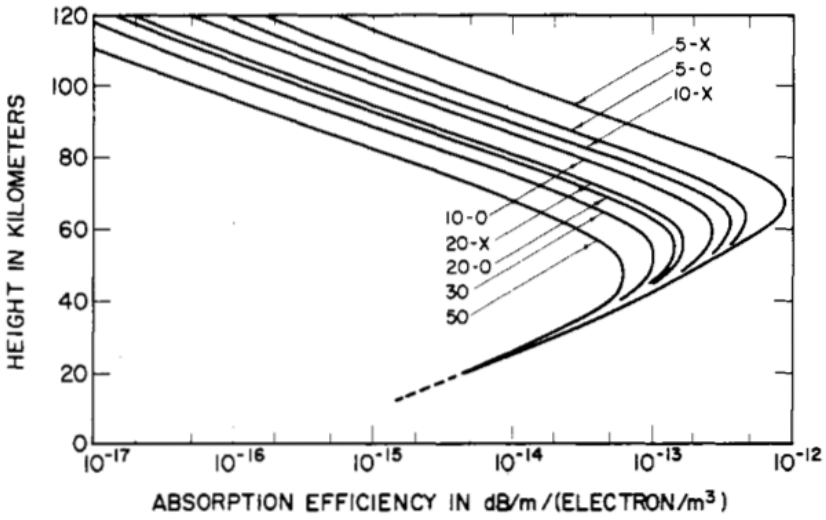

(a) Specific absorption curves in the D-region. © [38]

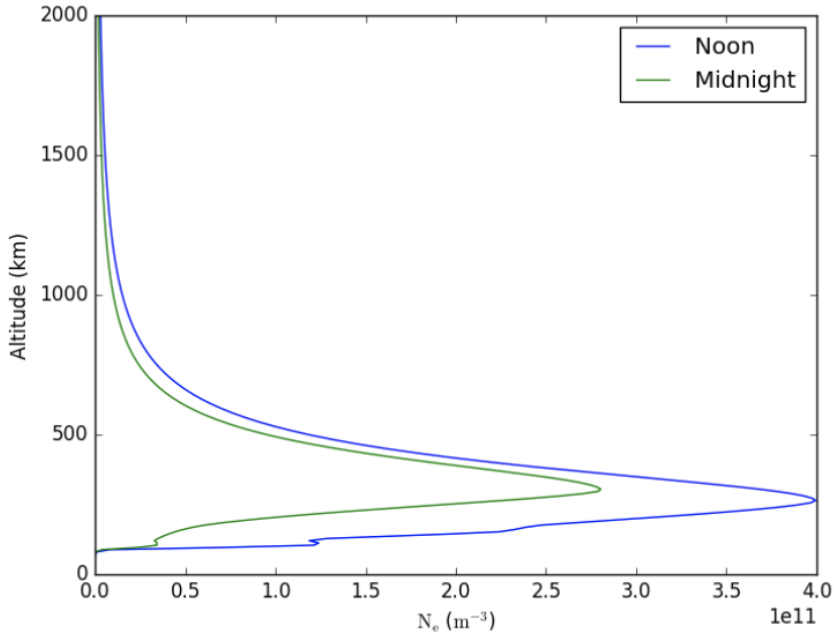

(b) IRI model based electron density profile. © [3]

Figure 4.3: Plots of the ionospheric electron density and the ionospheric absorptions for different heights

Chapter 5

Radar

5.1 Introduction to Radars

Radar is short for "RAdio (aim) Detecting And Ranging". They are used in tracking, measurement and detection, to localize objects from a great distance using radio waves. They are steered using an elevation and an azimuth angle. The advantages with radar is that it do not depend on the weather nor the time of day. This chapter will start by going through the parameters in the radar equation necessary to obtain measurements with it, and how these parameters affect the measurements. A brief introduction of the high power large aperture (HPLA) radars will be presented in order to see the importance of the choice of radar for the debris measurement done in the BPE chapter (7.1).

5.2 The Radar-Equation

The EISCAT radars has powerful klystrons[1] which generates high amount of power to transmit a short duration pulse in UHF frequency propagating through the atmosphere at the speed of light of (approx. $c = 3 \cdot 10^8\ m/s$) to a range of 2500 km with a FOV of 0.7°-1.0°.

Neither of the EISCAT antennas can transmit nor receive simultaneously, so a duplexer ensures the switching between the transmit and receive mode in the antenna; if it did not do this the pulses with its high transmit power with its large amount of energy would then destroy the receivers. A phase array do not have this problem since it can divide its area into receive and transmit mode. When the signal hits an electric conducting surface (some sort of metal) it reflects the signal and which is received by the same antenna that transmitted it (monostatic). This is more carefully described as the radar cross section in section (5.4).

The radar equation can be described as the the receiving power P_r:

$$P_r = \frac{P_t G_t G_r \lambda^2 \sigma_{RCS} A^4}{(4\pi)^3 R^4} \tag{5.1}$$

where the power received is equal to the transmit power P_t, antenna transmit and receiver gain G_t and G_r, the radar cross section, σ_{RCS}, of the target area, times the atmospheric absorption factor, A, which is in this case equal to 1 due to the small attenuation in the atmosphere which will be negligible in this thesis. All of this over the loss terms which are the distance from the radar to the target and back again to the radar, $1/R^4$, and the wavelength, λ, and 4π.

The receiving gain G_r is

[1] Klystrons are high power vacuum tubes which generate or amplifies the transmitted wavelengths

$$G_r = \frac{A_e 4\pi}{\lambda^2} \tag{5.2}$$

which is described as the effective aperture, A_e, of the antenna which describes how good the antenna is, this over the wavelength, λ of the signal.

5.3 Signal-to-Noise Ratio

When measuring scientific experiments with the antenna, the signal to noise ratio (SNR) is used to describe its sensitivity and its ability to measure a target. In figure (5.1) the SNR is illustrated as the echo signal strength. It shows when a target hits the antenna beam, the instrument echo strength varies inside the beam. The signal is strongest in the middle of the beam, which is marked with the red line-of-sight (LOS) showing a higher response (green) in the spectrum than when the target hits the side of the beam. The signal is strongest in the main lobe in the on-axis position (the center of the beam), and smaller when off-axis, due to smaller antenna gain. When outside beam, no echo is returned.

Big spacecrafts usually has a large radar cross section and reflects large amount of energy. So the chances of it to be detected by one of the sidelobes is high. Smaller objects do not reflect as much and are detected only within the main lobe of the antenna beam pattern. This is one of the reasons most of these radars are placed far from cities and people to avoid disturbances and inferences such as from mobile and radio which can increase the noise level, N, which can cause the signal to drown in the noise, and thus detections may be lost.

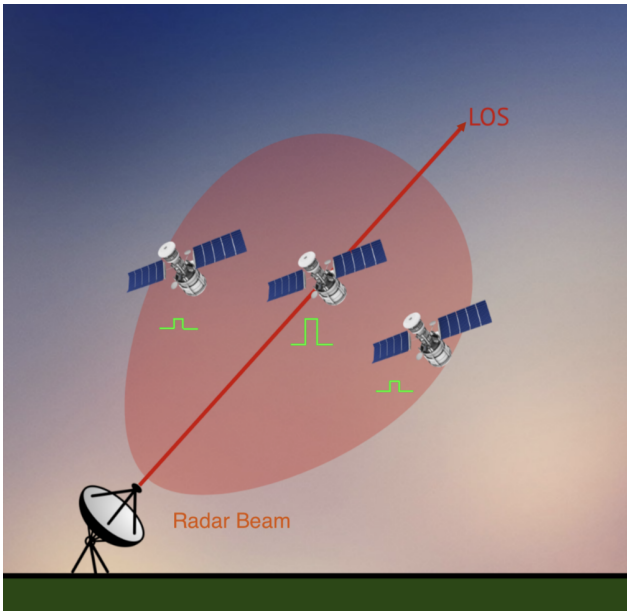

Figure 5.1: Illustration of the radar beam hitting a target when it flies through the beam and its echo strength. The red line is the line-of-sight of the beam and is at maximum strength.

The SNR is described as the power received over the background noise power, N:

$$S/N = \frac{P_r}{N} = \frac{P_r}{k_b B_r T_s} \tag{5.3}$$

where the noise is described as a function of Boltzmann constant, k_b, system noise temperature, T_s, and the received bandwidth, B_r. By inserting the radar equation (5.1) into the SNR equation (5.3), the following SNR is thus:

$$S/N = \frac{P_t G_r G_t \lambda^2 \sigma_{RCS}}{(4\pi)^3 R^4 k_b T_s B_r}, \tag{5.4}$$

Figure (5.2a) shows the beam pattern formed as an airy function indicating the strength $G(\Theta)$ depended of the beams geometry. The figure (5.2b) shows the beam pattern on the side giving a more descriptive representation of the beam strength $G(\Theta)$.

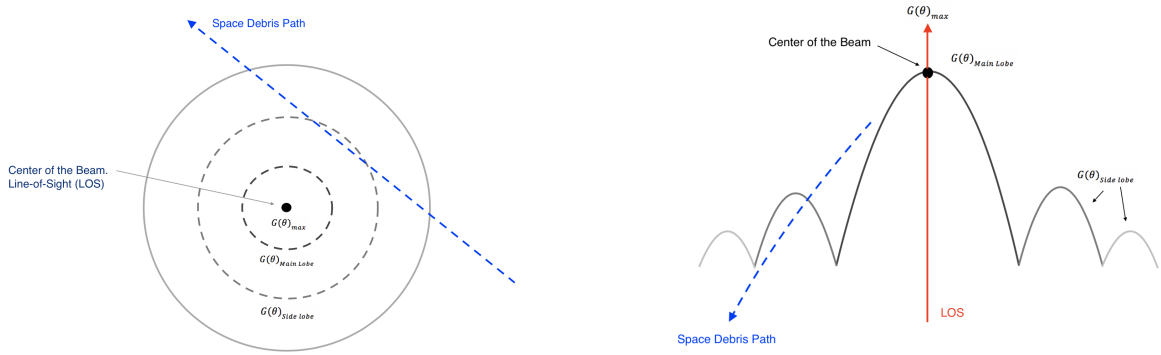

(a) Beam from the top. **(b)** Beam from the side.

Figure 5.2: The figures shows the beam pattern and its strength in gain. The blue dashed line shows the space debris path going through the beam. The signal is strongest in the center of the beam, and decreases for each sidelobe.

5.4 Radar Cross-Section

The ability of a target to reflect energy is characterized by the radar cross-section (RCS), σ_{RCS}. How much an object reflects per unit area depends the the angle of incidence of the radio wave θ and its wavelength, λ. However, a large object can still give a small RCS, such as a stealth bomber. Likewise, a small object can have a large RCS, such as a corner reflector [37]. To simplify the calculation it is assumed that all targets are a perfect conducting spheres.

The RCS can be described by figure (5.3) which shows the different scattering domains for the respective wavelength and size of the object. The minimum detectable size of an object for EISCAT is added here, as well the range for the HPLA. The Mie and resonance scattering is not considered here, so the two main focus will be Rayleigh and optical regime. Figure (5.3) can be described by the formula:

$$\frac{\sigma_{RCS}}{\frac{1}{4}\pi d^2} = \begin{cases} 9\left(\frac{\pi d}{\lambda}\right)^4, & \text{when d} < \frac{\lambda}{\pi\sqrt{3}} \\ 1, & \text{when d} > \frac{\lambda}{\pi\sqrt{3}} \end{cases} \tag{5.5}$$

This equation tells when the Rayleigh regime stops and goes over to optical regime. It stays in Rayleigh as long as the wavelength is larger than the target. When the wavelength decreases in

size and becomes smaller than the target it goes into the optical region [3, 37].

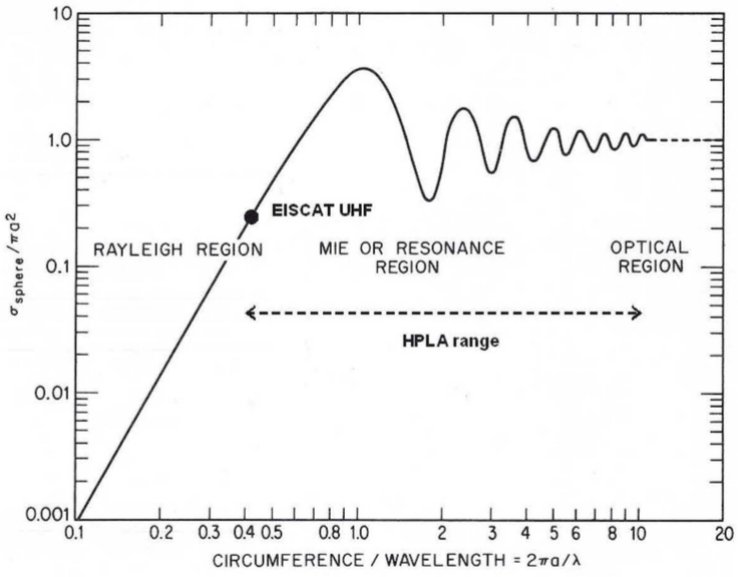

Figure 5.3: Different domains for the radar cross-section [2, 39]

To explain figure (5.3) more clearly, a comparison of three EISCAT radar systems with different wavelength is shown. The modeling done in figure (5.4) shows the different wavelengths transmitted by EICSCAT UHF at Svalbard and Tromsø, and the upcomming phased-array, EISCAT 3D, they use the wavelengths $\lambda_1 = 0.32m$, $\lambda_1 = 0.60m$, $\lambda_2 = 1.5m$, respectively. The comparison is shown due to detection threshold visually decided with a SNR=1. This is the definition of system noise equivalent diameter. The beampark experiment, however, are done with detection threshold of SNR = 25.

Table 5.1: The min. and max. detectable diameter in the Rayleigh region of the wavelengths in figure (5.4). With $SNR = 1$.

Detection Threshold			
Radarband	UHF	UHF	VHF
Wavelength (m)	0.32 Tromsø	0.60 Svalbard	1.50 EISCAT 3D
Min. Range (km)	300	300	300
Max. Range (km)	8 790	16 740	40 350
Min. Diameter (m)	0.006	0.0080	0.010
Max. Diameter (m)	0.0590	0.110	0.270

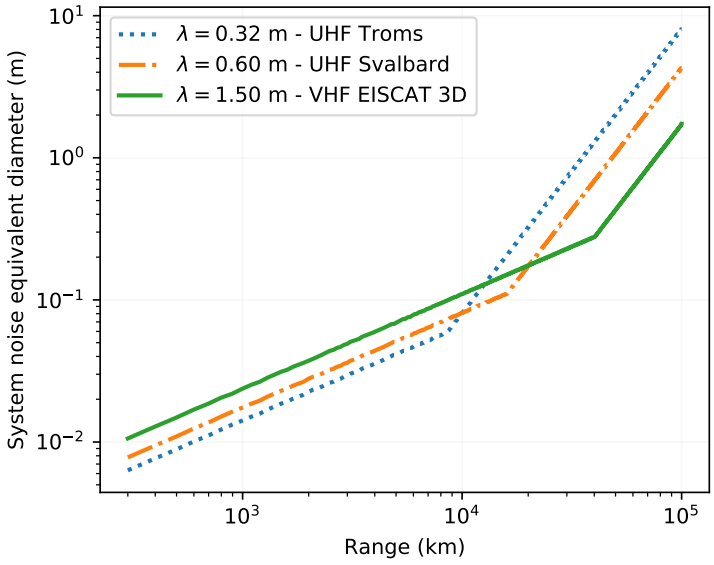

Figure 5.4: Plots of the different domains for different antennas systems with different transmit wavelength with SNR=1.

The larger the wavelength is, the harder it is to measure small objects which is true for the different aperture radars mentioned. Both of the EISCAT UHF radars may detect even smaller diameters than EISCAT 3D. Due to the low frequency used by the EISCAT 3D it experiences more ionospheric propagation effects, however this makes it more sensitive to Rayleigh scatter regime and the wide beam enables it to be more efficient in discovering new objects [3].

5.5 High Power Large Aperture Radars

The Space Surveillance Network (SSN) is tracking and cataloging all space debris object larger than 10 cm in size. However, the deficiency of the SSN is the lack of detection of space debris smaller than 10 cm, so by using the high power large aperture (HPLA) radars, it would make it possible to detect smaller objects between 1 cm and 10 cm. Smaller objects than this is difficult so space debris models has been used (see section (3.9 in chapter (3)) to statistically measure were they are, how large they are, their distribution in range, and what their impact flux of kinetic energy on

spacecrafts could be [27, 28].

HPLA radars (see figure (5.5)) was built for ionospheric research purposes such as incoherent scattering, amongst these are the Arecibo (Puerto Rico), Jicamarca (Peru), EISCAT[2] (Svalbard (N), Tromø(N), Sodankylä (F), Kiruna (S)), Millstone Hill (Massachusetts, USA), Kharkiv (Kharkiv, Ukraine), Poker Flat(Alaska, USA), Irkutsk (Irkutsk, Russia), Resolute Bay (Nunavut, Canada), MU (Shigaraki, Japan). HPLA have a high spatial resolution, a narrow beam (Tromsø and Svalbard 0.5° and 1.0°, respectively), they are sensitive, have high transmit power, and large aperture.

They do not manage to observe all the features of the target, but with the reflected echo strength signal it can derive info about the targets radial velocity (Doppler velocity) and its acceleration, echo-strength and number of events, with its features HPLA manage to detect down to 1 cm in size [2, 39, 40].

An HPLA such as EISCAT use a beampark measurement to track and compare the measured objects with the the prediction model [41]. The data is then used to confirm the catalog and the models. This will be explained more in depth in chapter (7.1).

[2] N = Norway, F = Finland, S = Sweden.

Figure 5.5: Various High Power Large Aperture Radars around the world. Both Phase Array and parabolic radars are shown here. [41].

5.6 EISCAT Radars

The EISCAT Fascility in Ramfjorden, Tromsø, in Norway is part of the European Incoherent Scattering (EISCAT) organization with radar systems in Northern Scandinavia. It is supported by Finland, France, Norway, Great Britain, Sweden, Germany, Japan, and China. It has a UHF and a VHF radar, but this thesis will focus on the UHF one.

The UHF radar is a 32-meter diameter parabolic antenna (see figure (5.6a) transmitting frequency of 930 MHz, ($\lambda = 0.32$) and uses a transmitter of 2 MW. It was moved from 933 MHz to 931 MHz to not interfere with mobile phone system frequency. The UHF antenna in Tromsø can both transmit and receive (monostatic), and there are three other facilities that can either transmit and receive or both with the same antenna (multistatic). In this thesis, only monostatic will be considered.

In Tromsø in February 2002, the UHF radar managed within 4.5 hours to detect 56 objects ranging in size from 0.5 m to 0.019 m in diameter in altitudes from 490 km and up to 1480 km. [24].

The EISCAT radars at Svalbard (figure 5.6b) is placed 8 km from Longyearbyen on a mountain top among other facilities (such as SuperDarn, Northern lights observatory KHO, and etc.). The one used for the BPE has a 32 m steerable cassegrain antenna, transmitting frequencies of 500 MHz ($\lambda = 0.60$ m). It has since 2000 done several of BPE to test the possibility to do these experiments, and since march 2007 space debris measurements has been done with BPE. These two HPLA EISCAT radars with the great sensitivity of their systems, combined with the location so far north in latitude makes these excellent for observation of space debris [42]. The specification of the EISCAT radar system is given in the table (5.2).

Table 5.2: EISCAT Radars

Specifications	Tromsø	Longyearbyen, Svalbard
Location	Tromsø	Longyearbyen
Geographic coordinates	69° 35'N	78° 09'N
	19° 14'E	16° 01'E
Geomagnetic inclination	77° 30'N	82° 06'N
Invariant Latitude	66° 12'N	75° 18'N
Radar Band	UHF	UHF
Frequency (MHz)	931	500
Max. Receive Bandwidth	8	10
Transmitter	2 Klystrons	16 Klystrons
Channels	8	6
Peak Power (MW)	2	1
Average Power (MW)	0.25	0.25
Pulse Duration (ms)	0.001-2.0	0.0005-2.0
Phase Coding	Binary	Binary
Minimum inter-pulse (ms)	1	0.1
Receiver	Analog	Analog
System Temperature (K)	90-110 K	65-80
Antenna	Parabolic Dish	Parabolic Dish
	32 m steerable	32 m Steerable
Feed System	Cassegrain	Cassegrain
Gain (dBi)	48.1	42.5
Polarization	Circular	Circular

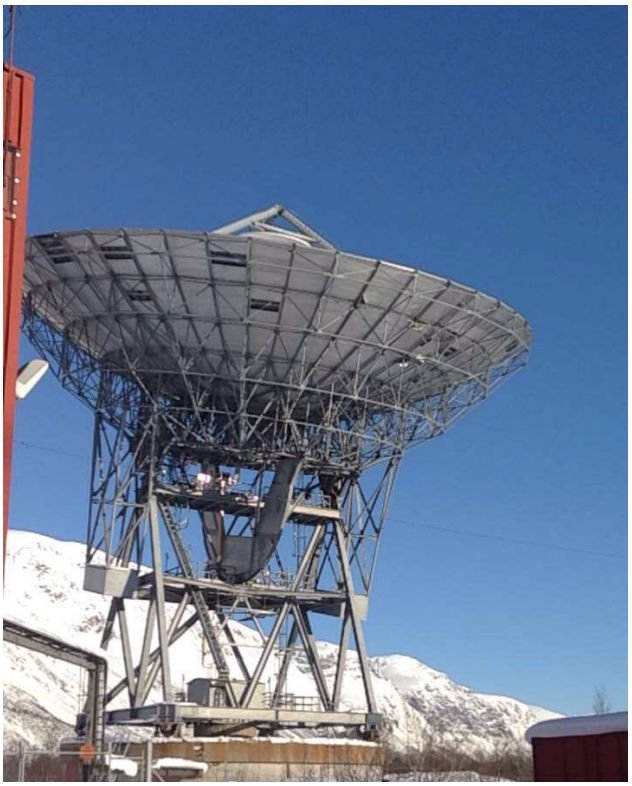

(a) EISCAT Tromsø.

(b) EISCAT Svalbard

Figure 5.6: EISCAT UHF radar antennas used in the beampark-experiment.

Chapter 6

Measurement techniques

This chapter will briefly explain how all the parameters for the beampark experiment are measured.

6.1 Point-Like Target

Figure (6.1) shows how a measurement by the EISCAT radar is done. The point-like target is used to describe the space debris trajectory which have a small range extent, and a high radial velocity. It transmits pulses with a high transmit power, a duty cycle of 5% - 25%, and a radar wavelength λ. The radar pulse is encoded differently each time it is transmitted, and it is feasible to distinguish each transmitted pulses.

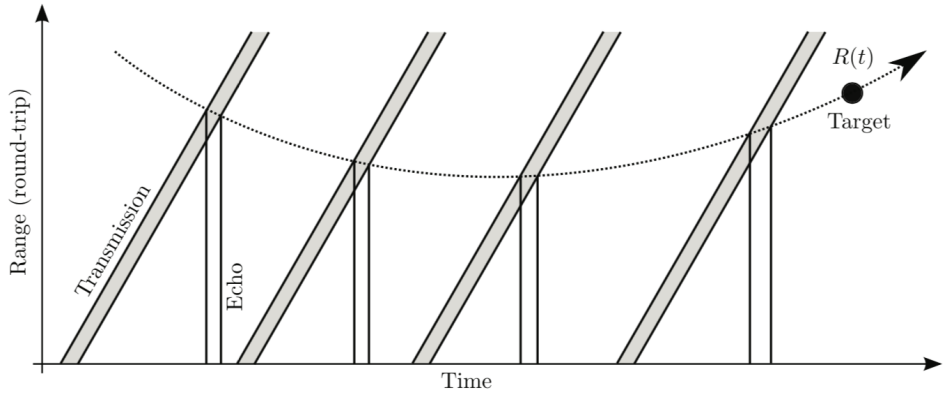

Figure 6.1: A range time diagram of the transmission and receiving of the radar measurements showing the targets radial velocity, R(t). [Figure credit Juha Vierinen [40]].

The object is flying through the radar beam, each point in the beam gives the Doppler velocity which gives the target's inclination and the time of day gives the longitude of the ascension node. The continuous time radar echo m(t) for the trajectory of a point-like target [40]:

$$m(t) = f(t) + \xi(t) \tag{6.1}$$

where the $m(t)$ is the radar echo equal with the reflected signal $f(t)$ and the radar receiver noise $\xi(t)$.

6.2 Range

Range is measured by correlating an acceleration (phase chirp), velocity (Doppler) and range shifted (time delay) transmitted pulse with the echo. This filter has the largest power for the range, velocity and acceleration that corresponds to the target trajectory. The range, R, of the signal is the round trip delay for the pulse to reach the target and back again:

$$R = \frac{c \cdot \Delta t}{2} \tag{6.2}$$

where Δt is the time delay of the signal, and c is the speed of light (approx. c= 300 000 km/s).

6.2.1 Relation between Range and Apogee

In the simulation the ECEF[1] follows the earth rotation, with its origin at the center of the earth. By doing so, it is important including the earth's radius (R_e=6371 km) when estimating the range of the observation. By assuming the eccentricity is zero (e=0) the perigee can be neglected, leaving with only the apogee. The apogee, a is:

$$a = R_e + R \tag{6.3}$$

where R_e is the radius of earth, and R is the Range to the target in the beam.

6.3 Doppler Velocity

Radar uses range and range rate to determine the orbit of a target. The range is the distance from the radar to the targeted object, and the range rate is the targets line-of-sight (LOS) velocity during the overhead pass [6]. Choosing EISCAT radar as the frame of reference, the velocity of the space debris appear slower on the measurements than what its true velocity is. The measurements state that the velocity of the majority of the space debris travels at a speed of -3 km/s to +3 km/s towards or away from the radar, respectively. This means it moves parallel to the radar, while for 0 km/s it moves perpendicular to the radar. Changing the frame of reference to the space debris, its velocity is thus 7 - 10 km/s or even higher. By assuming the space debris has a circular orbit (e = 0), the space debris' true velocity can be found by the centripetal acceleration:

$$v = \sqrt{\frac{G \cdot M_e}{R_e + r}} \tag{6.4}$$

where the G is the gravitational constant $G = 6.67408 \times 10^{-11} m^3 kg^{-1} s^{-2}$, M_e is the mass of the earth $M_e = 5.972 \times 10^{24} kg$, R_e is the earth's radius R_e=6371km and r is the range of each of the detection done by the BPE. The Doppler velocity can be found by assuming if the inclination of the detected object is known, and by assuming the object moves in an uniform circular motion it can be found by.

$$v_r = v \cdot cos(i) \cdot cos(\alpha) \tag{6.5}$$

where v is the true velocity of the object, i is the inclination, and α is the elevation angle of the antenna.

[1] earth Centered earth Fixed

6.4 Doppler Inclination

The Doppler velocity can indicate the inclination of the space debris flying through the beam, and by having found the space debris' true velocity the inclination, i, by assuming zero eccentricity (e = 0) can be found by the angle between the targets true velocity and its radial velocity:

$$i = \sin^{-1}\left(\frac{v_r}{v \cdot \cos\alpha}\right) \tag{6.6}$$

where i is the inclination, v is the targets true velocity, and v_r is the radial velocity. It is worth mention that some meteoroids travels much faster with velocity ranging from 30-60 km/s depending if they moving with or towards the earth on its path around the sun [2, 43].

6.5 Modulation and Coding

Radars transmit a pulse of electromagnetic energy and the returned signal (echo) is analyzed to give the parameters of the target. But, without modulating the signal before transmitting, it is just an EM wave with no information on it. In order to distinguish the signal from any other incoming signals it goes through the modulator of antenna hardware system. Here it will be modulated when transmitting, and demodulates again at receive. There are three characteristics of signals that are modulated. That is, the amplitude, the frequency and/or the phase. However, to distinguish each pulses transmitted, which can be several thousands pulses for each measurements, it is important to apply a unique coding to each pulses. The modulation and coding helps to apply information on the signal and as well distinguish each transmitted pulses. In the BPE campaign there was used a phase-coded for the transmitted pulse. For some selective intervals the phase is flipped. A new observing mode called LEO (Low earth Orbit) uses alternating codes. The pulse length for the LEO experiment is 1920 microseconds (ms). With a long pulse length it allows high pulse compression, including individual pulses. The code group is a strong 64 bit alternating code, with 30 microsecond bit length, and there are 128 different phase codes group. The interpulse period (IPP) is set for 20 ms per pulse which provides a 3000 km range window, before the next pulse is transmitted [6, 24].

6.6 Matched Filtering

A measured target has radial trajectory parameters. To estimate the received signal with the corresponding shape vectors such as the range, velocity, and acceleration. These shape vectors is found when finding the maximum likelihood by the a Generalized Matched Filter (GMF)[2], the end result is the error corrected parameters, and its most likelihood estimates.

The method on how to detect space debris while "piggy-backing" an incoherent scattering measurement is carefully described by Markkanen in [24]. By doing so, makes the beampark measurement of space debris a low cost experiment. He describe how they uses a separate receiver parallel with EISCATs own receiver to not interfere with the ionospheric measurements and how they obtained a significant faster model by using faster computers.

To detect a target, a modulated coded signal is transmitted into space hitting a target with sufficient radar cross section that scatters sufficient energy back for the radar to detect it, called the radar echo. If it exceed the detection threshold based on estimated signal energy $W_{\hat{s}}$ the target

[2]The EISCAT UHF radar uses a similar filter FMF which gives almost the same results

gets detected. The detection threshold is set by visual inspection of data to be high enough to get sufficient echo measurement of the target to prevent false alarms [24].

The requested parameters to determine the target is the range, **R**, the radial velocity, v_r, the radial acceleration a_r and the signal energy, W_s. All these parameters are found in the measured signal, and by finding the maximum GMF:

$$\widehat{SNR}_N \equiv \frac{\widehat{W_s}}{kT_{sys}} \approx max_{R,v_r,\alpha}\frac{GMF^2}{\sigma^2} \tag{6.7}$$

$$\Longleftrightarrow\sqrt{\widehat{SNR}_N} = max_{R,v_r,\alpha}\frac{GMF}{\sigma} > Threshold \tag{6.8}$$

meaning that the sensitivity of the radar depends on the transmitted signal. Matched filtering is used when making the beampark measurement, however it is not used in the simulations. Here it is used a theoretical SNR, with calculations that are consistent with the ones used in the BPE [40].

Chapter 7

Beampark Experiment 2018

A beampark experiment (BPE) is presented in this chapter, and how it is performed, what it obtains and what parameters may be extracted from it.

7.1 Introduction

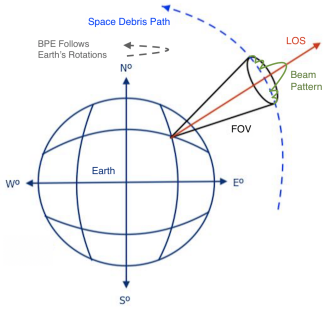

Figure 7.1: Concept of the beampark experiment.

As a part of this master thesis a beampark experiment (BPE) was performed on the 4th of January 2018 simultaneously at EISCAT Svalbard (32m) and EISCAT Tromsø (UHF). Each radars are located at different latitudes and longitudes pointing east at a fixed point at a azimuth angle of 90° and with an elevation of 75° (see figure 7.2). Figure (7.1) shows the concept of the BPE. Here the beam sweeps through the polar regions for 24-hours following the earth's rotation. EISCAT UHF has a beam with a field-of-view (FOV) of 0.7°. The line-of-sight (LOS) is marked with a red line and is the center of the beam, where the beam pattern is illustrated in green. The dashed blue line shows the space debris path, however, this is just an example orbit, the space debris may enter the beam from any angle.

The data which the BPE collects is the parameters such as the Doppler inclination, range, RCS and the Doppler velocity of the space debris. Another part of this thesis is to perform a simulation of the space debris environment and to estimate the density function of the space debris of EISCAT UHF may detect through the beam as a function of possibility of detecting the space debris with EISCAT beam. The simulation will be simulate a BPE and will be explained more in the next chapter (8). Here the observations by the beampark experiment campaign will be compared with the simulation.

Figure (7.2) shows the radar beam of EISCAT UHF at Svalbard (Red) and Tromsø (yellow) both with a range of 2500 km at scale. Svalbard has a FOV of 1°, whereas Tromsø has a FOV of 0.7°. The space debris orbits in a Keplerian orbit as a satellite would, and its position is found by the six classical orbital elements: $\mathbf{x} = [e, a, i, \Omega, \omega, \nu]^T$ [3].

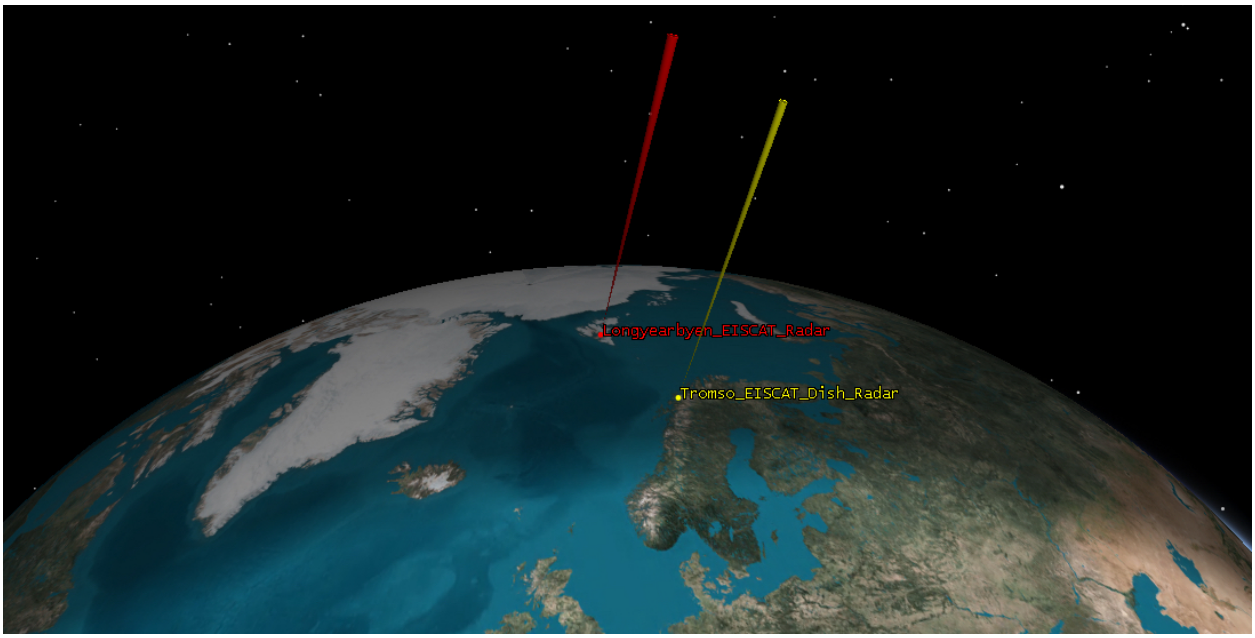

Figure 7.2: An illustration of the beampark experiment. EISCAT radar at Longyearbyen has a FOV of 1°, wheras Tromsø has a FOV of 0.7°. [2]. Made in STK [4].

7.2 Beampark Experiment 2018

The data is presented in table (7.1) giving all the parameters extracted from the experiment which where used for plotting the output.

Table 7.1: The parameters extracted from the BPE data done at 4th of January to 5th of January 2018 at Tromsø and at Svalbard

Parameters	UHF Tromsø	UHF Svalbard
Date	04/04/18 - 05/04/18	04/04/18 - 05/04/18
Start time	12:00:00	12:00:00
Duration (hour)	24	24
Duration (sec)	86 400	86 400
Integration time (sec)	0.1	0.1
Number of Detections	1744	1815
Transmit Power (MW)	1.55 - 1.69	0.60 - 0.70
System Temp. (K)	90.0 - 95.0	110.0 - 120.0
Azimuth (deg)	90	90
Elevation (deg)	75	75
Coherent - Integration ($\sqrt{SNR}$)	5 - 10 000	5 - 10 000
Range (km)	200 - 2500	200 - 2500
Doppler Velocity (km/s)	- 9 to + 9	- 9 to + 9
Doppler Acceleration (km/s^2)	0 - 200	0 - 200
Event Duration (s)	0 - 25	0 - 25

7.3 Plots

7.3.1 Range

The figure 7.3 shows the number of detection per 25 km bin between Tromsø and Svalbard. The detections correlate very well, but differ at various peaks, this may be the different latitude the radars is located at, or their different transmit frequencies. At Svalbard, satellites with inclination between 78° and 102° are detected wheras Tromsø detects satellites with inclination between 68° and 112° making the Tromsø radar detect more satellites in between 68° and 78° and 102° and 112°.

The histogram shows the number of detection for each 100 km in LEO done by EISCAT UHF radar in Tromsø. There are several peaks that indicates the most dense orbits. These are approx. at 600, 800, 1100, and 1500 km. At 600 and 800 km is where the two most severe break up events happened, the Iridium-Cosmos and the Fengyun-1c. These happened in 2007 and 2009, which is now over ten years ago, and still these orbits are dense with space debris. This states the fact that it takes a long time for these altitudes to de-orbit.

1100 and 1500 km are popular orbits for weather- and surveillance satellite, there has not been any known break up events in these orbits. There are yet not that dense in the 1100-1500 region, here it is planned to launch 12 000 satellites by SpaceX, OneWeb and Samsung. However, in the next plots there is shown a cluster indicating a recent break-up event exactly in these regions.

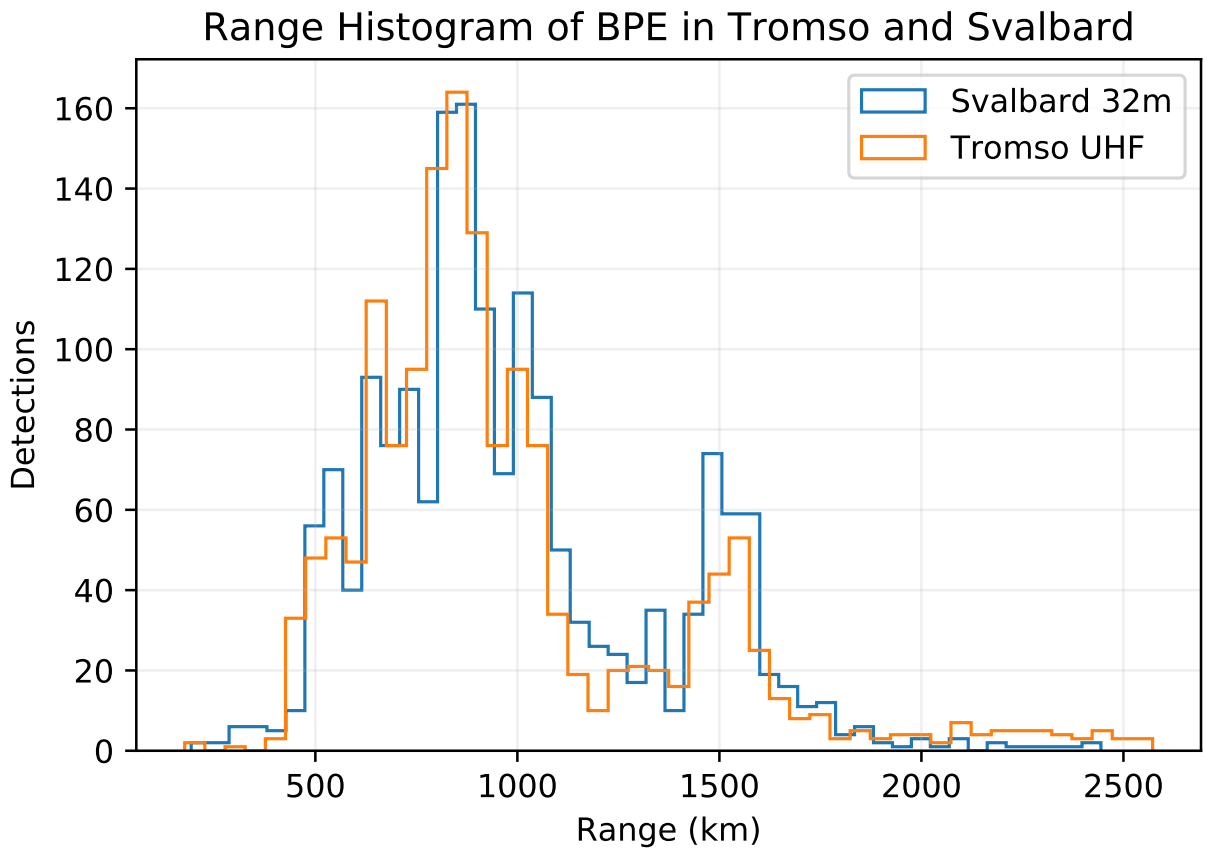

Figure 7.3: Number of detections per 100 km during the BPE in Svalbard and Tromsø.

Range vs Time

The BPE lasted for 24 hours (86 400 seconds). The figure (7.4) shows all the detections for total range and timespan during the BPE. The colors indicates the Doppler velocity of the target.

It is seen in the scatter plot at 1350 km at both 40 000 seconds and 80 000 seconds a cluster in green which indicates that there has been recently a break up event. It is not known yet what this has been, indicating it may have been either an inactive satellite colliding with a unknown space debris object, or a fragment breaking up due to anomalous events. Same is barely seen at 500 km at 40 000 seconds and 80 000 seconds. By finding its orbital elements it is feasible to track its origin, and what it could have been.

It can be discussed if there is even more in the scatter plot, however the mentioned cluster is the one most visible in the plot with its distinctive cluster signature. Moreover, the density in figure (7.4b) is largest at 800 km during the entire event. However, the histogram in figure (7.6c) shows the number of detections per 30 minutes with peaks at 15 000 seconds, 40 000 sec., 60 000 sec, 80 000 sec, where the latter one, peaks highest of them all, which is usual for a break-up event.

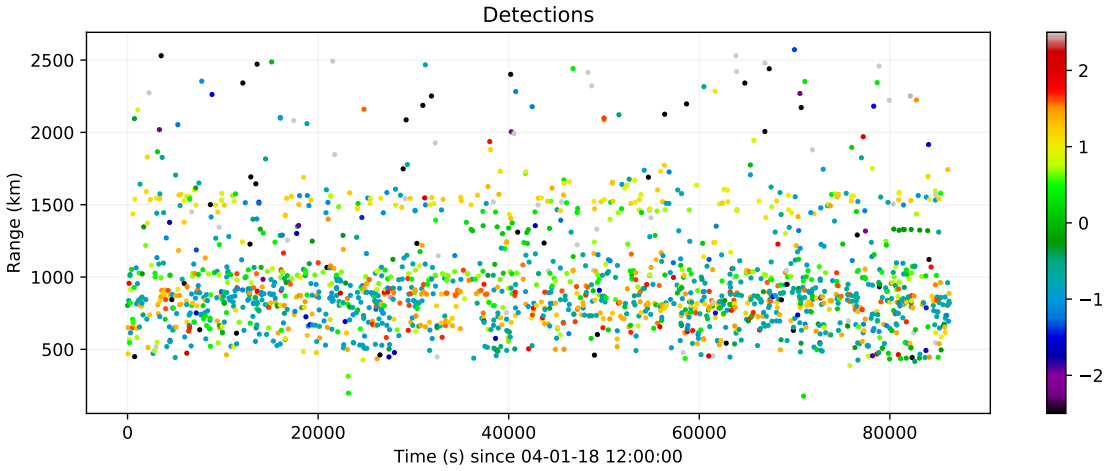

(a)

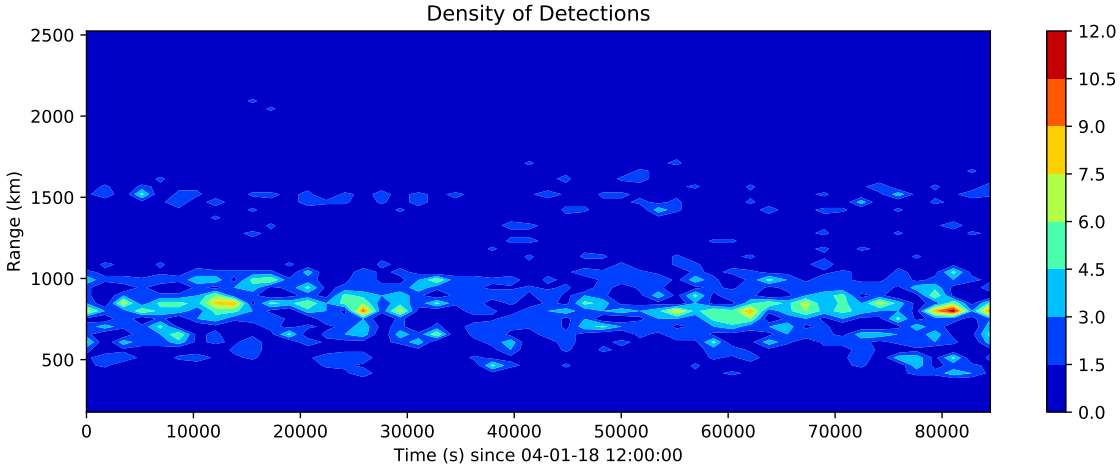

(b)

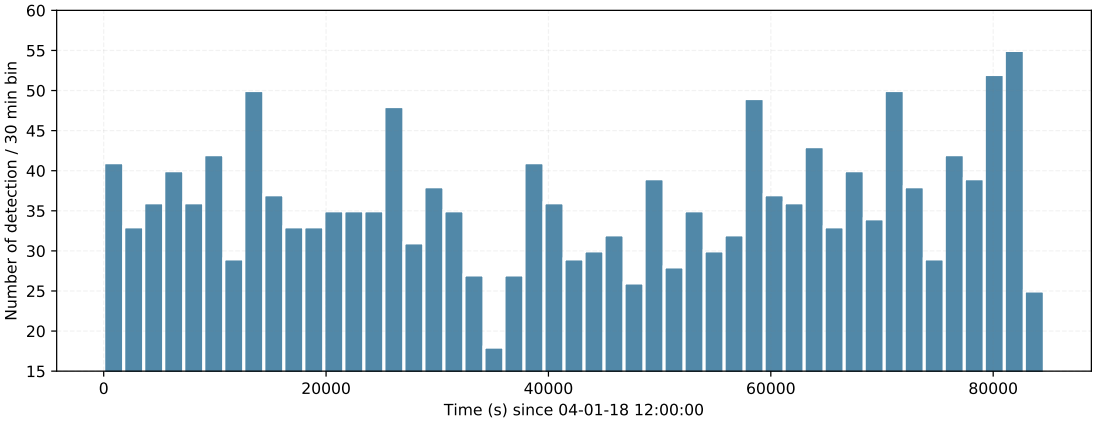

(c)

Figure 7.4: Range vs. Time

7.3.2 Doppler

Doppler vs Range

The Doppler velocity comes from when the target hits the beam and several pulses measures the difference of time in the beam. The measured Doppler velocity, v_d is the radial velocity, $R(t)$ of the object. For EISCAT this is called point-like target radar measurement. The scatter plot in figure (7.5a) shows the detections for each km from 200 to 2500 km, and its corresponding Doppler velocities. When the target moves towards the radar the velocity is negative (blue), and it is positive (red) when the target moves away from the radar, the target is zero (green) when it moves perpendicular to the radar.

Figure (7.5b) shows that the most dense regions is at 800-900 km this distribution is almost symmetrical for objects that moves towards and away from the radar with a peak velocity of $-0.82km/s$ and $+1.19\ km/s$ and a mean velocity of $1.04\ km/s$ on the negative side, and $1.11km/s$ on the positive side with 827 detections on the negative side and 913 detections on the positive side. However, the space debris moves much faster in the lowest altitudes, with higher accelerations, which is something what are seen in the acceleration plots, this is not included in this thesis.

The dashed gray lines shows the radial velocity when the signal is on maximum strength for targets in circular orbits at an elevation steered at 75°.

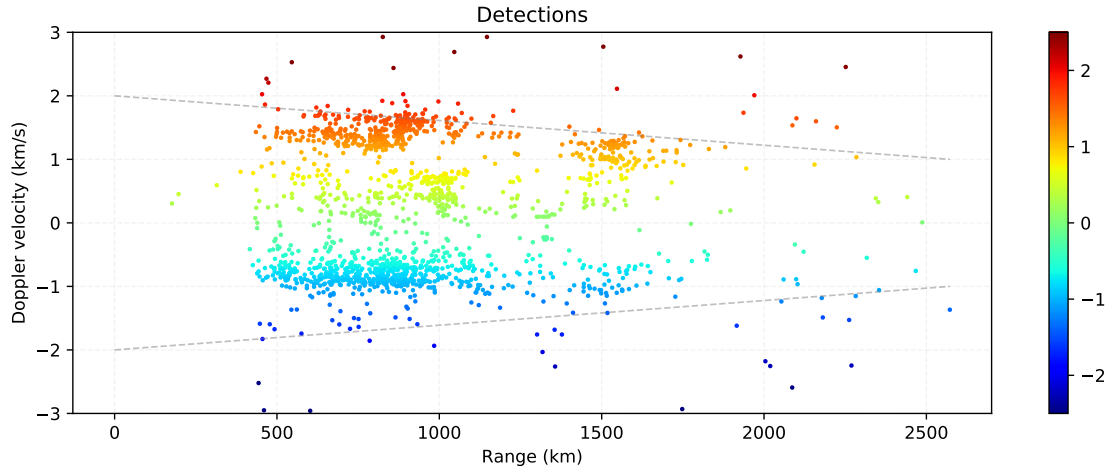

(a)

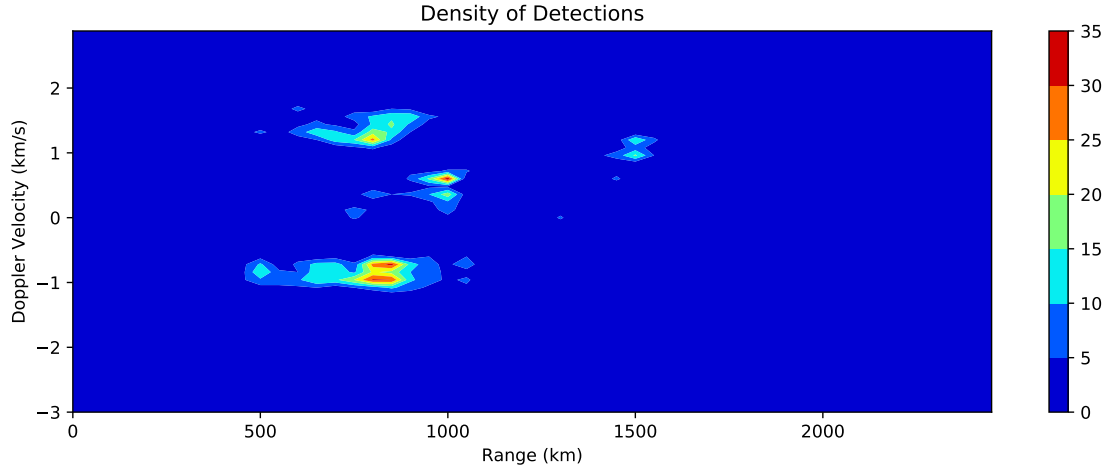

(b)

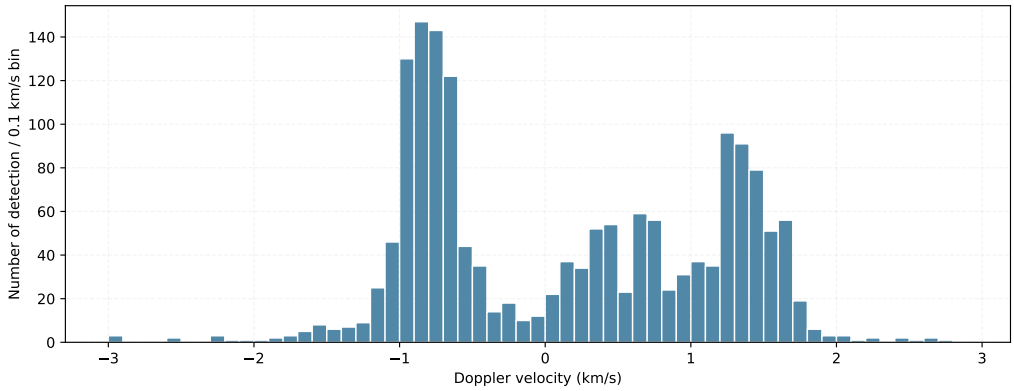

(c)

Figure 7.5: Doppler Velocity vs. Range

Doppler vs Time

The figure 7.6 shows the number of detections measured during the time that BPE occurred and their Doppler velocity. Also in figure (7.6a) it is seen a distinctive cluster at the same time, at 80 000 seconds.

In the density plot in figure (7.6b) there are repetitive regions with a negative velocity of $\approx -1\ km/s$ lasting almost continuously from roughly 10 000 s ($\approx$ 15:00) until 25 000 s ($\approx$ 19:00), and the same strong density rate again at from 68 000 s ($\approx$ 7:00) to 78 000 s ($\approx$ 9:30). This means a large amount of objects orbiting with a velocity of mean -1.04 km/s each 12 hours lasting for roughly 5 hours moving towards the radar. For the positive Doppler velocity the distribution is more uniform spread throughout the entire BPE.

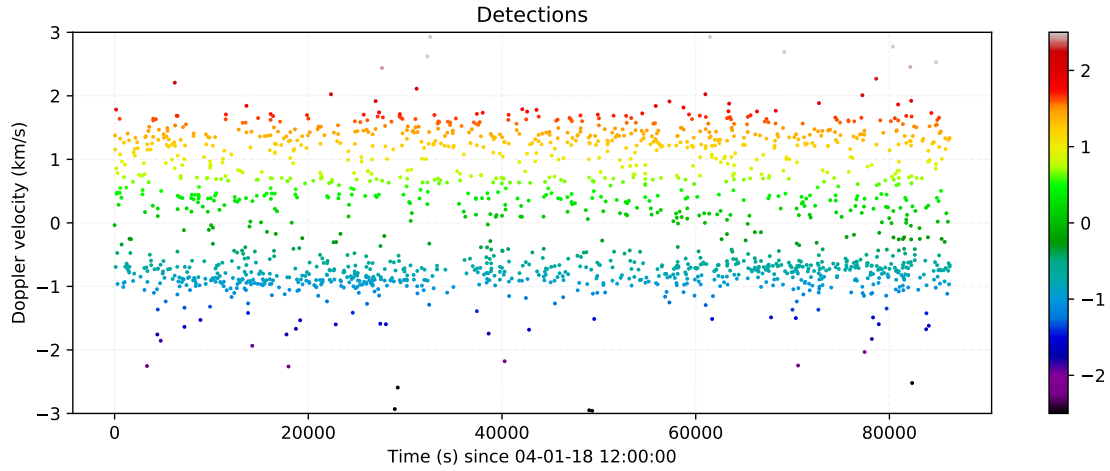

(a)

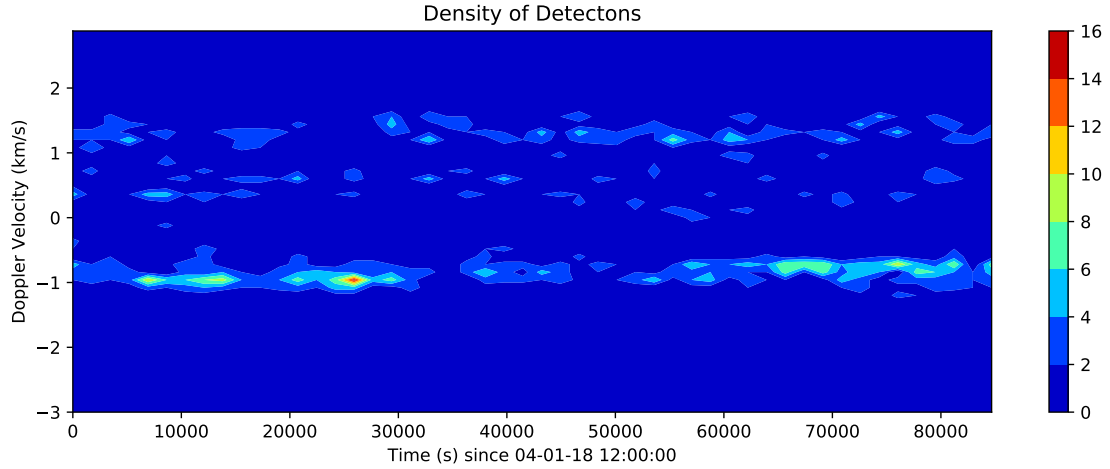

(b)

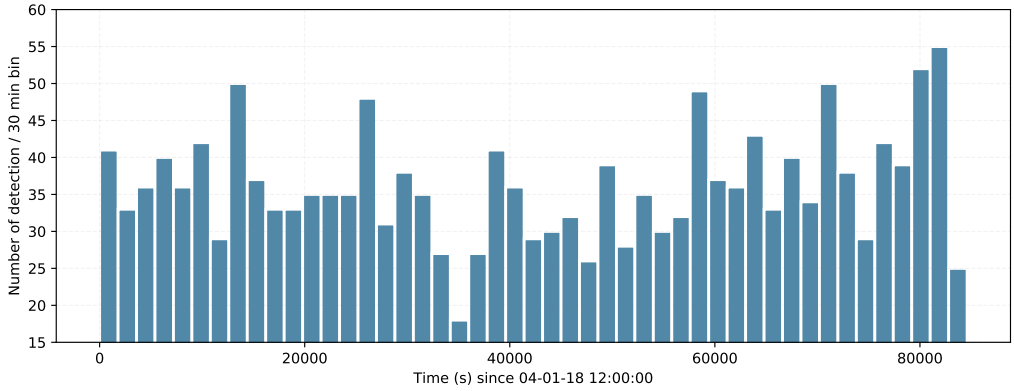

(c)

Figure 7.6: Doppler Velocity vs. Time

Doppler Inclination

By assuming that the space debris has a uniform circular motion ($\varepsilon = 0$), and by using the Doppler velocity the inclination of the targets can be found. The UHF Tromsø only detects objects which has an inclination larger than 68° and less than 128°. The number of detection can be seen in be seen in figure (7.7a) which shows large amount of detections especially in the range of 900 km and 1500 km, where the densest regions is shown in figure (7.7b) where the largest inclination is at 900 km with an inclination of $96° \pm 2°$ at a range of 800 km. This is one of the most popular region and is the sun-synchronous orbit (i = $100° \pm 5°$), a quick reminder that it is assumed here that the eccentricity is zero, which is not the case in real life, so this inclination is not accurate, but a close approximation, which is why it deviates a bit. The second most dense orbit is at $76.5° \pm 2°$ at a range of 820 km. And the third most dense orbit is at $84° \pm 3°$ at a range of 820 km. These corresponds very well as the ESA's illustration of the density of space debris in the polar regions are shown in figure (3.8). The histogram in figure (7.7c)shows the number of detections for each degree(°) from 68° to 128°.

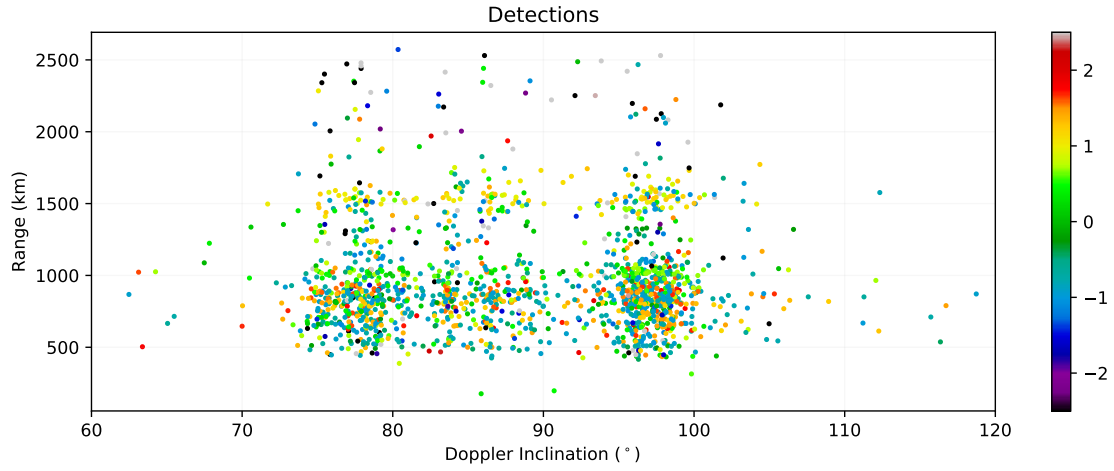

(a)

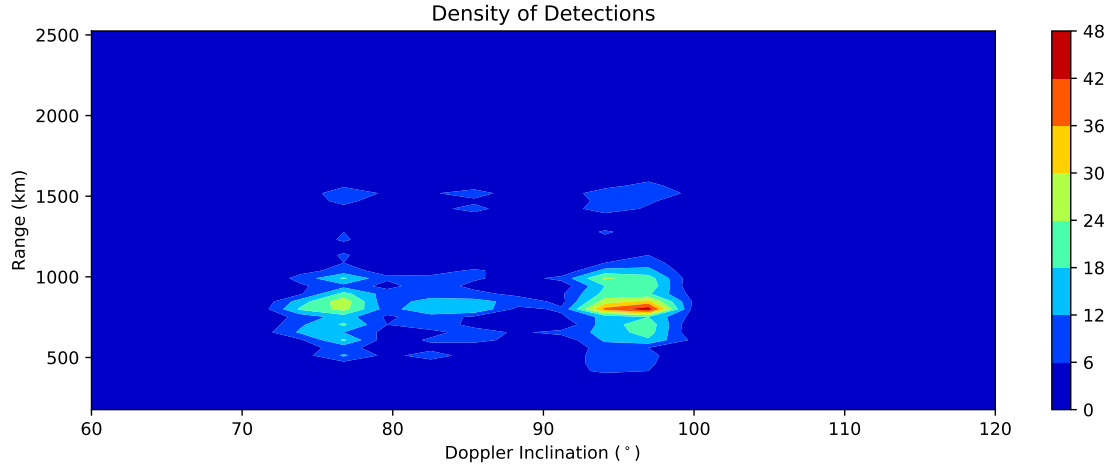

(b)

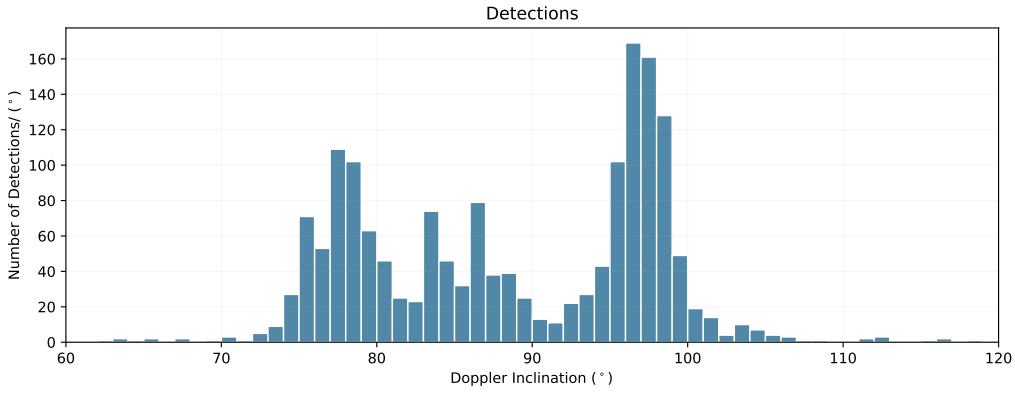

(c)

Figure 7.7: Doppler Inclination vs. Range

7.3.3 Signal-to-Noise Ratio

Over the next four pages, the plots of the SNR with respect to range, time, Doppler velocity and Doppler inclination will be presented. The descriptions of the plots will be explained first, followed by the plots.

The radar cross section (RCS) determines the amount of reflected energy from the measured target. It is not known where along the beam the object is, therefore its true size and shape is not known. A large object (e.g. a large satellite) may show low response on the spectrum at the receiver when it moves in the one of the sidelobes, and it can give large amount of instrument response on the spectrum when it hits in the middle of the main lobe. The same goes for a small object (e.g. CubeSat, space debris, small rocket parts) they may not be detected when they hit one of the sidelobes due to their small size which cannot reflecting enough amount of energy to trigger the threshold criteria. Having lower threshold than 25 gives false alarms in the detections.

SNR vs. Range

The measurements in figure (7.8) shows the SNR over the range from 200 to 2500 km. A minimum detected objects are distinctive shown at SNR = 5 dB, and up to a maximum of 80 dB. The colors in the scatter plot in figure (7.8a) is the Doppler velocity of the detections. In figure (7.8b) it is shown a high density of detections at 18 dB at a range of 800 km, corresponding rather well in shape and density with the histogram below in figure (7.8c).

SNR vs. Time

The figure (7.9) shows the number of detections done during the 24 hours BPE campaign with the corresponding SNR. The minimum threshold is 5 dB and the colors in the scatter plot (7.9a) is the Doppler Velocity. The SNR is the parameter that indicates the size of the objects that flies through the beam assumed that the objects hits the center of the beam. The mean SNR is around 18 dB which repeats in time interval through the BPE, where the densest region of the number of detection was at approx. 80 000 s. This confirms even more that there had to be measured a break-up event during the experiment. The histogram shows the number of detections per every 30 minutes for 24-hours.

SNR vs. Doppler Velocity

It is seen here in figure (7.10) that the largest density of detections happens in the velocity of $-1\ km/s$ which moves towards the radar with an SNR of 18 dB.

SNR vs. Doppler Inclination

The figure 7.11 shows which inclination with its corresponding sizes in the form of SNR. The figure (7.11a) shows the detections in the various inclinations with corresponding SNR where the colors is the doppler velocity. The two most dense regions with highest amount of detections is shown in (7.11b) of SNR = 18 is the $i = 78°$ and $i = 98°$ and at the latter one the highest distributions reaches to above 50 dB which might indicate that this inclination has the largest sizes flying through the beam. Which is somewhat true, since here orbits most of the satellites in the sun-synchronous orbit, and requires large solar panels to perform their measurements. The figure (7.11c) shows the number of detections per inclination degree (°), and that the inclination of $i = 98°$ also has the highest amount of detections.

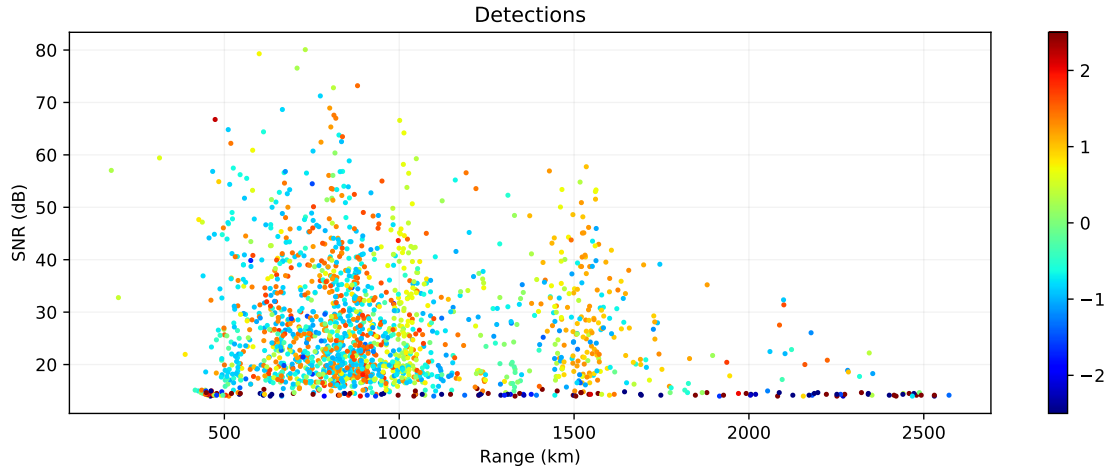

(a)

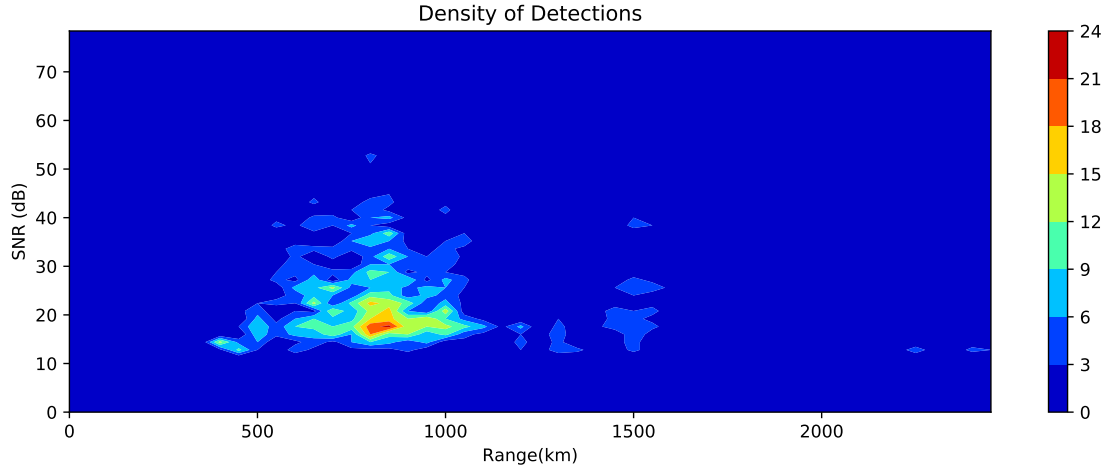

(b)

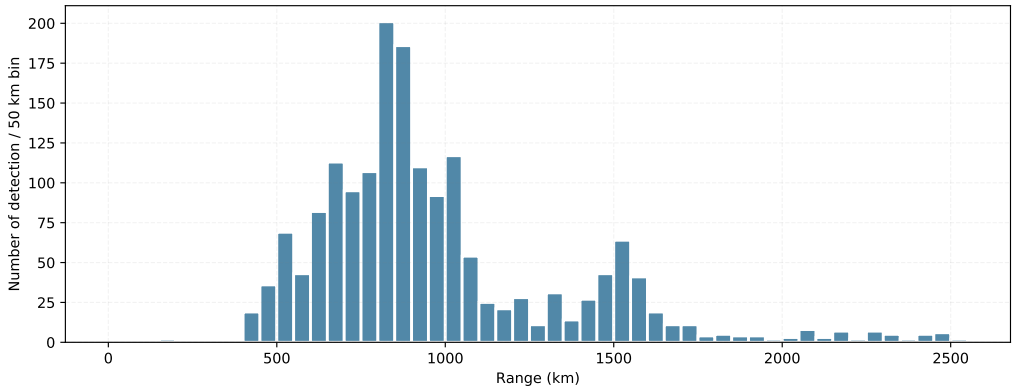

(c)

Figure 7.8: Range vs. SNR

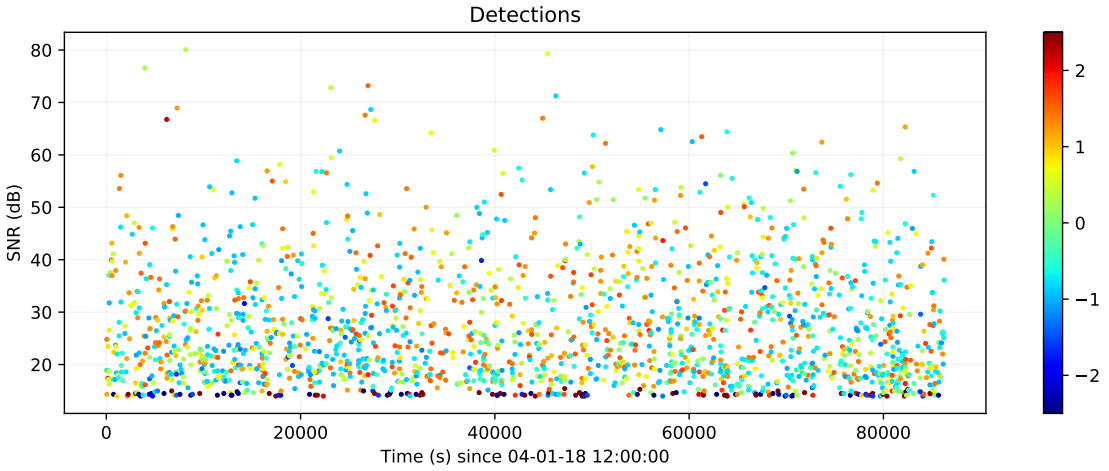

(a)

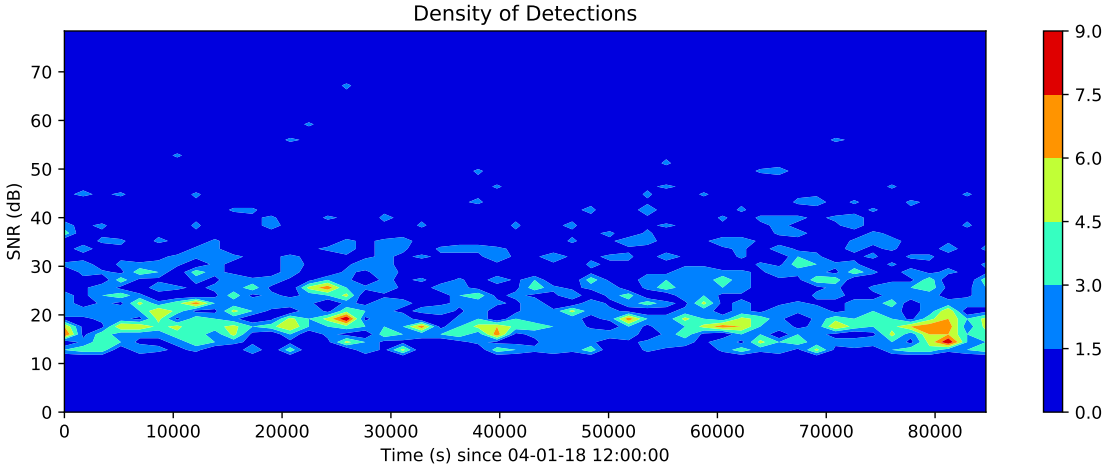

(b)

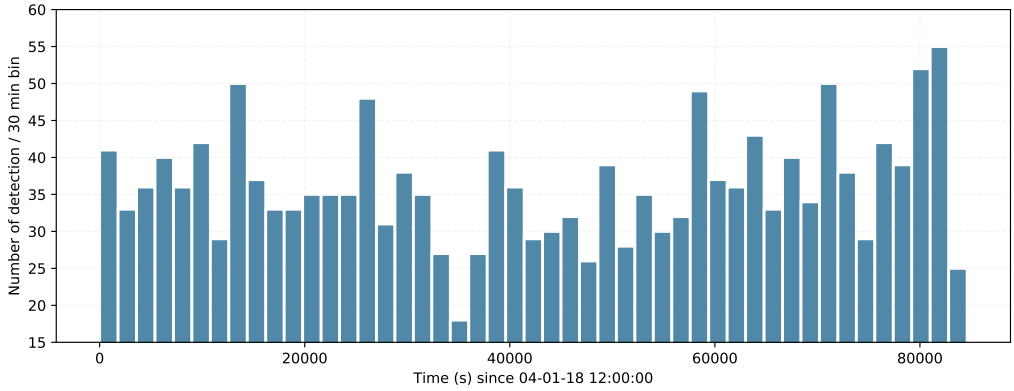

(c)

Figure 7.9: Time vs. SNR

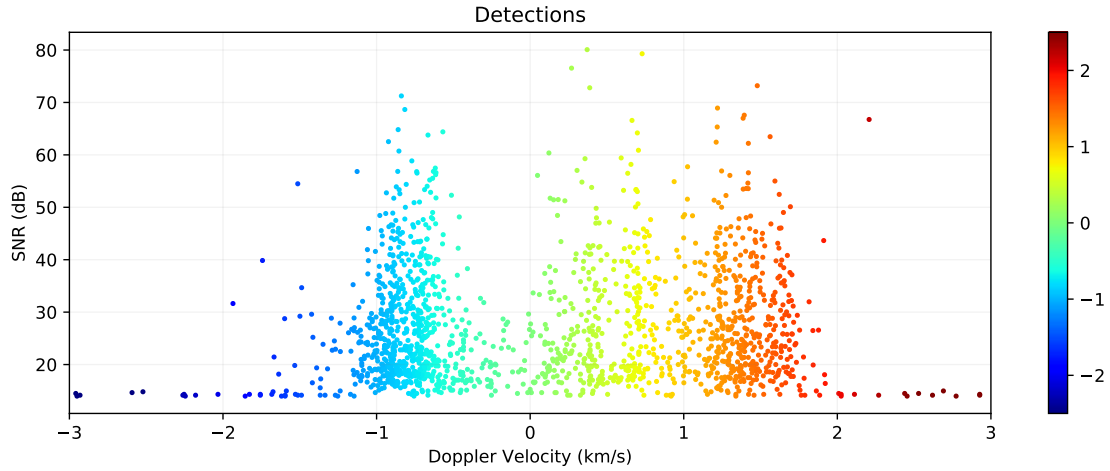

(a)

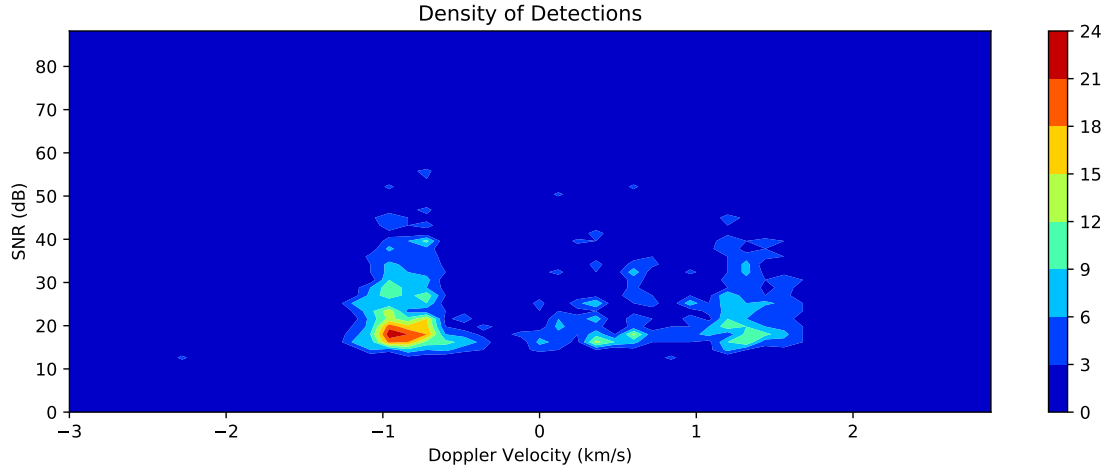

(b)

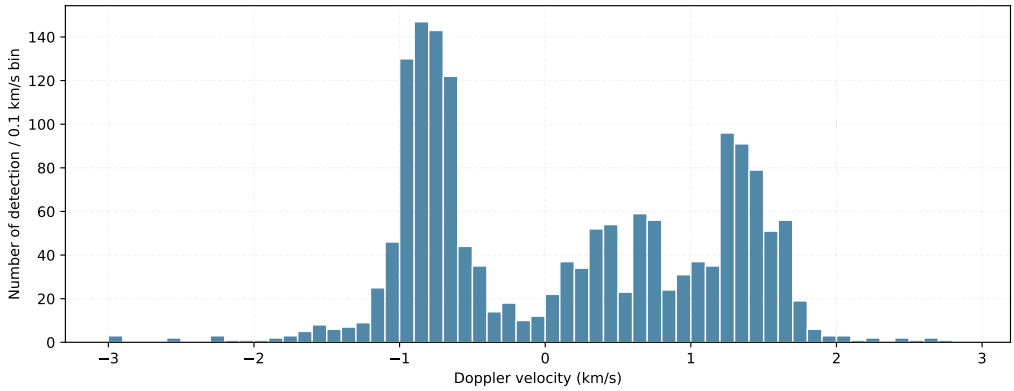

(c)

Figure 7.10: Doppler Velocity vs. SNR

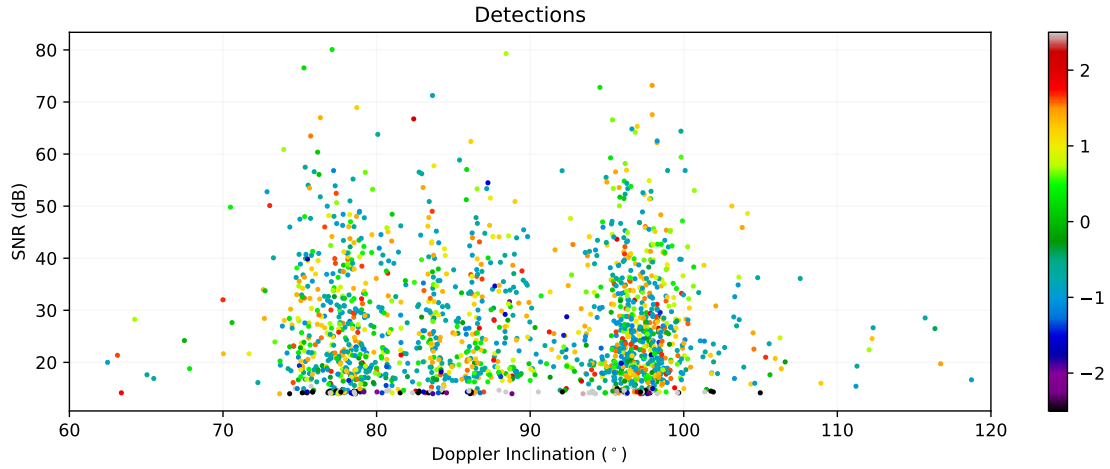

(a)

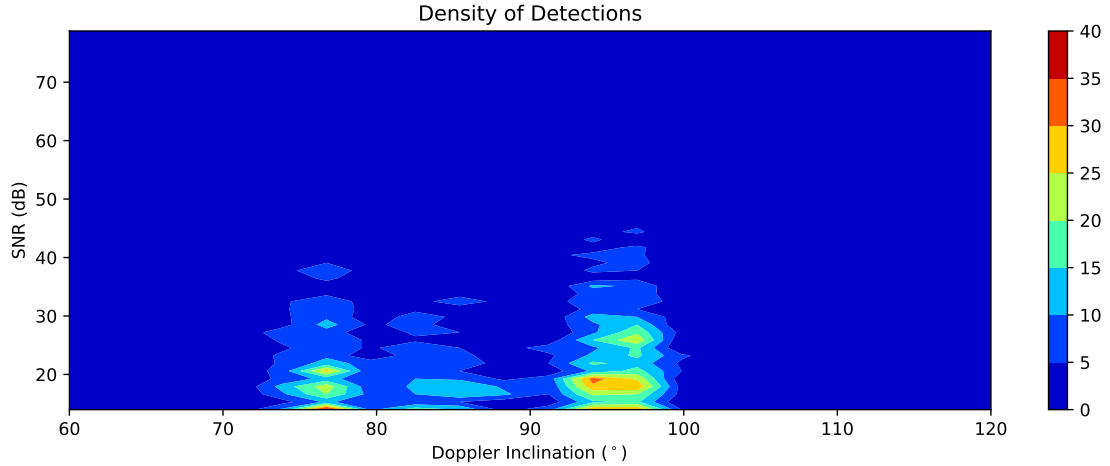

(b)

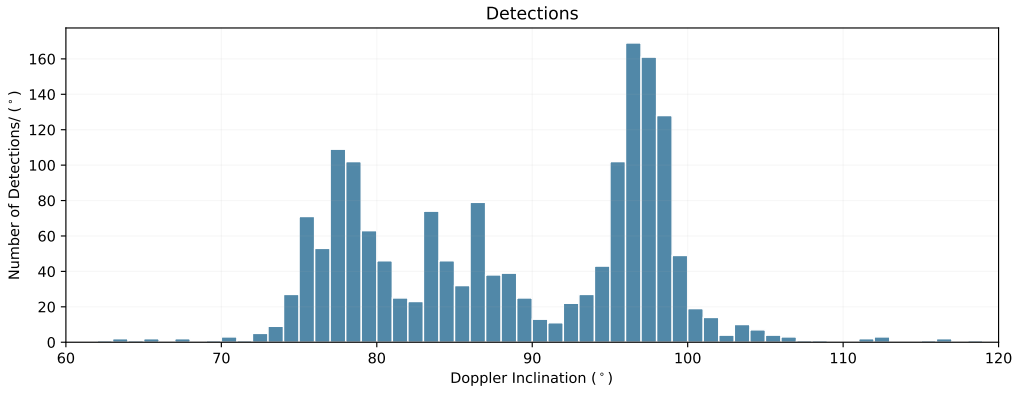

(c)

Figure 7.11: Doppler Inclination vs. SNR

7.4 Summary

In the beampark experiment (BPE) it was found what is believed to be a recent break-up event. This is seen roughly at the time of 80 0000 seconds, which are roughly at 22:00:00 UT, at an altitude of 1350 km. By finding its orbital elements, it is feasible to find out what this could be, and trace it back to its origin, especially so soon after its break-up. However, there is not stated any recent break-up events in any catalogs yet.

It is seen in the comparison between Svalbard and Tromsø a good correlation in the detection. A slight deviation in some of the altitudes, which could be due to the different transmitted frequencies, or their different location. Nevertheless, both showed peaks in the range of 800 km and 1500 km.

The Doppler inclination stated that there was more space debris in the regions with inclination of 78° and 98°, which corresponds to the Doppler velocities of roughly $-1km/s$ and 1 km/s, respectively.

Chapter 8

Modelling EISCAT Observations of Space Debris

This chapter contains the modelling of EISCAT beampark experiment. It will go through the process on how the modelling was obtained. It will start by explaining the process on how to simulate a beampark experiment and which sizes are detected with its respective apogee and inclination.

8.1 Introduction

In order to estimate and simulate the beampark experiment, some assumption had to be made. Since the BPE only lasted for 24 hours, alot of perturbations that space debris normally would experience can be neglected. The first one is to neglect atmospheric drag, which affects objects orbiting below 1000 km, second the earth gravity harmonics is neglected, since it is assumed that earth is a perfect sphere. Also, the third-body perturbation gravitational effect is neglected, here the Sun and the Moon affects the objects in orbit. Also, no solar radiation is considered, which may push the orbital objects further down in altitude, and at last it is assumed that the space debris moves in a uniform circular orbit. All of these perturbation could be included if the experiment lasted for over a longer period of time, which is something satellites in orbit take into considerations. All these simplifications had to be made in order to make faster multiple runs of the simulation.

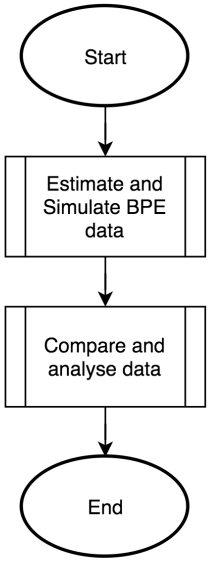

Figure 8.1: The process of the BPE and the simulation.

8.2 Number of Detections per day

The process of how the estimation and simulation of the BPE data is done are described through the flowchart in figure (8.2). It shows in order to obtain the probability of detection $p(a, i, d)$, a simulation of the BPE experiment needs to be done, parallel with the sorted ESA MASTER catalog.

Starting with the simulation. It uses the radar parameters as stated in the table (8.1). The elevation was set to be 75° and azimuth pointed towards east at 90°. The transmit power was calculated by the radar-equation (5.1) and with a gain pattern corresponding to a uniformly illuminated circular aperture of a dish with 16 meter radius.

Table 8.1: Radar parameters used in the simulation.

Parameters	Values
Peak Power, P_t	1.5 MW
Coherent Integration time (CIT)	1 ms
Transmitt Pulses/CIT	5
Noise Bandwidth	200 Hz
Receiver Noise Temperature, T_r	100 K
Gain, G (On-axis)	48 dB
Radius of Circular Aperture	16 m

With these parameters the modelling was done by using a Monte-Carlo method, which is used to collect statistics on multiple runs in the simulation. It propagates a large number ($N_s = 1000$) of objects for 24 hours. The simulation records the maximum antenna gain, G_p for each pass of an object and where the object crosses the beam in a certain timestep. Then it finally records the parameters that describe each pass. Then it models through all the apogee following by all the inclinations, where each number of object has the same apogee and inclination, but the has a different random mean anomaly. This is then stored in a database which now contains the simulated observations. Then the calculated SNR for each pass is obtained by using the recorded antenna gains. By selecting only the objects which exceeds the threshold of 25 results in knowing how many objects, N_d, would be detected.

The radar cross section was programmed in a way that objects had to reflect enough amount of energy per unit square area for the instrument response at the receiver to exceed the threshold while flying through the beam. In other words, the signal to noise ratio at receive had be more than 25 in order for the object to be detected. This threshold has been set after many test campaigns which confirmed threshold, and is the same as the one used during the BPE 2018 campaign. A special case for the BPE at EISCAT is with that the threshold ($\sigma = 5.6$) it is assumed that the number of false detections and missed detections is closed to zero [24]. This will be studied further in chapter (9).

The number of detections is then divided by the number of samples, N_s done in the simulation, which results in the number of detection per day, which then by a grid search of apogees, inclination and diameters and by averaging for all diameters resulted in an estimate of the average number of detections per day, $N(a, i, d)$. Where the inclination grid was set to be 0.5° and an apogee grid of 10 km.

The results of the output are in the two following section (8.2.1) and (8.2.2). Here it is described as the number of detection per day, $N(a, i, d)$, first for small objects, then followed by large objects.

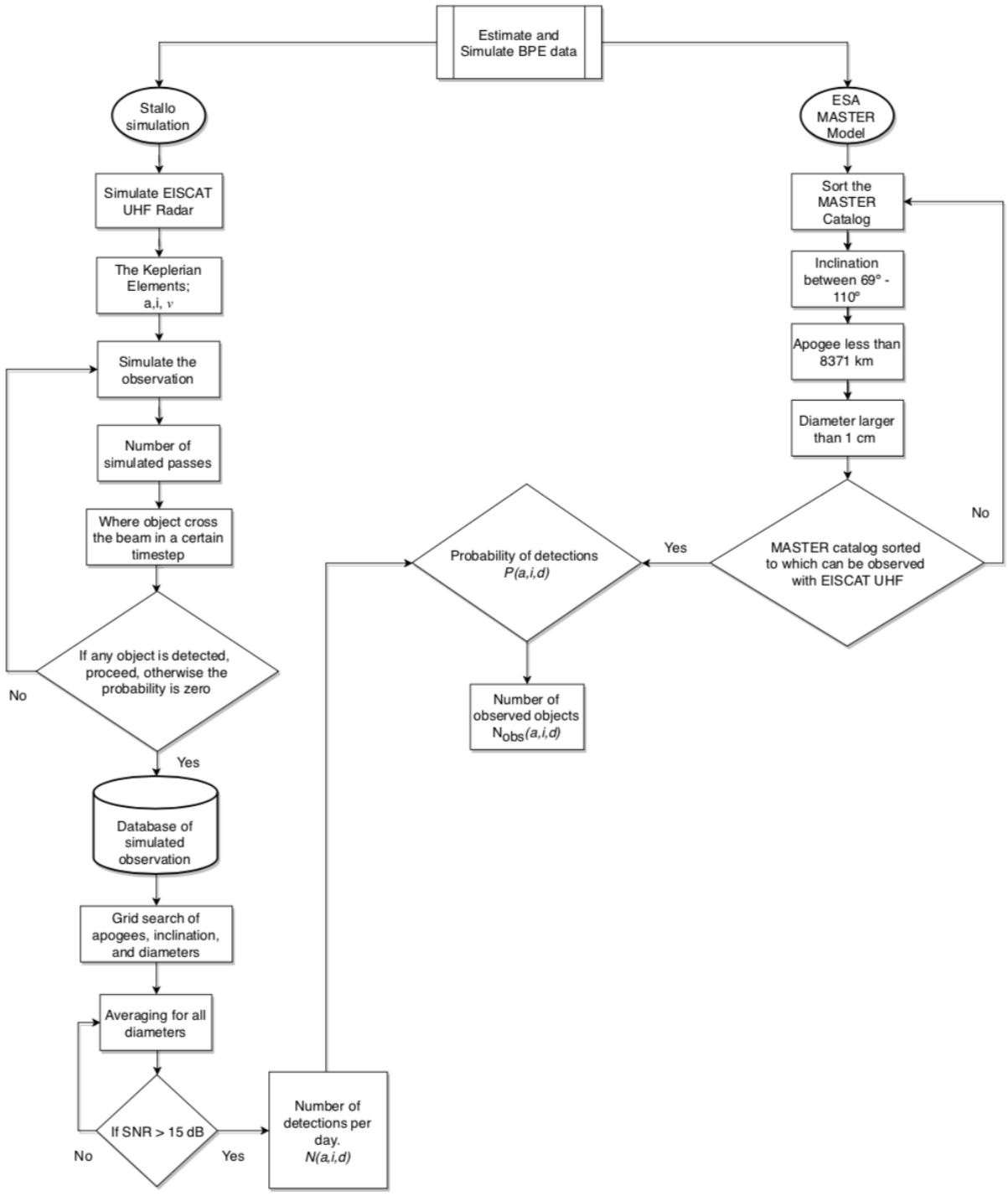

Figure 8.2: Flowchart on how the estimation and simulaton of the BPE data was processed in order to use the ESA MASTER Model to get the probability of detections. This resulted in the output of number of observed objects.

8.2.1 Small Sized Objects

The smallest objects below 10 cm are not trackable with SSN. The figure (8.3) shows the smallest objects which only the HPLA radars may detect, from 1 cm to 10 cm. The colorbar is the number of detections per day. For objects at 1 cm, this is nearly not detected, only the 300 km in range. However, it is seen here for the smallest diameter the probability of detection in range increases proportional as the diameter of the object increases. The increase happens at an inclination of 70° and 110°. These objects moves rather close to the latitude of EISCAT, presumably due to objects are spending more time moving parallel to the radar, than for polar orbits around 90° which moves perpendicular. So, the number of detections per day is strongly a function of inclination. Objects above 5 cm are, however, observable at the entire range.

8.2.2 Large Sized Objects

As the size increases the probability of detections per day increases. In figure (8.4) objects above 20 cm and up to 100 m is shown. Still the strongest detections are at the inclinations of 70° and 110°. For these sizes the probability is rather high, and significantly more detections can be made. This we can observe the object in the sidelobes of the antenna beam pattern, which is not possible for objects around 2 cm.

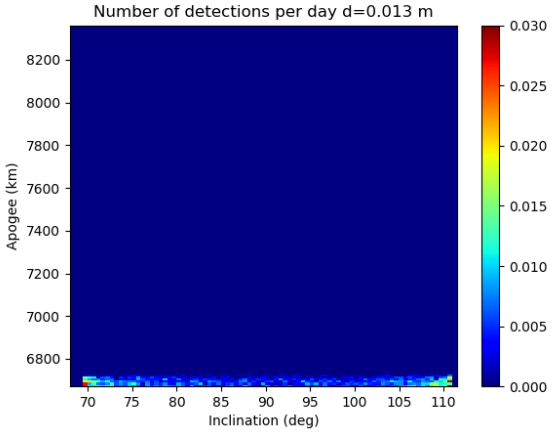

(a) 1.30 cm

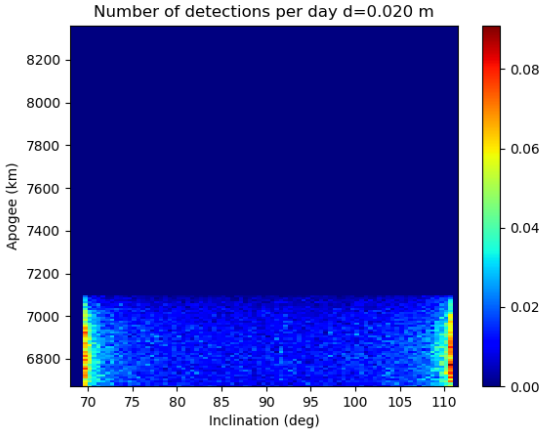

(b) 2.00 cm

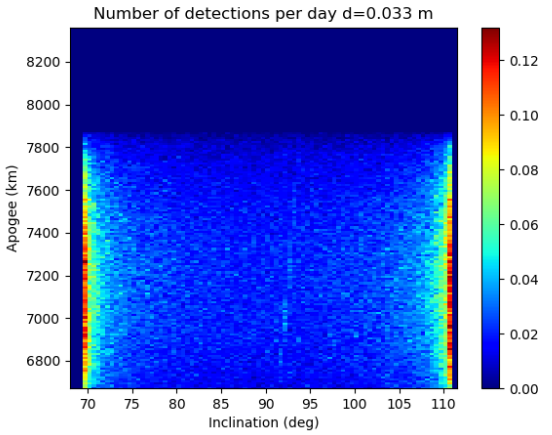

(c) 3.30 cm

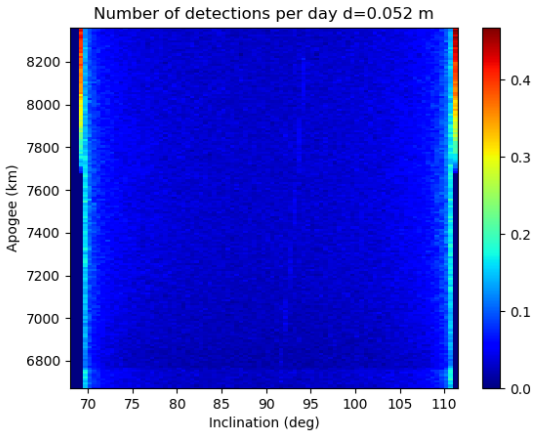

(d) 5.20 cm

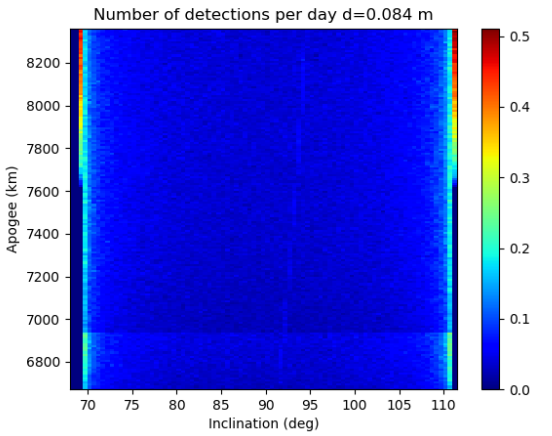

(e) 8.40 cm

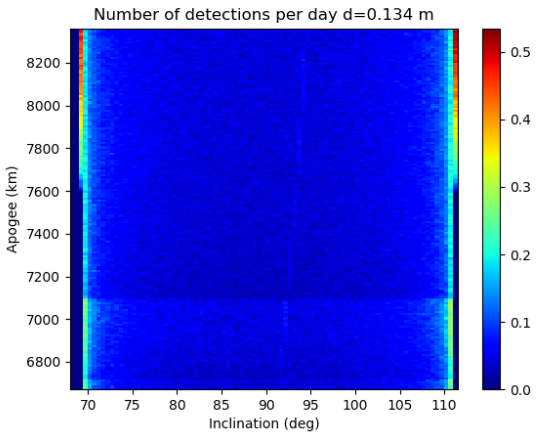

(f) 13.40 cm

Figure 8.3: Objects with diameters from 1 cm to 13 cm.The colors indicates the probability of detections per day for a diameters from 1.30 cm to 10 cm. Number of detections per day, as a function of apogee and inclination, for a 2 cm diameter object.

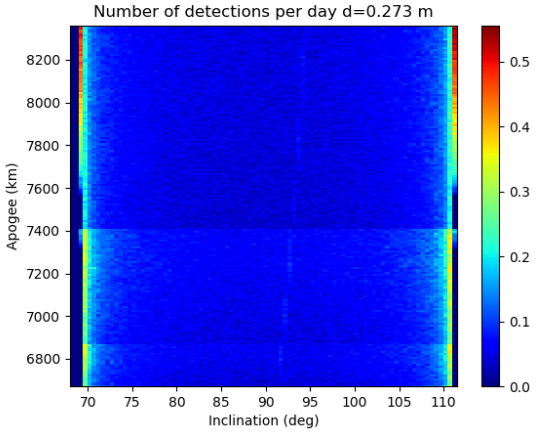

(a) d = 0.27 m

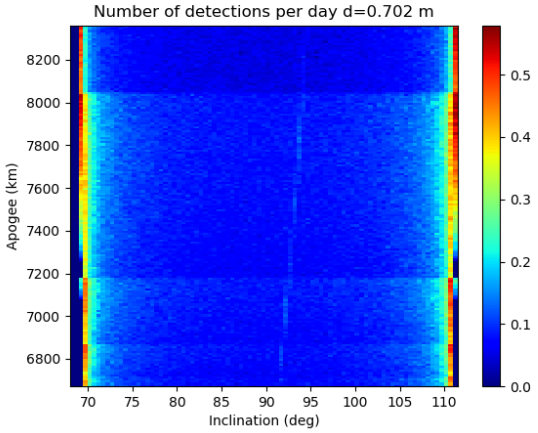

(b) d = 0.70 cm

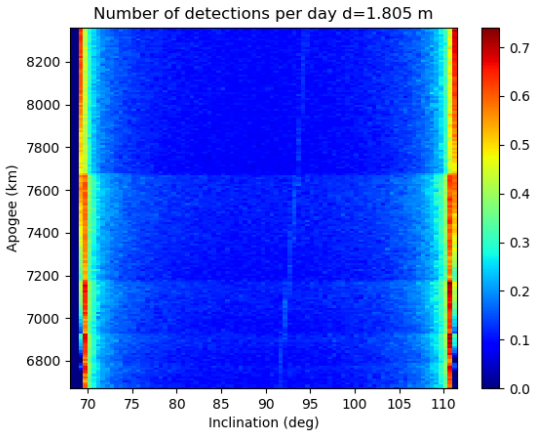

(c) d = 1.80 m

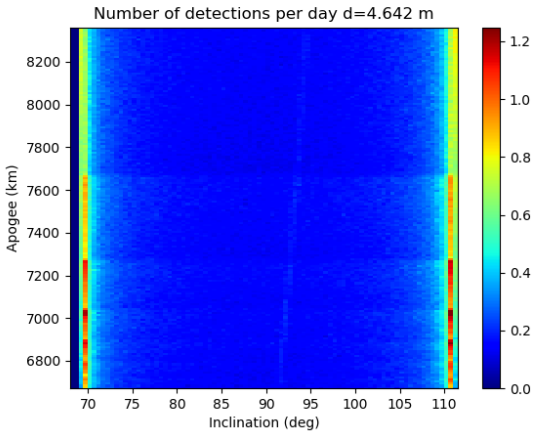

(d) d = 4.60 m

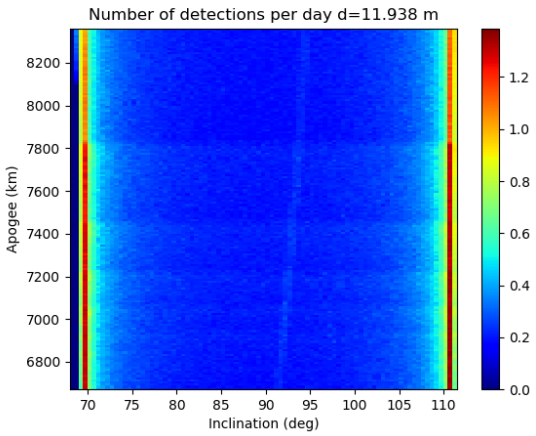

(e) d = 12.0 m

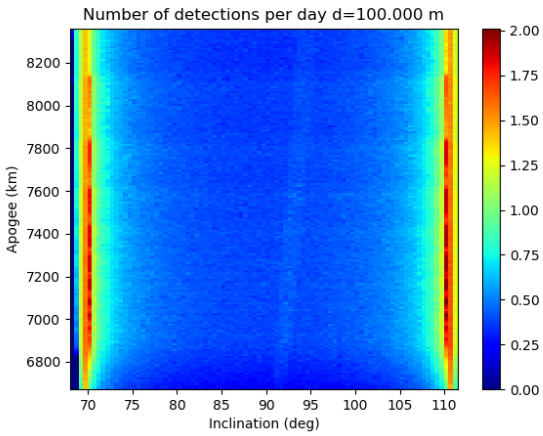

(f) d = 100 m

Figure 8.4: Objects with diameters above 20 cm. The colors indicates the probability of detections per day for a diameters from 20 cm to 100 m. It is seen here for the smallest diameter the probability of detection in range increases proportional as the diameter of the object increases. The increase happens at an inclination of 70° and 110°.

8.3 Comparison

Now, after the simulation of the radar beam is done, the implementation of the sorted MASTER catalog can go into the simulation. With $N(a, i, d)$, it is now possible to filter objects in the MASTER catalog, and to determine how many detections on average for each object. The sorting was done by using the ESA MASTER-2009 model which contains a catalog with six keplerian parameters, as well as information about the diameter of each object. By going through each object in the catalog to sort out the parameters which would be detectable with EISCAT UHF, and obtain a weighted sample of objects, where

$$N_{obs} = N(a, i, d)F \tag{8.1}$$

where N_{obs} is the number of detected objects and is equal to the number of detections per day as a function of apogee, inclination, and diameter, times the abundance factor, F, which is included for each object listed in the MASTER catalog.

This leads to a comparison of the modelling and the beampark. The flowchart in figure (8.5) shows the process of how the comparison of the estimated and the measured data is proceeded.

These two collect their information in two different ways. The beampark collects its data from the space debris environment and collecting their elements and outputs it in the form of range, R, Doppler velocity, v_r, echo strength, S, and the time of the experiment, which by some assumptions, can be transformed into keplerian elements. The simulation, however, collects its data from the space debris model MASTER-2009 which uses the keplerian elements as its parameters. These parameters outputs the same as the BPE would, thus can be compared with the same output from the beampark.

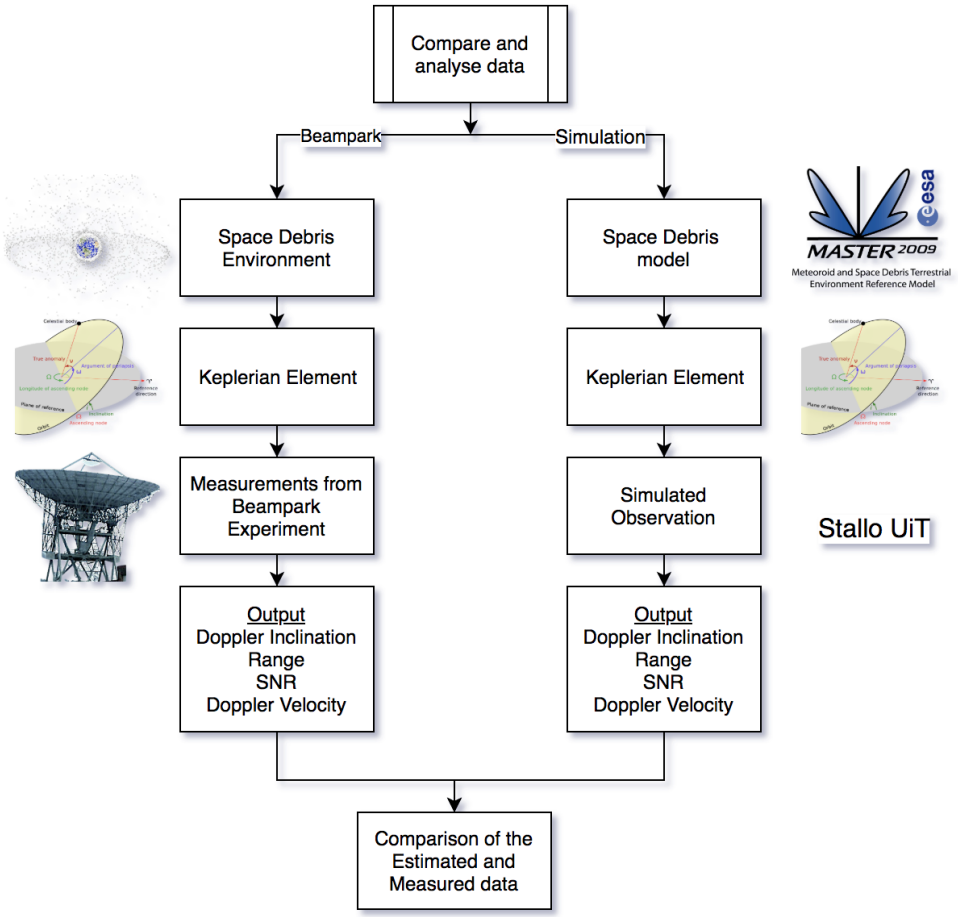

Figure 8.5: Flowchart of the BPE and the simulation.

The spatial density in range (km) is shown in the figure (8.6b). They are both cut to a range of 2000 km even though the observation measured up to 2500 km. The MASTER had some simplified assumption in order to run the simulations. This is why the observation data shows a different peak in the first ranges of 300 km and up to 700 km. Overall the shape of the distribution correlates very well. They both peak at 800 km and at 1500 km. For the Doppler velocity the in figure (8.6b) their peaks are at the same velocities. Both at -0.8 km/s and at +1.3 km/s. However, the general of the shape of the two distributions differs at certain velocities.

This is believed to be due to the simplified assumptions of circular orbits (zero eccentricity), so the true velocity is not correct in the MASTER data, leading to an inversion problem when converting inclination into Doppler velocity.

In figure (8.7) the model and the observation is compared next to each other. It shows the detected objects as a function of range (km) and Doppler Velocity (km/s). The model agrees with the measurement reasonably well. Although, the observation is more smeared than the modelling. Also, the number of detections observed is not as high as in the modelling. It is almost three times more detection in the modeling. Again, this is believed to be due to the true velocity of the objects to orbit in a uniform circular orbit (zero eccentricity). A summary of the comparison of the MASTER and the BPE is given in the table (8.2).

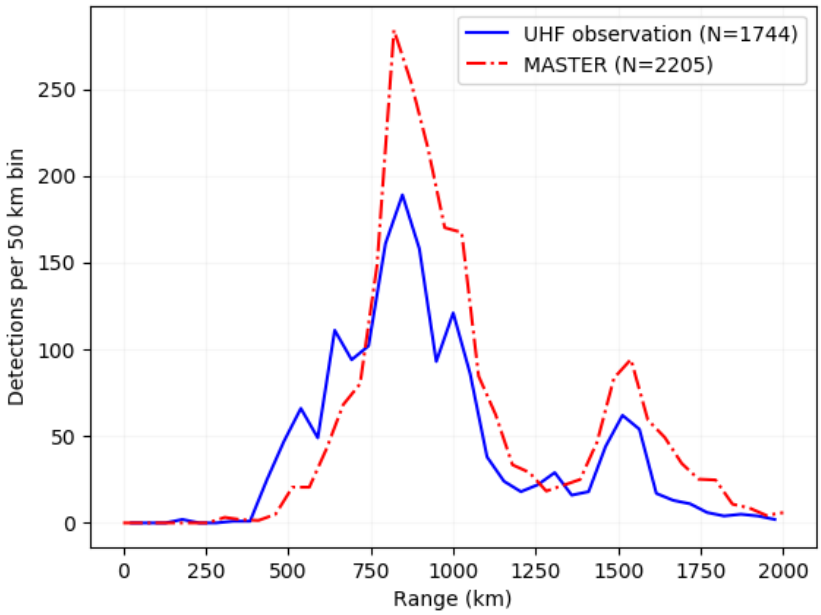

(a)

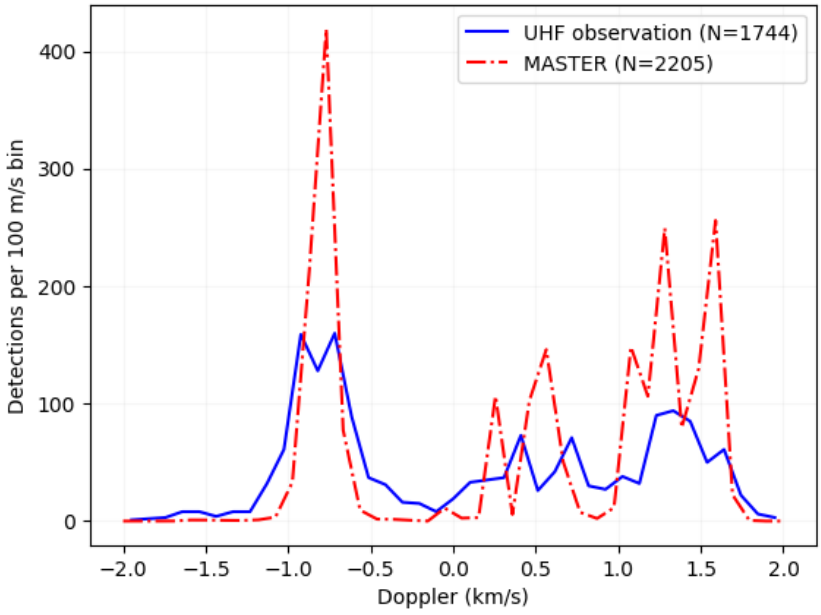

(b)

Figure 8.6: The simulation model with MASTER catalog compared with the measurements from the beampark 2018 campaign. The red stippled line is the simulation with the implemented MASTER catalog, and the blue solid line is the BPE measurement. Figure (a) shows the number of detections per 50 km bin over the range. Figure (b) shows the number of detection per 100 m/s with their corresponding Doppler velocities.

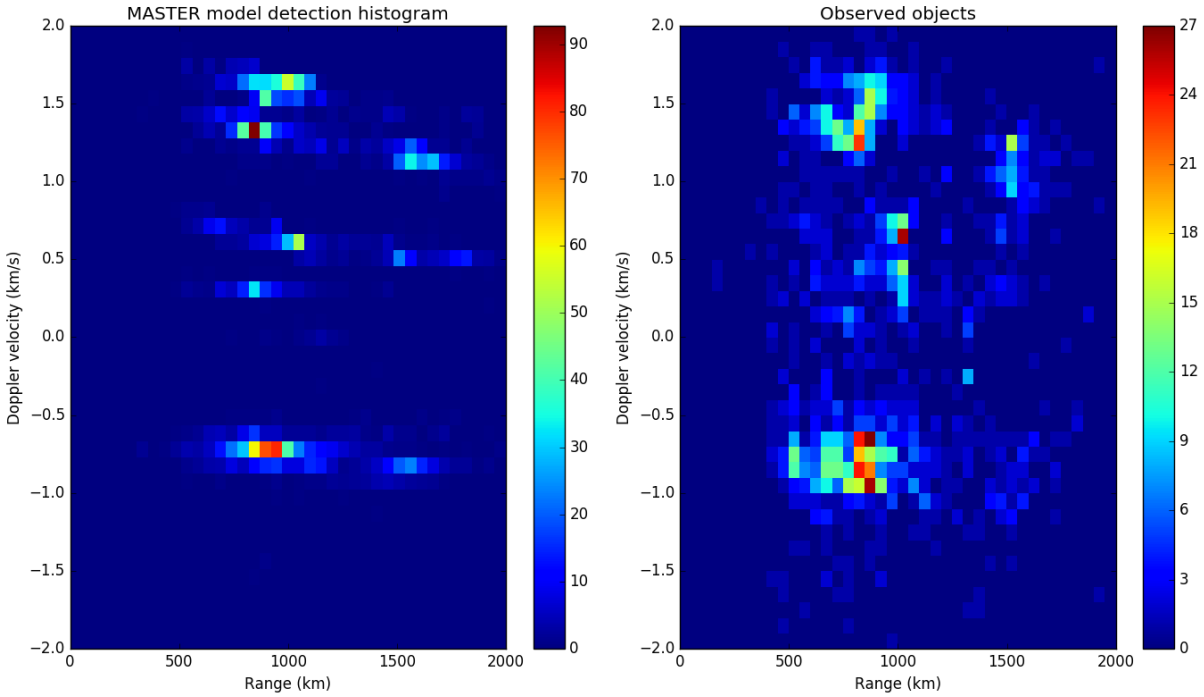

Figure 8.7: 2d histogram of range and Doppler shift..

Table 8.2: The results from the BPE and the simulation model

Specification	Values
Duration (s)	86 400
Duration (hours)	24
Range (km)	300 - 2000
Detection Threshold	> 5
Observed Objects, N_{tot}	1744± 84
MASTER Objects, N_{cat}	2205± 93
Uncorrelated Objects, (N_{tot} - N_{tot})	461
Observed Mean, $-v_r$ (km/s)	-0.8
Observed Mean, $+v_r$ (km/s)	+1.3
MASTER Mean,$-v_r$ (km/s)	-0.8
MASTER Mean, $+v_r$ (km/s)	+1.3

Chapter 9

Size distribution

It is not known what the space debris' true size of is when flying through the beam. As the range increases the fewer small objects gets detected. This happens since SNR is dependent on the $1/R^4$, the signal strength decreases as the range increases, thus not being able to hit the object with sufficient energy at long ranges. It is shown in figure (9.1) the observed distribution of the SNR from the beam park experiment. The number of counts decreases as the SNR increases.

Each object, depending on its size, can be detected in any place within the radar beam, as long as the resulting SNR is larger than the detection threshold. The area of the beam is larger at larger offset angles with respect to the on-axis position, meaning that more detections are made in the sidelobes than the main lobe, if the resulting SNR is sufficient for a detection.

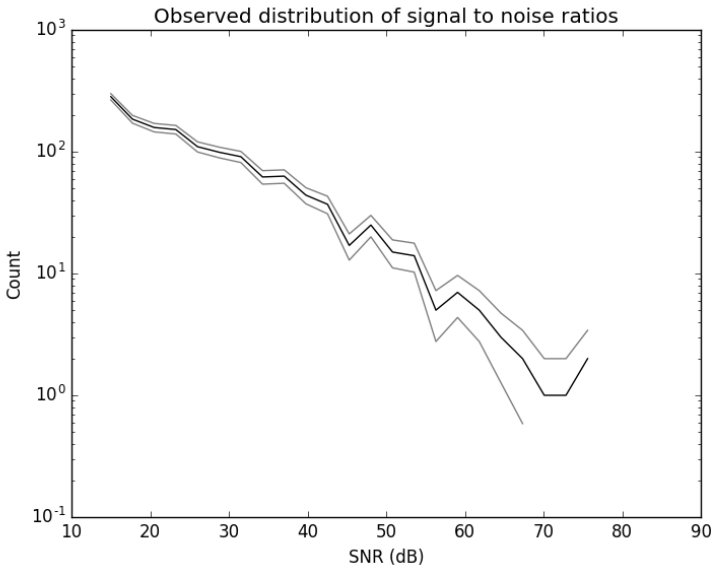

Figure 9.1: The observed distribution of SNR from the beampark experiment.

9.1 Method

In the simulation done in the previous chapter (8) all the number of detections by the simulated observations was stored in a database. The distribution of SNR is a result for a given size of an object d at an apogee of a, this under the assumption of the object moves in circular orbit.

This results in a basis function which provides the histogram of SNR that would result from one object of diameter d_i denoted as,

$$\Psi_i(SNR, a) \tag{9.1}$$

where SNR is the signal to noise ratio and a is the apogee. This can be inserted into the total distribution of observed SNR, which is a linear combination of these basis functions, weighted by the number of objects ϕ_i of each size d_i. The total distribution of observed SNR is given as:

$$D(SNR, a) = \sum_1 \phi_i \Psi_i(SNR, a) \tag{9.2}$$

Ideally, one would want to estimate the size distribution (ϕ_i) for each apogee separately, as each apogee has slightly different basis functions due to the $1/R^4$ dependence of SNR. However for a narrow apogee, there are not sufficiently many objects to obtain a smooth SNR distribution estimate.

In order to include all altitudes in the mode, we need to form a weighted average of basis function across all apogees:

$$\Psi_i^{'}(SNR) = \frac{1}{\sum_a w_a} \sum_a w_a \Psi_i(SNR, a) \tag{9.3}$$

where w_a is the number of objects at apogee bin a. We can now obtain a model that spans across all altitudes:

$$D(SNR) = \sum_i \phi_i \Psi_i^{'}(SNR) \tag{9.4}$$

This is a linear inverse problem, with a positivity contrain on ϕ_i. This can be solved with a non-negative least squares algorithm. However, because of the ill-posed nature of the problem, the smoothness of ψ_i needs to be regularized. This by using the first order Tikhonov regulation to accomplish this:

$$\phi_i - \phi_{i-1} \sim N(0, \alpha d_i^{-1}) \tag{9.5}$$

where α is a smoothness regularization parameter, which depends inversely on object size, allowing large jumps in the distribution for smaller objects (which there are more of). The parameter α determines how strong the overall regularization is. The larger the value, the larger jumps we allow [40, 44].

In addition to this, it is possible to constrain some parts of the distribution a priori. We have chosen to constrain the number of large objects, which are reasonably well known, by the MASTER model abundance. This can be accomplished by making the following assumptions:

$$\phi_i \sin N(\phi_{\text{MASTER},i}, \sigma^2), \tag{9.6}$$

where σ^2 is the variability around the a priori assumed value.

9.2 Instrument Response

The figure (9.2) shows the minimum detectable range of 300 km and up to maximum range of 2000 km. At the lowest altitude, the probability for small objects gets detected more often in the center of the beam. Large objects gets detected at all ranges.

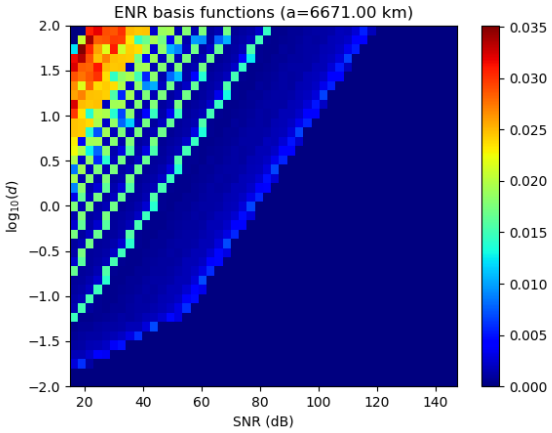

(a) Minimum range 300 km

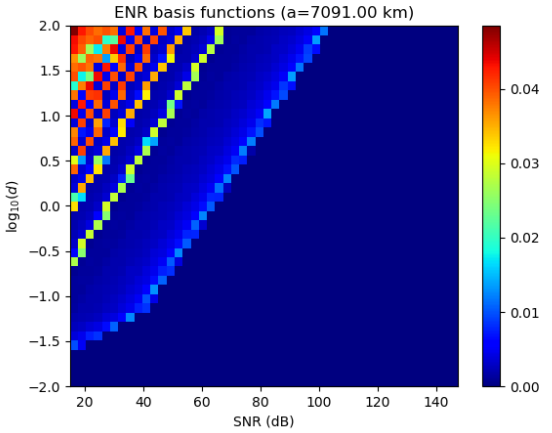

(b) Range 720 km

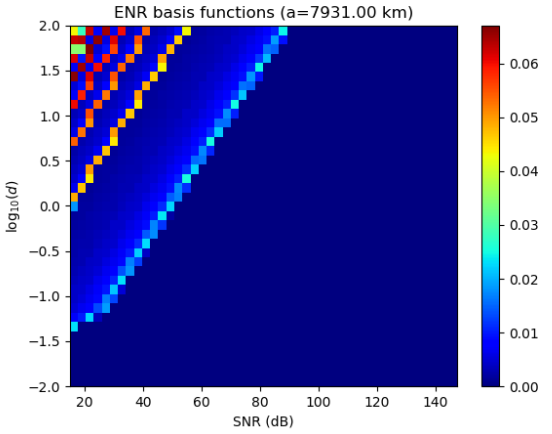

(c) Range 1590 km

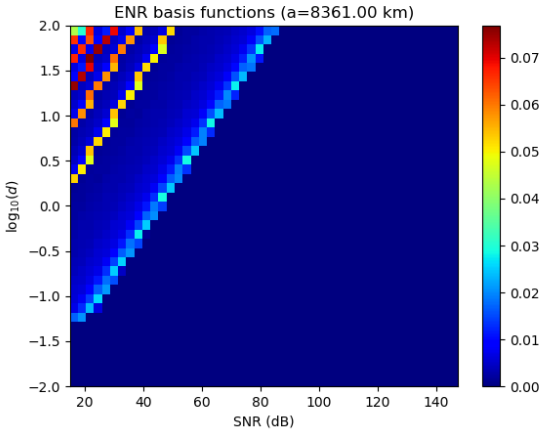

(d) Maximum range 2000 km

Figure 9.2: The figures shows the beam pattern and its strength in gain. The colors indicates the probability of detections of a space debris flying through the different lobes of the beam. As the range increases, the fewer small objects gets detected. Smaller objects are detected only within the main lobe of the antenna beam pattern, while larger objects are detected most of the time within antenna sidelobes. ENR is the energy-to-noise ratio which is the same as the signal-to-noise SNR in this case.

9.2.1 Size Inversion

By looking at the spectrum at the receiver, it is possible to retrieve some information about the shape of the target. Depending on the radar cross sections geometry an assumption about its size may be obtained. In both the BPE measurements and the modelling it was assumed that the target was a perfect conducting sphere, so this assumption still holds.

The results of the size inversion are shown in figure (9.3a), where the estimated size distribution is in figure (9.3b).

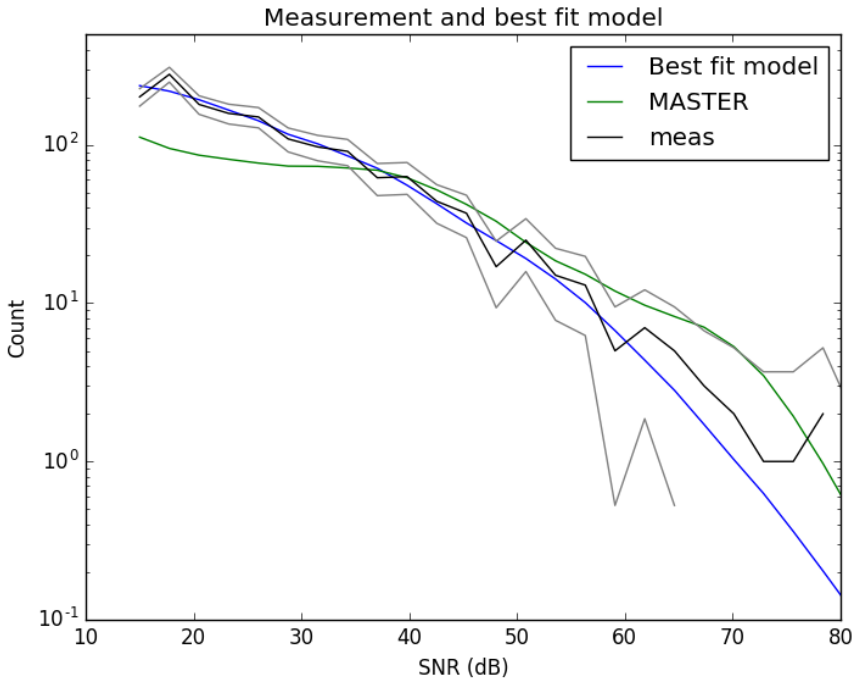

(a)

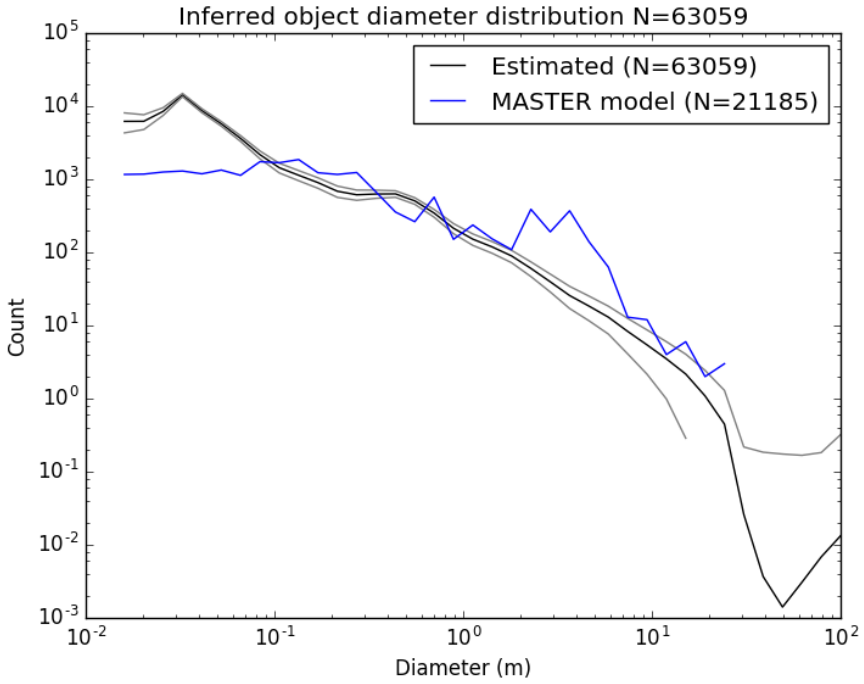

(b)

Figure 9.3: Figure (a) shows the measurement, and best fitting model. Also, the model of SNR distribution corresponding the the MASTER model size distribution is shown. No prior information on the size distribution is applied. Figure (b) shows the inferred size distribution of objects. Also shown is the size distribution obtained from the MASTER model. No prior assumptions on the size distribution, apart from smoothness is applied.

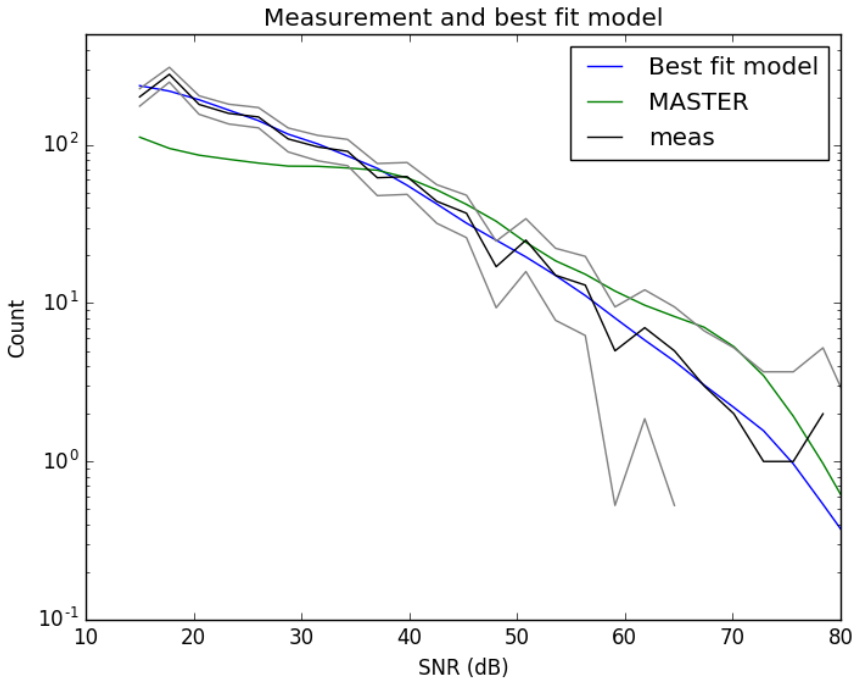

(a)

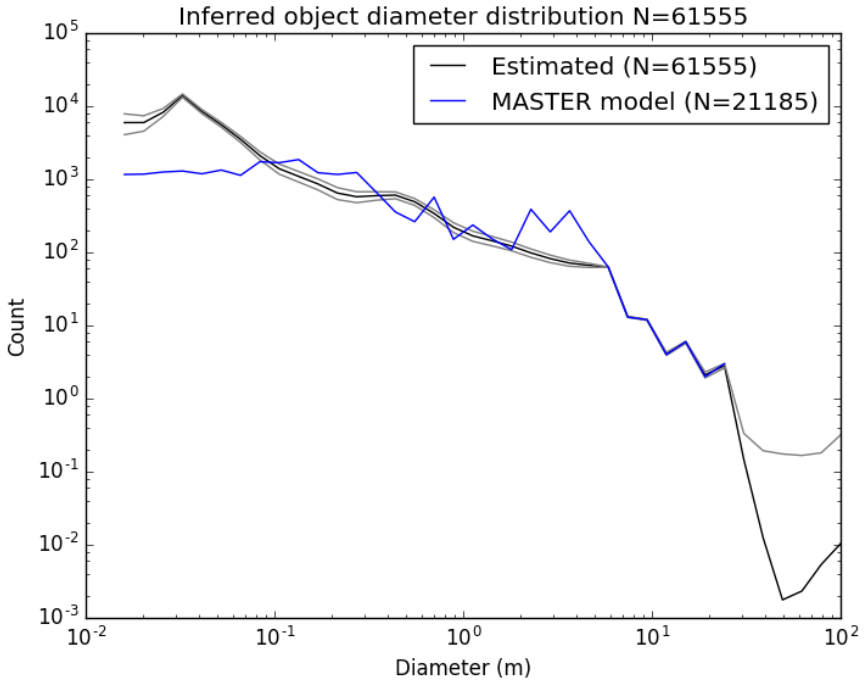

(b)

Figure 9.4: Figure (a) shows the measurement, and best fitting model. Also, the model of SNR distribution corresponding the the MASTER model size distribution is shown. Figure (b) shows the inferred size distribution of objects. Also shown is the size distribution obtained from the MASTER model. For both of the figures the distribution of objects larger than 5 meters in size are assumed to be the same as the MASTER model.

The results of the size inversion, which constrains the distribution of objects larger than 5 m to the MASTER model are are shown in Figure 9.4a. The estimated size distribution containing the prior assumption is shown in Figure 9.4b.

The results are quite similar. However, when implementing the distribution of objects larger than 5 meters in size, it shows that the inversion result suggest a larger number of objects smaller than 10 cm. it is not immediately obvious why this is so. One possibility is that larger objects saturate the EISCAT receiver, which results in no SNR observation higher than about 80 dB. When this is the case, the heavy on low SNR basis functions corresponding to larger objects cannot contribute to the SNR distribution, which in other words state that large objects result in many low SNR detections when passing though the sidelobes, and the small objects with low SNR need to explain the low SNR portion of the SNR distribution. Another, possibility is that there are more small sized objects than the MASTER model predicts. In order to validate this, more observations with different radars are needed. It would also be advantageous to attempt to measure the linearity of the radar system, and if possible, increase the linearity so that high signal to noise objects can be faithfully observed.

Chapter 10

Conclusions

After years of launching into space it has in the later years occurred more and more unintentional collisions. It is seen that especially in the polar regions it has started to become more dense with space debris, and as most of the ground observation instruments based further south these polar regions are not easily monitored. As well, most of them cannot detect objects below 10 cm. EISCAT, however, is located in the polar region and can measure down to 1 cm between ranges of 400 to 1500 km, compared to the space surveillance network which only tracks objects above 10 cm. This is due to its small beam with high spatial resolution. EISCAT facilities have done several beampark measurements over the years tracking some of the worst satellite collisions with a low cost budget by paralleling the measurements with ionospheric measurements with just a separate space debris receiver.

From the beampark experiment (BPE) that was done at 4th of January 2018, the plots shows high amount of density at the range of 800-900 km, and another peak at 1 450 km. The Doppler velocity had a mean velocity of $-1\ km/s$ and $+0.84\ km/s$ indicating the detected objects had an Doppler inclination of 98° and 78°, which seemed to occur periodically at each 3rd hour (12 000 s). The signal-to-noise ratio showed a density of 18 dB at the range of 800 km. Also what seems to be a recent break-up event is shown at around 38 000 seconds and 82 000 seconds at a range of 1 350 km, which is not known to be to this date, but by knowing its keplerian elements it can be traced back to its origin.

A modeling of the EISCAT observations of space debris in the form of simulating a beampark experiment was obtained in order to compare the detected with the estimated. From the results of the beampark simulation, it was found through the European Space Agency Meteoroid and Space Debris Terrestrial Environment Reference (ESA MASTER) catalog that there is the same peak at both ranges at 800 km and 1500 km as in the BPE. However, the MASTER indicates that it should be 2205 detections, while UHF during the BPE only detected 1744 objects. For the Doppler velocity, the peak at $-0.8km/s$ was almost 3 times more than the BPE, and these two deviated a lot on the positive side. Here, however, MASTER had two large peaks at $1.3km/s$ and $1.5km/s$, which is to believed to the negligible keplerian elements such as the zero eccentricity, and zero right ascension of the ascending node, RAAN.

For the 2-dimensional density plots of the range (km) and its corresponding Doppler velocity the MASTER and the BPE correlates very well in shape, but still here MASTER indicates that there should be almost three times more detections. The smallest measured during the BPE diameter was 1.32 cm, the largest detected object was to believed to be 3.08 m. The MASTER catalog was sorted to detect objects between 1 cm and 100 m, but the simulation shows that with EISCAT radar performance, below 1.32 m, it is almost not detected, and it had to be above this to be detected in

the range. This is believed that below this size it will not reflect enough energy back to the radar and exceed its threshold, thus not detected. As the size of the object increases, the further out in range it is observable, this is because small objects are only detected where the intensity of the beam is strong, while larger ones are detected most of the time in the sidelobes.

Bibliography

[1] Adrian V Gheorghe and Daniel E Yuchnovicz. The space infrastructure vulnerability cadastre: Orbital debris critical loads. *International Journal of Disaster Risk Science*, 6(4):359–371, 2015.

[2] Heiner Klinkrad. *Space debris*. Wiley Online Library, 2010.

[3] Juha Vierinen, J Markkanen, H Krag, J Siminski, and A Mancas. Use of eiscat 3d for observations of space debris.

[4] Satellite Tool Kit. Analytical graphics, inc, 2005.

[5] Space Track. the source for space surveillance data. *Available: www. space-track. org*, 2012.

[6] Wiley J Larson, James R Wertz, et al. Space mission analysis and design. *Space technology library*, 8, 1999.

[7] Arthur C Clarke and Extra-Terrestrial Relays. Wireless world, 1945.

[8] National Aeronautics and Space Administration. *Orbital Debris Quarterly News*, volume Volume 17, Issue 4. NASA Orbital Debris Program Office, https://orbitaldebris.jsc.nasa.gov/quarterly-news/pdfs/odqnv17i4.pdf, October 2013.

[9] JC Liou, AK Anilkumar, B Bastida, T Hanada, H Krag, H Lewis, MXJ Raj, MM Rao, A Rossi, and RK Sharma. Stability of the future leo environment–an iadc comparison study. In *Sixth European conference on space debris, ESOC, Darmstadt, Germany*, volume 38, 2013.

[10] Donald J Kessler and Burton G Cour-Palais. Collision frequency of artificial satellites: The creation of a debris belt. *Journal of Geophysical Research: Space Physics*, 83(A6):2637–2646, 1978.

[11] National Aeronautics and Space Administration. *Orbital Debris Quarterly News*, volume Volume 20, Issue 1 and 2. NASA Orbital Debris Program Office, https://orbitaldebris.jsc.nasa.gov/quarterly-news/pdfs/odqnv20i1-2.pdf, April 2016.

[12] V Braun, S Lemmens, B Reihs, H Krag, and A Horstmann. Analysis of breakup events. In *Proceedings of the Seventh European Conference on Space Debris, Darmstadt, Germany*, 2017.

[13] NASA. Orbital debris management and risk mitigation. 2012.

[14] ESA. Space debris story (2013), Jan 2016.

[15] Andrew Cutting. Ashes in orbit: celestis spaceflights and the invention of post-cremationist afterlives. *Science as Culture*, 18(3):355–369, 2009.

[16] MA Martín Serrano, M Catania, J Sánchez, A Vasconcelos, Dirk Kuijper, and X Marc. Sentinel-1a flight dynamics leop operational experience. In *International Symposium on Space Flight Dynamics Symposium*, 2015.

[17] E Malnes, M Eckerstorfer, and H Vickers. First sentinel-1 detections of avalanche debris. *The Cryosphere Discussions*, 9(2):1943–1963, 2015.

[18] H Krag, M Serrano, V Braun, P Kuchynka, M Catania, J Siminski, M Schimmerohn, X Marc, D Kuijper, I Shurmer, et al. A 1 cm space debris impact onto the sentinel-1a solar array. *Acta Astronautica*, 137:434–443, 2017.

[19] Adrian Schubert, David Small, Nuno Miranda, Dirk Geudtner, and Erich Meier. Sentinel-1a product geolocation accuracy: commissioning phase results. *Remote sensing*, 7(7):9431–9449, 2015.

[20] Eric L Christiansen, James L Hyde, and Greg Snell. Spacecraft survivability in the meteoroid and debris environment. *AIAA paper*, (92-1409):24–27, 1992.

[21] WU Ziniu, HU Ruifeng, QU Xi, WANG Xiang, and WU Zhe. Space debris reentry analysis methods and tools. *Chinese Journal of Aeronautics*, 24(4):387–395, 2011.

[22] WH Ailor and RP Patera. Spacecraft re-entry strategies: meeting debris mitigation and ground safety requirements. *Proceedings of the Institution of Mechanical Engineers, Part G: Journal of Aerospace Engineering*, 221(6):947–953, 2007.

[23] Maj Edward P Chatters IV and Maj Brian J Crothers. Chapter 19: Space surveillance network. *PDF). AU-18 Space Primer*, page 252, 2009.

[24] J Markkanen, M Lehtinen, A Huuskonen, and A Väänänen. Measurements of small-size debris with backscatter of radio waves. *Final report*, 2002.

[25] Zoran Sodnik, Josep Perdigues Armengol, Reinhard H Czichy, and Rolf Meyer. Adaptive optics and esa's optical ground station. In *Proc. SPIE*, volume 7464, page 746406, 2009.

[26] John N Opiela and Paula H Krisko. Evaluation of orbital debris mitigation practices using evolve 4. 1. *Science and Technology Series*, 2002.

[27] S Flegel, J Gelhaus, C Wiedemann, P Vorsmann, M Oswald, S Stabroth, H Klinkrad, and H Krag. The master-2009 space debris environment model. In *Fifth European Conference on Space Debris*, volume 672, 2009.

[28] PH Krisko, S Flegel, MJ Matney, DR Jarkey, and V Braun. Ordem 3.0 and master-2009 modeled debris population comparison. *Acta Astronautica*, 113:204–211, 2015.

[29] Nicholas L Johnson and Eugene G Stansbery. The new nasa orbital debris mitigation procedural requirements and standards. *Acta Astronautica*, 66(3):362–367, 2010.

[30] Norwegian Ministry of Trade and Industry. *Between heaven and earth: Norwegian space policy for business and public benefit.* The Norwegian Government.

[31] Departementenes sikkerhets-og serviceorganisasjon Informasjonsforvaltning. *Digital sårbarhet–sikkert samfunn Beskytte enkeltmennesker og samfunn i en digitalisert verden.* ISBN 978-82-583-1249-6. 07 Aurskog AS, https://lovdata.no/static/NOU/nou-2015-13.pdf, 2015.

[32] TG Reid, Andrew M Neish, Todd F Walter, and Per K Enge. Leveraging commercial broadband leo constellations for navigation. In *29th international technical meeting of the satellite division of the Institute of Navigation (ION GNSS+ 2016), Portland*, 2016.

[33] PV Radhadevi, SS Solanki, V Nagasubramanian, Archana Mahapatra, D Sudheer Reddy, MV Jyothi, Krishna Sumanth, J Saibaba, and Geeta Varadan. New era of cartosat satellites for large scale mapping. *Photogrammetric Engineering & Remote Sensing*, 76(9):1031–1040, 2010.

[34] Takushi Tanaka, Yoshiyuki Kawamura, and Takakazu Tanaka. Overview and operations of cubesat fitsat-1 (niwaka). In *Recent Advances in Space Technologies (RAST), 2013 6th International Conference on*, pages 887–892. IEEE, 2013.

[35] Kjetil Wormnes, Ronan Le Letty, Leopold Summerer, Rogier Schonenborg, Olivier Dubois-Matra, Eleonora Luraschi, Alexander Cropp, Holger Krag, and Jessica Delaval. Esa technologies for space debris remediation. In *Proceedings of the 6th IAASS Conference: Safety is Not an Option*, pages 3–4, 2013.

[36] K. Blix. Alomar observatory, andøya space center – what's up? In *44th Annual European Meeting on Atmospheric Studies by Optical Methods, 4-8 September 2017, Barcelona, Spain*, 2017.

[37] MI Skolnik. Radar handbook, vol. 1, 8, 2008.

[38] JK Hargreaves. Auroral absorption of hf radio waves in the ionosphere: A review of results from the first decade of riometry. *Proceedings of the IEEE*, 57(8):1348–1373, 1969.

[39] Asta Pellinen-Wannberg. The radio physics of meteors: High resolution radar methods offering new insights. *URSI Radio Science Bulletin*, 84(4):32–45, 2011.

[40] Juha Vierinen et al. On statistical theory of radar measurements. 2012.

[41] Juha Vierinen, Jussi Markkanen, and Holger Krag. High power large aperture radar observations of the iridium-cosmos collision. In *Proc. 5th ESA space debris conference*, 2009.

[42] Holger Krag, Heiner Klinkrad, Rüdiger Jehn, Jussi Markkanen, and Ludger Leushacke. Detection of small-size space debris with the fgan and eiscat radars. In *Proc. 7th US-Russian Space Surveillance Workshop*, 2007.

[43] J Vierinen, JL Chau, N Pfeffer, M Clahsen, and G Stober. Coded continuous wave meteor radar. *Atmospheric Measurement Techniques Discussions*, 8(7):7879–7907, 2015.

[44] Richard C Aster, Brian Borchers, and Clifford H Thurber. *Parameter estimation and inverse problems*, volume 90. Academic Press, 2011.